A Micro-Positioning Motion System to Enhance Lithography in Semiconductor Manufacturing Machines

by

Mahmoud Al-Tamimi

A thesis submitted to the Department of Mechanical Engineering

in partial fulfilment of the requirements for the degree of

Master of *Engineering*

at the

Memorial University of Newfoundland

October 2020

Suppervisors: Dr. Mohammad Al Janaideh and Dr. Ting Zou

St. John's Newfoundland

Abstract

This study proposes a novel precision micro-motion system to enhance the lithography process in the semiconductor manufacturing machines. This proposed micro-motion system is a new smart-materials stage that integrates piezoelectric actuators in the reticle stage of the future semiconductor manufacturing machines. The proposed smart-materials based reticle (SMBR) implements piezoelectric actuators to a novel flexure hinge-based mechanism to enhance the precision of the reticle stage; such that it reduces the relative in-plane micro-positioning errors in the synchronization motion between the reticle stage and the wafer stage in a time period less than the current settling time in lithography machines, 10 ms. The proposed SMBR can provide in-plane translational motions along x- and y-axes, and in-plane θ_z-rotational motion around z-axis with an amount of 11.7462 μm $\times$ 11.7462 μm $\times$ 0.4713 mrad, respectively, to correct the orientation of the reticle stage which governs the pattern of the integrated circuit being printed. The proposed SMBR considers the current dynamic performance of reticle stage of the semiconductor manufacturing machines; such that (i) it corrects the in-plane synchronization errors in a time period less than the settling time of the short-stroke, and (ii) the working frequency bandwidth remains above 550 Hz. The proposed SMBR can be integrated with the precision

motion systems of the semiconductor manufacturing machines to enhance the storage capacity, the functionality of the devices, and the CPU processing capability.

Acknowledgements

I would like to acknowledge some people without whom this work would have never come to life. My truthful gratitude begins with my supervisors, Prof. Mohammad Al Janaideh and Prof. Ting Zou, who have guided me, supported me, and enhanced my knowledge and skills through my academic journey. This is the best time to acknowledge that the best decision I have ever made in my academic journey was joining your research group. You were always there by my side, willing to help, support, and remove all the barriers that could prevent getting this work done. No words of appreciation and gratitude are enough in front of you. You are my role model in both my academic and personal life.

I would like to thank Dr. Yazan Al-Rawashdeh, who has always opened all the possible opportunities for me -even those which I used to think were impossible- to flourish my academic research. I simply cannot thank you enough. I would like to express my gratitude to Prof. Geoff Rideout and Prof. Jianming (James) Yang, who provided me with the best knowledge, tools, and skills that brought to me new ideas that can be implemented to improve my research work. I have always been honored to be a student in your classes.

I would like to express my appreciation to the Memorial University of Newfoundland that has facilitated all the required resources to conduct our research in the highest possible criteria.

My most profound appreciation for those whom I always remember (my parents) for their endless support. Thank you for teaching me the value of education and encouraging me in every step. Thank you for your blessings and unconditional love for me, you mean the world to me.

I would like to thank my wife and my daughter; you are the true reason behind every single success in my research journey. You are my rock during hard times. For all that they have done, I dedicate this work to them.

— Mahmoud Al-Tamimi   October 2020

Contents

Abstract **ii**

Acknowledgements **iv**

List of Symbols and Abbreviations **ix**

List of Tables **x**

List of Figures **xii**

1 Introduction **1**

1.1 Semiconductor Manufacturing 1

1.1.1 Precision Requirements in Semiconductor Manufacturing Machines 4

1.1.2 Attaining the Precision Requirements in Lithography Machines 5

1.1.3 Sources of Positioning Uncertainties in Lithography Machines 6

1.1.3.1 Air-bearings 6

1.1.3.2 Voice Coil Actuators with the Presence of Magnetic Suspension System 6

1.1.3.3 Other Sources of Positioning Uncertainties 7
1.1.4 Error Classification and Prevention Techniques in Lithography Machines 8
1.1.5 The Contributions to Enhance the Performance of Lithography Process 9
1.2 Compliant Mechanism Designs 11
1.2.1 x-y-Compliant Micro-/Nano- Positioning Stages 13
1.2.2 x-y-θ_z-Compliant Micro-/Nano- Positioning Stages 15
1.3 Piezoelectric Actuators 16
1.4 Contributions of the Thesis 17
1.5 Outline of the Thesis 18
2 Mechanism Design, Modeling, and Optimisation 20
2.1 Introduction 20
2.2 Mechanism Design for the Proposed Smart Materials-Based Reticle . 22
2.2.1 Stage's Working Principle 25
2.3 Compliance Analysis 27
2.3.1 Compliance Modelling for Limb 1 28
2.3.2 Compliance Modelling for Limb 2 30
2.3.3 Compliance Modelling for the Reticle 32
2.3.4 Compliance Modelling of the Entire Smart Materials-Based Reticle 33
2.4 Static and Stress Analysis 33
2.5 Modal Analysis 43

2.6 Dimensional Optimisation of the Proposed Smart Materials-Based Reticle . . . 52
2.7 Expressing the Output Displacements in Terms of Input Voltage . . . 57
2.8 Conclusions of the Chapter . . . 59

3 Dynamic Analysis of the Proposed Smart Materials-Based Reticle Integrated Into the Short-Stroke 62

3.1 Introduction . . . 63
3.2 Development of Dynamic Model of the Proposed SMBR Within the Short-Stroke . . . 65
3.3 Numerical Results . . . 76
3.3.1 Harmonic Analysis . . . 76
3.3.2 Transient Analysis . . . 80
3.3.2.1 Case 1: Activating the Proposed Smart Materials-Based Reticle Only . . . 82
3.3.2.2 Case 2: Activating the Short-Stroke Only . . . 83
3.3.2.3 Case 3: Activating both the Proposed Smart Materials-Based Reticle and the Short-Stroke at Full Stroke . . 83
3.4 Conclusions of the Chapter . . . 84

4 Conclusions and Future Work 86

Bibliography 89

List of Symbols and Abbreviations

PZT	Piezoelectric Actuator.	
SMBR	Smart Materials-based Reticle.	
CoG	Center of Gravity.	
DoF	Degree of Freedom.	
GWO	Grey Wolf Optimizer.	
WEDM	Wire Electrical Discharge Machining.	
FEA	Finite Element Analysis.	
FEM	Finite Element Method.	
PRBM	Pseudo-Rigid-Body Model.	
IC	Integrated Circuit.	
CD	Critical Dimension.	
MA	Moving Average.	
MSD	Moving Standard Deviation.	
IFT	Iterative Feedback Tuning.	
MIMO	Multi-Input Multi-Output.	
SISO	Single-Input Single-Output.	

O_B	The center of mass of the reticle.	$[-]$
a	The horizontal distance between the line of actuation of a piezoelectric actuator and the center of mass of the reticle.	$[m]$
$\mathbf{C}$	A 6×6 compliance matrix.	$[m/N]$
$\mathbf{T}_i^j$	The transformation matrix from frame O_i to frame O_j.	$[-]$
E_r, E_s, E	The Young's modulus of the reticle, the flexure mechanism, and for a beam, respectively.	$[Pa]$
ν_r, ν_S, ν	The Poisson's ratio of the reticle, the flexure mechanism, and for a beam, respectively.	$[-]$

ρ_r, ρ_s, ρ	The density of the reticle, the flexure mechanism, and for a beam, respectively.	$[kg/m^3]$
K_x, K_y	The equivalent stiffness of the proposed SMBR along the x- and y-axes, respectively.	$[N/m]$
K_{θ_z}	The equivalent stiffness of the proposed SMBR around the z-axis.	$[N.m/rad]$
x_{out}, y_{out}	The in-plane output translational motions of the proposed SMBR along x- and y-axes, respectively.	$[m]$
$\theta_{z\text{out}}$	The in-plane output θ_z-rotational motion of the proposed SMBR around z-axis.	$[rad]$
x_{ss}, y_{ss}, θ_{ss}	The output displacements of the short-stroke during the translational motions along x- and y-axes, and during the θ_z-rotational motion around z-axis, respectively.	$[m]$, $[m]$, $[rad]$
f_x, f_y	The resultant input forces provided by the piezoelectric actuators along x- and y-axes, respectively.	$[N]$
M_{θ_z}	The total input moment arises by the piezoelectric actuators around z-axis.	$[N.m]$
$q_{p_{i,n}}$, $q_{p_{i,a}}$	The nominal and actual displacements, respectively, of the ith piezoelectric actuator.	$[m]$
F_{p_i}	The input force provided by the ith piezoelectric actuator.	$[N]$
k_{p_i}	The stiffness of the ith piezoelectric actuator.	$[N/m]$
n_a	The assigned factor of safety.	$[-]$
$\mathbf{M}$	The equivalent mass matrix for the proposed SMBR.	$[kg]$, $[kg.m^2]$
$\mathbf{K}$	The equivalent stiffness matrix for the proposed SMBR.	$[N/m]$
$\mathbf{\Phi}_j$, ω_j^2	The eigenvectors and eigenvalues, respectively, of the proposed SMBR.	$[-]$
ω_n	The undamped natural frequency.	$[rad/s]$
ω_d	The damped natural frequency.	$[rad/s]$
ω	The driving (or forcing) frequency.	$[rad/s]$
t_s	The settling time.	$[s]$
m_x, m_y	The total masses of the SMBR that contribute in the translational motions along x- and y-axes, respectively.	$[kg]$
J_{θ_z}	The inertia of the SMBR around z-axis that contribute in the θ_z-rotational motion around z-axis.	$[kg.m^2]$

List of Tables

2.1 Various operating case scenarios of the proposed SMBR. 38
2.2 In-plane resonant frequencies of the stage (Hz). 48
2.3 Modal effective mass and inertia of the proposed SMBR 50
2.4 Mass participation percentage of the proposed SMBR 50
2.5 The architecture parameters of the proposed SMBR (mm) 57
2.6 Material properties of the proposed SMBR 58

3.1 The parameters used in the harmonic and transient analyses. 76

List of Figures

1.1 A schematic representation of the lithography machine architecture, which consists of three main parts: (i) the reticle stage, (ii) the projection lenses, and (iii) the wafer stage. The y-direction represents the scanning direction, and the reticle stage is our working scope. 2

1.2 Basic principle of lithography process: (a) basic layout of the machine, and (b) part of the step-and-scan exposure profile across the dies on a silicon wafer. 3

1.3 Illustration of positioning error classifications in lithography process: (a) translational (or overlay) error; the reticle field is shifted along x- and y-axes, (b) rotational error; the reticle field is rotated around z-axis, (c) magnification error; the reticle field is shifted along z-axis, and (d) trapezoid (or tilting) error; the reticle field is rotated around x- and/or y-axes. 8

2.1 The proposed SMBR 23

2.2 The proposed SMBR's operation principle in the xy-plane: (a) the in-plane output translational motion along x-axis, (b) the in-plane output translational motion along y-axis, and (c) the in-plane output θ_z-rotational motion around z-axis. *The red bars represent the active piezoelectric actuators, whereas the yellow bars represent the inactive actuators.* . . . 26
2.3 The flexure hinges used in the proposed stage: (a) right-circular flexure hinge, and (b) rectangular flexure hinge (leaf spring). . . . 27
2.4 The design parameters and dimensions for limb 1: (a) the entire limb, and (b) the upper part of the limb. . . . 29
2.5 The design parameters and dimensions for limb 2: (a) the entire limb, and (b) the top-left part of the limb. . . . 30
2.6 The proposed SMBR . . . 35
2.7 The primary in-plane displacements of the proposed SMBR under various values of loads: (a) the translational displacement along x-axis, (b) the translational displacement along y-axis, and (c) the θ_z-rotation about z-axis. . . . 36
2.8 The parasitic in-plane coupling displacements of the proposed SMBR during the primary motions: (a) along x-axis and (b) along y-axis . . 37
2.9 The primary in-plane displacements of the proposed SMBR under various values of loads taking into consideration the compensation factors: (a) the translational displacement along x-axis, (b) the translational displacement along y-axis, and (c) the θ_z-rotation about z-axis. . . . 38
2.10 The parasitic in-plane coupling displacements of the proposed SMBR, taking into consideration the compensation factors, during the primary motions: (a) along x-axis and (b) along y-axis . . . 39

2.11 The maximum equivalent von-Mises stress at the critical locations at different load values for the translational motions along x- and y-axes, and the θ_z-rotational motion around z-axis. 42

2.12 The critical locations at which the maximum stress occur during (a) translational motion along x-axis, (b) translational motion along y-axis, and (c) θ_z-rotational motion around z-axis. 42

2.13 The minimum value of the factor of safety in the proposed SMBR during the (a) translational motion along x-axis, (b) translational motion along y-axis, and (c) θ_z-rotational motion around z-axis. 43

2.14 The first six mode shapes of the proposed SMBR extracted by *ANSYS*: (a) Mode 1 at 859.14 Hz, (b) Mode 2 at 860.14 Hz, (c) Mode 3 at 1112.9 Hz, (d) Mode 4 at 1328.6 Hz, (e) Mode 5 at 1346.9 Hz, and (f) Mode 6 at 1370.4 Hz. 48

2.15 Parametric study for the effecting parameters: (a) the influence of t_4 and l_{11} on K_x and K_y, (b) the influence of t_4 and l_{11} on K_{θ_z}, (c) the influence of l_{17} and l_{20} on K_x and K_y, (d) the influence of l_{17} and l_{20} on K_{θ_z}, (e) the influence of r_1 and $t_{0,1}$ on K_x and K_y, (f) the influence of r_1 and $t_{0,1}$ on K_{θ_z}, (g) the influence of S_1 and S_4 on K_x and K_y, (h) the influence of S_1 and S_4 on K_{θ_z}, (i) the influence of S_2 and S_5 on K_x and K_y, (j) the influence of S_2 and S_5 on K_{θ_z}, (k) the influence of S_3 and S_5 on K_x and K_y, (l) the influence of S_3 and S_5 on K_{θ_z}, (m) the influence of l_6 and S_5 on K_x and K_y, and (n) the influence of l_6 and S_5 on K_{θ_z}. 54

2.16 The convergent process of the GWO: (a) K_x convergence, (b) K_y convergence, (c) K_{θ_z} convergence, and (d) optimising parameters convergence. 56

2.17 Maximum stiffness histories over all repetitions: (a) the K_x and K_y histories, and (b) K_{θ_z} history. 57
2.18 The required input voltage to be supplied to the piezoelectric actuators in order the proposed SMBR achieves a desired in-plane output displacement function: (a) $x_{\text{out}} = 5\sin(50t)$ μm, (b) $y_{\text{out}} = 3\cos(50\text{t})$ μm, and (c) $\theta_{\text{zout}} = 0.2\sin(50\text{t})$ mrad. 59

3.1 A schematic representation of the lithography machine architecture, which consists of three main parts: (i) the reticle stage, (ii) the projection lenses, and (iii) the wafer stage. The y-direction represents the scanning direction, and the reticle stage is our working scope. 64
3.2 A schematic representation of the proposed SMBR stage within the short-stroke of the scanning motion system in lithography machine. . 64
3.3 An equivalent lumped mass-spring model of the proposed SMBR within the short-stroke. 66
3.4 Bode plot of the derived model for the output motion along x-axis: (a) the frequency response, and (b) the phase angle of the response. . . . 78
3.5 Bode plot of the derived model for the output motion around z-axis: (a) the frequency response, and (b) the phase angle of the response. . 79
3.6 Bode plot of the derived model for the output motions: (a) along x-axis and (b) around z-axis, while the piezoelectric actuators are deactivated 80
3.7 The simulation scheme for the translational motions along x- and y-axes, and the θ_z-rotational motion about z-axis, where the transfer functions are obtained using the Equations (3.12) and (3.24). 81

3.8 A comparison between the FEA results and the analytical results for the output in-plane displacement responses measured at the center of gravity (CoG) of the proposed SMBR, O_B, when the proposed SMBR is activated at full stroke while the short-stroke is kept inactive: (a) the translational motion along x-axis, (b) the translational motion along y-axis, and (c) the θ_z-rotational motion about z-axis. 82
3.9 A comparison between the FEA results and the analytical results for the output in-plane displacement responses measured at the center of gravity (CoG) of the proposed SMBR, O_B, when the short-stroke is activated at full stroke while the proposed SMBR is kept inactive: (a) the translational motion along x-axis, (b) the translational motion along y-axis, and (c) the θ_z-rotational motion about z-axis. 83
3.10 A comparison between the FEA results and the analytical results for the output in-plane displacement responses measured at the center of gravity (CoG) of the proposed SMBR, O_B, when both the proposed SMBR and the short-stroke are activated at full stroke: (a) the translational motion along x-axis, (b) the translational motion along y-axis, and (c) the θ_z-rotational motion about z-axis. 84

Chapter 1

Introduction

The lithography process in the semiconductor manufacturing industry is discussed in 1.1, and the challenges in this area are introduced. Besides, a literature review for the contributions that have been done to enhance the lithography process is discussed in 1.1.5. Since this work aims to enhance the lithography process by proposing a smart materials-based reticle (SMBR) which is designed by a flexure hinge-based mechanism, a literature review for the in-plane flexure mechanisms is established in this chapter, this includes the x-y-flexure mechanisms in 1.2.1 and x-y-θ_z-flexure mechanisms in 1.2.2. In addition, as the proposed SMBR implements piezoelectric actuators, a brief discussion about such actuators has been included in 1.3. This chapter ends with our research objectives in 1.4 and thesis outline in 1.5.

1.1 Semiconductor Manufacturing

In semiconductor manufacturing, optical lithography machines are used to produce nanometric integrated circuits (ICs). As illustrated in Figure 1.1, these devices use an optical system to print an image of integrated circuits onto a silicon disk, known

as *wafer*, which is coated with a light-sensitive material [1]. The integrated circuit pattern exists on a quartz plate, called *reticle* [2], part of the reticle stage motion control system. The semiconductor industry seeks to manufacture a higher number of electronic circuits within one chip [2], in order to enhance the storage capacity, the functionality of the devices, and the CPU processing capability [2,3].

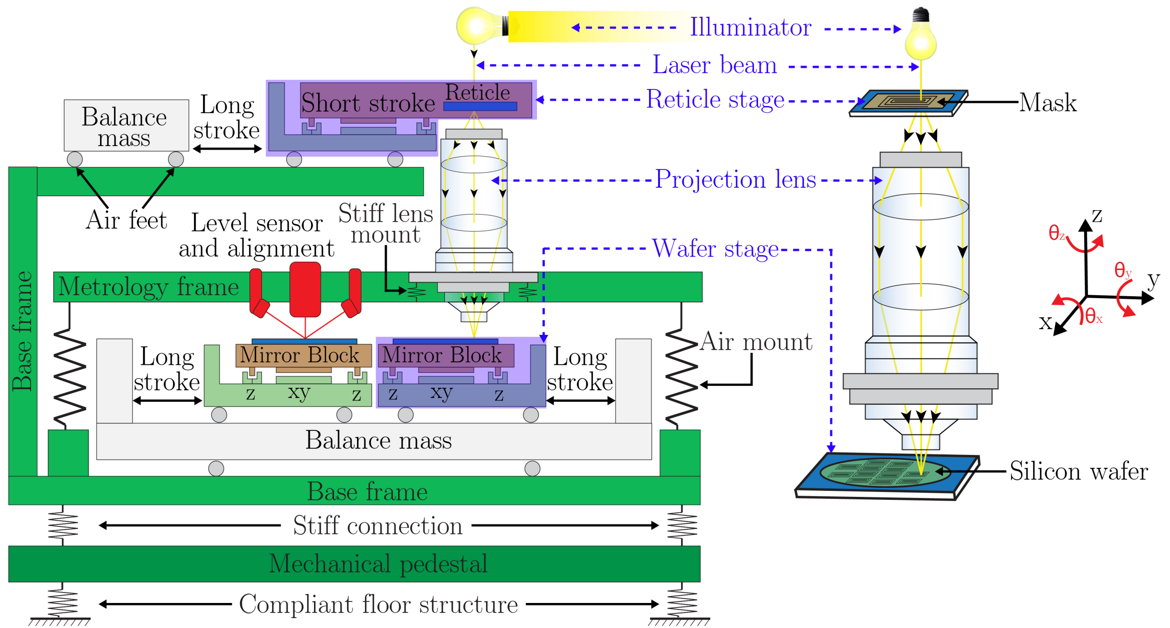

Figure 1.1: A schematic representation of the lithography machine architecture, which consists of three main parts: (i) the reticle stage, (ii) the projection lenses, and (iii) the wafer stage. The y-direction represents the scanning direction, and the reticle stage is our working scope.

As depicted in Figure 1.2, the step-and-scan technique is adopted in the lithography machines; a small rectangular area of the wafer, known as *die*, is exposed while the wafer is moving by the wafer stage. Simultaneously, the reticle moves by the reticle stage in the opposite direction of the wafer's movement direction.

As illustrated in Figure 1.2(b), each exposure represents a projection (scanning) for a single die. Once the projection of a single die is accomplished, the wafer stage

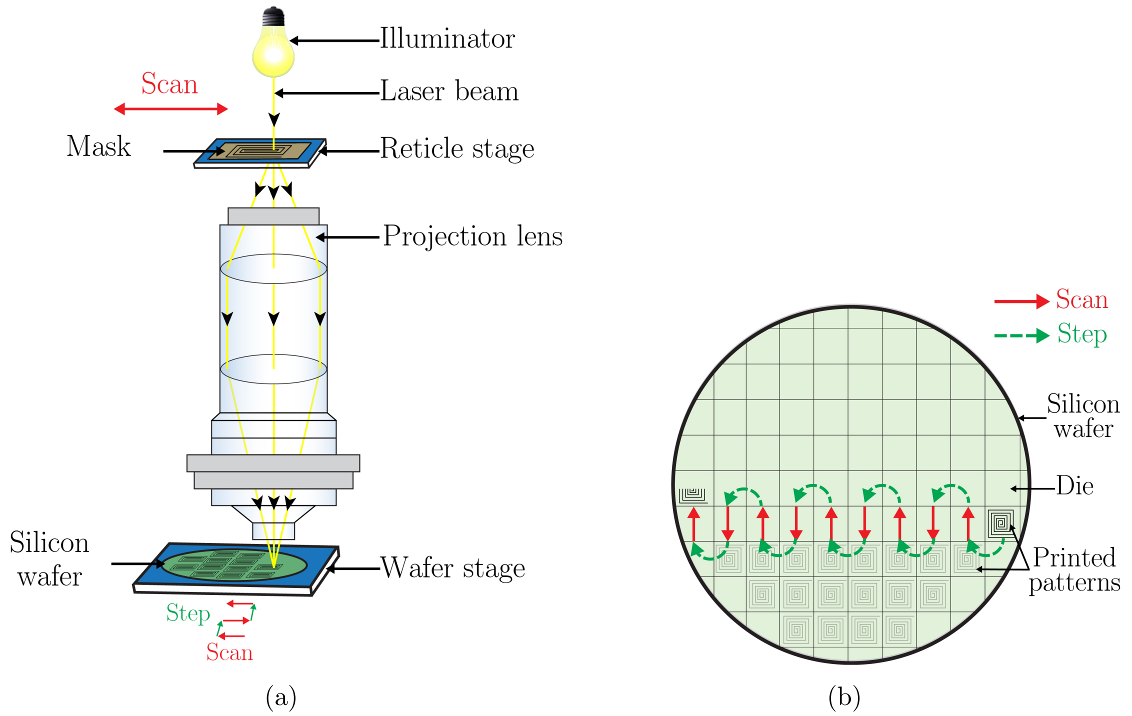

Figure 1.2: Basic principle of lithography process: (a) basic layout of the machine, and (b) part of the step-and-scan exposure profile across the dies on a silicon wafer.

moves the wafer to a next die location (stepping) [4, 5]. The exposure of a moving reticle has several advantages over the exposure of a stationary reticle [6], as discussed below.

Since the reticle is moving, every point in the pattern is exposed over the full width of the exposure slit. Hence, the positioning errors induced by the projection lens is compensated by an opposite error in another part of the slit. Consequently, in the case of random errors, these errors will average out.

In addition, the lenses in the projection lens box have a circular cross-section. However, exposing the silicon wafer in circular dies is inefficient because large portions of the wafer will not be exposed in this case. For this reason, the dies on the silicon wafer always have rectangular shapes. Having the reticle stage moving in a scanning fashion allows the utilization of larger pattern sizes without increasing the cost and

the size of the lenses, and consequently, maximizes the size of the image field.

1.1.1 Precision Requirements in Semiconductor Manufacturing Machines

There are four main measures which determine the precision requirements of lithography machines. These are *Critical Dimension*, *Overlay*, *Productivity*, and *Fading* [6]. An explanation for these measures is provided below.

The first measure is the critical dimension (CD). It is defined as the minimum attainable feature size in a printed Integrated Circuit, IC. Equation (1.1) expresses the achievable CD or resolution in lithography machines.

$$\mathrm{CD} = \mathrm{k}_1 \frac{\lambda}{\mathrm{NA}} \tag{1.1}$$

where k_1 is a process parameter that varies between 0.25 and 1 [3], λ is the wavelength of the illumination light, and NA is the Numerical Aperture of the lens which depends on the light's collecting-angle by the lens, and the type of medium between the lens and the wafer.

The second measure is the overlay. It is defined as the horizontal position difference between any consecutive layers in a printed IC. This type of flaw has an impact on the IC's electrical properties, and it could result in short circuits if it exceeded its limit value, 15% of the CD value [6].

The third measure is the productivity. This measure is influenced by some factors, such as machine reliability and throughput [3]. The later is defined as the maximum number of wafers that can be exposed within one hour. Thus, productivity can be defined as the maximum number of good exposures per unit time. While the productivity is more meaningful for the customers, the throughput is more practical

and efficient to use in the machine design process.

The fourth measure is the fading. It is defined as "the lack of contrast due to the vibrations of the machine during exposure" [6]. Such vibrations could exist due to the high velocity and acceleration of the positioning stages in lithography machines.

The above discussion highlights the lithography process's main components and the precision requirements in semiconductor manufacturing machines. Further details about how the precision requirements are achieved in lithography machines are presented in Section 1.1.2.

1.1.2 Attaining the Precision Requirements in Lithography Machines

At the beginning of each die location, the wafer and reticle stages are allowed to settle until the alignment positioning errors between the wafer and reticle stages become small enough before turning the illuminating light on [7]. The reticle and the wafer position are simultaneously controlled through positioning stages, the reticle and wafer stages, respectively [8]. During the scanning process, both the reticle and the wafer stages must track a challenging reference trajectory in x-, y-, z-, θ_x-, θ_y-, and θ_z-directions.

Attaining high precision and large stroke requirements in the field of lithography cannot be achieved using a single type of actuator [3]. Hence, the semiconductor manufacturing machines adopt a dual-stage structure, where large range micron-scale movements are accomplished by the long-stroke stage using commutating actuators capable of strokes up to 1 meter. In contrast, small range nano-scale dynamic tracking and positioning are conducted by the short-stroke stage using Lorentz actuators with a stroke of up to 1 millimeter [9]. As a result, the semiconductor manufacturing machines can cover a large range with high positioning accuracy [10].

Any positioning error in the synchronization motion between the reticle and the wafer stages leads to in-plane and/or out-of-plane shifting of the formed pattern on the wafer and, consequently, degrades the efficiency of the ICs [11].

There are many sources that induce positioning errors in lithography machines. Further details about these sources are presented in Section 1.1.3.

1.1.3 Sources of Positioning Uncertainties in Lithography Machines

1.1.3.1 Air-bearings

In ultra-precision positioning stages, air-bearings are widely used because of its capability of providing a motion platform with less contamination, zero hysteresis, and zero friction or wear in nano-level motions [12]. However, due to the airflow high-speed, air vertices will be generated within the air-bearing, which sequentially will induce small vibration in the positioning stage [13]. As a result, the overall moving and positioning accuracy of the ultra-precision positioning stage will be reduced [14], and self-excited instabilities may occur, which could damage the whole positioning stage [15]. These small vibrations induced in the air-bearing deteriorate the fabrication processes that require nanometric moving and positioning accuracy.

1.1.3.2 Voice Coil Actuators with the Presence of Magnetic Suspension System

Magnetic suspension positioning stages with voice coil actuators are widely used in ultra-precision systems where ultra-high precision movement over a micro-scale is required [16, 17]. The magnetic suspension system is used to compensate the gravity of the stage. However, the implementation of such system introduces some problems.

For example, placing multiple actuators close to each other with the presence of the magnetic suspension system results in electromagnetic cross-talk between these actuators and balance magnets [18].

1.1.3.3 Other Sources of Positioning Uncertainties

There are many other sources contribute to the positioning errors and affect the positioning accuracy in lithography machines. For example, the actuator's thrust fluctuation, measurement noise, and machining errors of the coils and magnets will induce uncertainties and modeling errors. Moreover, the uneven air gap thickness and cable forces will cause disturbances in the long-stroke stage motion, which is also coupled to the short-stroke stage to a certain extent [7]. These modeling errors and disturbances will profoundly affect the positioning accuracy of the ultra-precision positioning stages.

Focusing and leveling processes in lithography machines are essential to enhance the exposure quality on the wafer. Hence, both the short- and long-strokes of the wafer and reticle stages posses 6-DoF to achieve the required focusing and leveling. However, these stages have cross-coupled kinematics between each axes [19]. Consequently, the vertical adjustments of the stages have a significant impact on the horizontal motions of the stage, which causes uncertainties in the positioning accuracy that degrade the quality of the printed IC.

1.1.4 Error Classification and Prevention Techniques in Lithography Machines

The low-frequency positioning errors[1]that causes overlay and defocus errors, and the high-frequency positioning errors[2]that causes image fading can be classified into translation, rotation, magnification, and trapezoid errors [5], as illustrated in 1.3. These positioning errors can be compensated by adjusting the reticle stage position [11].

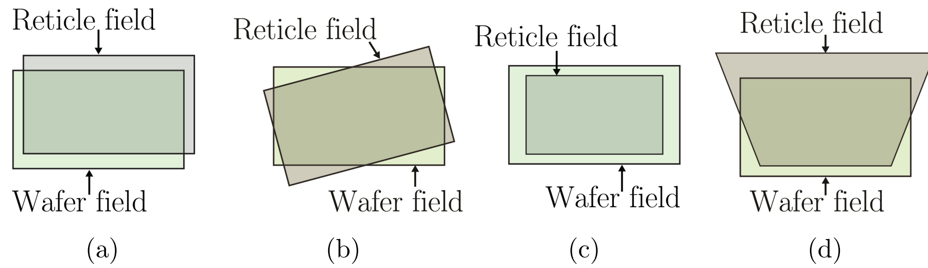

Figure 1.3: Illustration of positioning error classifications in lithography process: (a) translational (or overlay) error; the reticle field is shifted along x- and y-axes, (b) rotational error; the reticle field is rotated around z-axis, (c) magnification error; the reticle field is shifted along z-axis, and (d) trapezoid (or tilting) error; the reticle field is rotated around x- and/or y-axes.

Hence, since the positioning accuracy of the reticle and the wafer is very critical to produce efficient IC [11], and since the synchronized motion between the reticle and the wafer stages is essential to avoid the focus and overlay errors, then minimizing the relative positioning error between the two stages in the 6-DoF is considered as the main performance requirement in lithography process [20].

The dynamic architecture of lithography machines is designed to isolate all non-deterministic dynamic disturbances from the optical imaging system [6]. As demonstrated in Figure 1.1, in order to reduce the impact of the vibrations, a mechanical

[1]it is known as Moving Average (MA) error.
[2]it is known as Moving Standard Deviation (MSD) error.

pedestal, which is made from solid concrete, is utilized to connect the wafer scanner with the floor, which is made from steel bars. In this way, the pedestal will effectively mount the wafer scanner on the compliant floor structure. Also, a rigid base frame made of steel is utilized to fix all wafer scanner components. This base frame is directly mounted on the pedestal without additional vibration isolation measures. In addition, since the metrology frame firmly holds the projection lens, three air mounts[3]are utilized between the base-frame and the metrology frame to reduce the transmission of vibrations between these frames. Moreover, the reticle and wafer stages are supported by the base frame through either air-bearings or active magnetic support to ensure having motion with less contamination, zero hysteresis, and zero friction or wear [12]. Besides, the balance masses, which float over air foot, are utilized to absorb the machine's reaction forces that are in the order of several kilo Newton [6].

1.1.5 The Contributions to Enhance the Performance of Lithography Process

A number of studies contribute to enhance the lithography process. An iterative feedback tuning (IFT) approach is developed in [1] with robustness constraints; such that, robust stability is guaranteed while requiring only a nonparametric model. The developed model was applied on the wafer stage in the lithography machine, and the obtained results confirm improved performance and guaranteed robustness estimates. In [17], combined system identification and robust control design framework is developed for high-performance precision motion systems where the throughput and accuracy are critical measures. A data-based multi-input multi-output (MIMO) feedforward control design is applied in [21] to the motion systems of a wafer scanner.

[3]Air cushion springs with a very high stiffness.

The proposed control design is capable of dealing with unknown disturbances and minimizing its effect on the performance variables. In [22], data-based feedforward control is developed for the wafer stage in lithography machines to improve the scanning performances, including the settling behavior and reducing the cross talk effect. In [23], a novel synchronization control structure is proposed in order to enhance the synchronization performance and reduce the synchronization error between the reticle and the wafer stages.

Since the magnetic suspension system in the reticle stage causes coupling between its multiple degrees of freedom, an adaptive sliding mode control method is presented in [24] to improve the convergence of the tracking errors. By compensating the modeling errors and external disturbances, the proposed controller effectively reduced (i) the coupling in the stage, (ii) the tracking errors in the scanning direction, and (iii) the positioning errors in other multiple DoF.

By implementing fourteen piezoelectric actuators (PZT) through two arrays of actuation mechanisms located at the edges of the reticle, a reticle curvature manipulator is proposed in [3] as a curvature correction technique in lithography machines. The proposed design reduces the focus error due to lens heating and wafer unflatness. Consequently, the estimated focus error reduction was approximately 10 nm. In [9], for the aim of achieving enhanced scanning accelerations, a new reticle clamping concept is investigated in which the reticle slip is eliminated, and non-correctable reticle deformation is reduced. The proposed reticle clamping concept avoids acceleration force transfer through friction and by employing struts into the reticle to constrain it kinematically. In [8], reticle slip is eliminated by employing piezoelectric stack actuators that exert controlled pushing forces on the reticle to cancel the inertial loads.

1.2 Compliant Mechanism Designs

Flexure hinge-based mechanism is a monolithic structure manufactured by removing certain parts from a one single piece of material to form elastic flexure hinges. The flexure hinges' elastic deformations help in realizing rotational or translational motion replacing traditional joints [25, 26], therefore the friction between the moving joints does not exist. Consequently, the flaws of creep and backlash during motion are eliminated in such mechanisms. Besides, this kind of mechanism has the features of no clearance and no lubrication needed; hence a high resolution can be realized. It also has the advantages of no hysteresis, ease of fabrication, and compactness, providing smooth motions, and its capability to achieve motions with nanometer-level resolution [27].

In general, the flexure hinge-based mechanisms can be designed with serial hinge connections, parallel hinge connections, or a combination of serial and parallel hinge connections. Comparing with the parallel stage, the series structure is easier to design and control, but its precision is not high. Because of this limitation in series structure, most micro-motion stages with high precision and resolution use parallel hinge connection. However, most of the proposed parallel stages have coupled motions, making the kinematic model complex and the precise control challenging to be realized. Thus, the parallel stages have the advantages of high rigidity, high load carrying capacity, high accuracy, and high velocity. However, it also suffers from the coupled motions and being difficult to control.

The flexure-based compliant mechanisms have been utilized in many applications for ultra-precision motions at the micro-/nano-levels. For example, in biological applications, amplifiers for piezoelectric actuators, ultra-precision scanning, and aligning and machining [28–31].

There are two main problems in the development of flexure-based compliant mechanisms. One issue is the large stroke and high precision positioning requirements. The other issue is to calculate the amplification ratio of the mechanisms accurately. The stiffness matrix method, which was proposed in [32], can be used to calculate the amplification ratio of the mechanism accurately. However, this method is complicated compared with the Pseudo-Rigid-Body model (PRBM) in which the rotational center shifting is ignored, thus, leading to inaccurate results. In general, there are three approaches used in the literature to design and analyze compliant mechanisms; the matrix method, finite element analysis (FEA), and topology design [33].

Significant efforts have been applied to design and analyze flexure-based compliant mechanisms. For instance, in [34], a 3-DoF flexure based parallel mechanism is designed for micro-/nano- manipulation, where its dynamics and kinematics were analyzed through the matrix method. A decoupled flexure-based x-y- parallel micromanipulator is proposed in [35], in which the matrix method was applied to evaluate the equivalent compliance of the proposed model.

In flexure-based compliant mechanisms, the load-deflection relationship became an evaluation criterion for the stiffness characteristics [36, 37]. An analytical model for the optimal design of a flexure-based displacement amplifier is proposed in [32], where the strain energy and Castigliano's displacement theorem were adopted to derive the displacement and stiffness equations. In [38], a lever displacement amplifier is designed and implemented in a dual-mode motion stage through the matrix method. The matrix method was utilized in [39,40] to derive the kinematic models of their proposed mechanisms, and the results of the finite element analysis and the experiment verified the analytical results.

In [39], finite element analysis is utilized to model a high-precision flexure-based mechanism driven by piezoelectric actuators. In [41], the topological approach is

employed to perform kinematic analysis for a multi-stage piezo stroke amplifier, and the FEA was utilized to verify their results. In [33], the principle of virtual work and the Pseudo-Rigid-Body model (PRBM) were adopted to derive the analytical model for the proposed design. More examples can be found in [42–45].

A number of studies proposed compliant micro-/nano- positioning stages. These studies can be classified into x-y-compliant stages, and x-y-θ_z-compliant stages. However, the performance of these stages is limited by the resonance frequency, the stiffness, the workspace, and the decoupling property. In addition, the stages with high resonance frequency possess high stiffness, and the stiffness would be in contradiction with the workspace and motion accuracy. Moreover, the stages possessing large stiffness need to be actuated by large-stiffness piezoelectric actuators. Therefore, it is necessary to develop a parallel micro-motion stage with high resonance frequency, relatively small stiffness, good decoupled property, and large workspace. Further details on some of the available compliant micro-/nano- positioning stages are presented in Sections 1.2.1 and 1.2.2.

1.2.1 x-y-Compliant Micro-/Nano- Positioning Stages

A number of studies proposed serial compliant micro-/nano- positioning stages. An x-y- serial stage is formed in [46], which has a workspace of 39.1 μm $\times$ 42.1 μm, this is achieved by composing two modular 1-DoF stages in a stack. In [47], a serial x-y- stage with a stacked structure is designed, with a resolution of 50 nm and a workspace of 80 μm $\times$ 80 μm. An embedded structure to design a planar serial x-y- stage is proposed in [48]. It provides a resolution of 50 nm and a workspace of 41.6 μm $\times$ 42.8 μm.

In addition, several parallel compliant micro-/nano- positioning stages are de-

signed. In [49], a 2-DoF flexure-based micro-motion stage for two axes' cooperative motion is designed, made from aluminum 7075 with symmetrical configuration, with a workspace of 18.03 μm $\times$ 18.03 μm. An approach based on graph theory is presented in [50] to obtain several possible configurations of a micro-/nano- positioning stage with a bridge-type amplification mechanism. Using this approach, several configurations were obtained for multi-DoF stages, and one configuration is chosen for further analysis. The workspace for the chosen stage is 434 μm $\times$ 435 μm $\times$ 286 μm for the displacements along x-, y-, and z-axes, respectively.

In [51], a 2-DoF compliant micro-motion stage that is made from aluminum 7075 is designed, and the first two natural frequencies are 233.83 Hz and 234.01 Hz. A decoupled micro-/nano- positioning stage with lever amplifiers is developed in [52]. The stage is symmetric along x- and y-axes, and it utilizes two symmetric lever displacement amplifiers to obtain large workspace by amplifying the output displacements of piezoelectric actuators. This micromanipulation stage has low cross-coupling (less than 0.1%), a large reachable workspace (169.6 μm $\times$ 165.3 μm), high stiffness and high bandwidth (the first natural resonant frequency is 348.31 Hz).

In [53], a 2-DoF x-y-stage is developed. Its planar size is 385 mm $\times$ 385 mm, and it has a workspace of 10 mm $\times$ 10 mm along x- and y-axes, respectively. However, the first resonant natural frequency is 18 Hz. a 2-DoF x-y-stage is developed in [54]. Its planar size is 300 mm $\times$ 300 mm, a workspace of 5 mm $\times$ 5 mm along x- and y-axes, respectively.

In [55], a 2-DoF x-y-stage is developed. Its planar size is 244 mm $\times$ 244 mm, and it has a workspace of 14 mm $\times$ 14 mm along x- and y-axes, respectively. However, the first resonant natural frequency is 20 Hz. A 2-DoF x-y-stage is developed in [56]. Its planar size is 214 mm $\times$ 214 mm, and it has a workspace of 10.5 mm $\times$ 10.5 mm along x- and y-axes, respectively. However, the first resonant natural frequency is 23 Hz.

In [57], a 2-DoF x-y-stage is developed. Its planar size is 61 mm $\times$ 61 mm, and it has a workspace of 127 μm $\times$ 127 μm along x- and y-axes, respectively, and the first resonant natural frequency is 200 Hz. In [58], a 2-DoF x-y-stage is developed. Its planar size is 130.9 mm $\times$ 130.9 mm, and it has a workspace of 125 μm $\times$ 125 μm along x- and y-axes, respectively, and the first resonant natural frequency is 740 Hz. a 2-DoF x-y-stage is developed in [59]. Its planar size is 2.6 mm $\times$ 2.6 mm, and it has a workspace of 225 μm $\times$ 225 μm along x- and y-axes, respectively, and the first resonant natural frequency is 400 Hz. Another 2-DoF compliant stage is proposed in [60], but the design was unsymmetrical, and it has a limited operating frequency that is relatively low for the scanning applications. Moreover, the cross-talk between the x- and y-axes was 5.4 %

1.2.2 x-y-θ_z-Compliant Micro-/Nano- Positioning Stages

In [61], a 3-DoF x-y-θ_z-stage is developed. It has a workspace of 283.13 μm $\times$ 284.78 μm $\times$ 8.73 mrad for the translational displacements along x- and y-axes, and the θ_z-rotational motion around z-axis, respectively. The resonant natural frequencies for the translational motions along x- and y-axes is 243.09 Hz, and the resonant natural frequency for the rotational motion around z-axis is 405.52 Hz.

A 3-DoF x-y-θ_z-stage is proposed in [62], with a workspace of 147.84 μm $\times$ 137.96 μm$\times$3.75 mrad for the translational displacements along x- and y-axes, and the θ_z-rotational motion around z-axis, respectively. The first resonant natural frequency of the stage is 199.7 Hz.

In [63], a 3-DoF x-y-θ_z-stage is designed. It has a workspace of 36.5 μm $\times$ 32 μm $\times$ 1.24 mrad for the translational displacements along x- and y-axes, and the θ_z-rotational motion around z-axis, respectively. The first resonant natural frequency

of the stage is 349.8 Hz.

In addition, another 3-DoF x-y-θ_z-stage is designed in [64]. It has a workspace of 6.9 μm $\times$ 8.5 μm $\times$ 0.29 mrad for the translational displacements along x- and y-axes, and the θ_z-rotational motion around z-axis, respectively. The resonant natural frequencies for the translational motions along x- and y-axes is 629.3 Hz, while those for the rotational motion around z-axis is 522.5 Hz. In [65], a 3-DoF flexure-based micro-motion stage is proposed to perform x-y-θ_z motions, but it has large coupling during the y- and θ_z-motions and the x-, y-, and θ_z-motions appeared in the second, sixth, and seventh mode shapes, respectively.

1.3 Piezoelectric Actuators

In 1880 Jacques and Pierre Curie discovered that applying a pressure on certain types of natural monocrystalline materials, such as Quartz, Tourmaline, and Seignette salt, leads to generation of electric charges. This phenomenon is called *direct piezoelectric effect* or *sensor effect*. After that, they noticed that applying electrical fields on such types of materials led to mechanical deformations proportional to the applied voltage. This phenomenon is called *inverse piezoelectric effect* or *actuator effect*.

The piezoelectric effect of natural monocrystalline materials is relatively small. Hence, the industry improved these materials and introduced polycrystalline ferroelectric ceramics such as Barium Titanate ($BaTiO_3$) and Lead Zirconate Titanate (PZT) which has an improved piezoelectric effect, such that it provides larger deformations, or induce larger electrical voltages. In addition, the PZT piezo ceramic materials are commercially available in many modifications and can be customized based on customer needs, such that its piezoelectric and dielectric parameters can be specifically optimized based on the desired application.

The piezoelectric effect is used in many applications, such as lighters, loud speakers, and in the automotive technology where the transition times in combustion engines are reduced because of using the piezo-controlled injection valves, and consequently, it improves the smoothness and exhaust gas quality.

The piezoelectric actuators stiffness is a very important parameter that must be taken into considerations since it plays a major role in the generated force and resonant frequency. The piezoelectric actuators have very high stiffness (several hundred newtons per micrometer), and consequently, very high resonant frequencies (32 kHz-162 kHz).

Since the piezoelectric actuators have unique features, such as reasonably large output forces (up to a kilo-newton level) and strokes, compact size, swift response, high resolution, electrical mechanical coupling efficiency, low heat, continuous displacement, negligible backlash, no need for lubrication, high stiffness, and high precision [66, 67], these kinds of actuators are widely utilized in the micro-/nano- positioning stages, as mentioned earlier.

1.4 Contributions of the Thesis

Based on the previous discussion, in order to increase the capacity of memory chips and operating speeds of microprocessors, more functionality must be packed into each integrated circuit, IC. This can be achieved by increasing the number of printed ICs per square centimeter of wafer surface, and by decreasing the positioning errors that occur during the scanning process.

Several contributions have been made to enhance lithography machines. Up to this moment, there is no any study that proposes a regulating stage into the reticle stage which can compensate the existing errors in the lithography machine. In this work, a

smart materials-based reticle (SMBR) is designed and analyzed. The proposed SMBR is able to reduce the relative in-plane micro-positioning errors that exist in the synchronization motion between the reticle and wafer stages in the current lithography machines. This is achieved by integrating x-y high-speed piezoelectric actuators into a novel parallel flexural hinge-based mechanism. The proposed mechanism transfers the output displacements of the piezoelectric actuators to move the reticle with the required in-plane displacements necessary to correct the existing in-plane synchronization errors in lithography machines. In this way, the precision of the lithography process can be highly improved.

Since the reticle stage in the current semiconductor manufacturing machines has an operating frequency bandwidth of more than 2 kHz and settling time of 10 ms [2,3], the proposed SMBR is designed to be able to correct the in-plane errors in a time period less of than 10 ms. In addition, the proposed SMBR is designed to have a high working frequency (550 Hz is chosen in the design process) in order not to decrease the working frequency of the current lithography machines.

1.5 Outline of the Thesis

The remaining of the thesis is organized as follows: Chapter 2 illustrates the mechanism design, modeling, and optimization of the proposed SMBR, where a description of the proposed SMBR and its working principle is discussed, and analytical models of the proposed SMBR are derived. These analytical models include compliance, static, stress, and modal analyses. The analytical analyses are verified by the Finite Element Method (FEM) using *ANSYS* in the same chapter. In addition, this chapter includes the dimensional optimization of the proposed SMBR to meet the design requirements.

A dynamic model of the proposed SMBR (including the piezoelectric actuators)

and the short-stroke is presented in Chapter 3. The dynamic characteristics of the entire stage[4] are illustrated in this chapter, and the working frequency bandwidth is verified. The transfer functions of the whole stage have been determined, and three case scenarios are introduced to demonstrate how the proposed SMBR corrects the micro-positioning errors in the synchronization motion between the reticle and wafer stages. Finally, conclusions are drawn in the last chapter.

[4] including the proposed SMBR, the piezoelectric actuators, and the short-stroke

Chapter 2

Mechanism Design, Modeling, and Optimisation

In this chapter, the flexure mechanism design of a novel smart materials-based reticle (SMBR) is proposed in Section 2.2, and its working principle is presented in Section 2.2.1. In addition, the analytical modeling of the proposed SMBR is accomplished, which includes (i) compliance analysis in Section 2.3, (ii) static and stress analyses in Section 2.4, and (iii) modal analysis using Lagrange's approach in Section 2.5. All these analyses are verified by the finite element method (FEM) using *ANSYS*. After that, the dimensional optimization is conducted in Section 2.6 to minimize the settling time of the proposed SMBR.

2.1 Introduction

In this chapter, a novel flexure hinge-based mechanism will be designed such that it satisfies the below specifications:

- It must have the ability to perform in-plane translational motions along x- and

y-axes, and θ_z-rotational motion around z-axis.

- It must acquire high resonant frequencies, greater than 550 Hz, in order to be utilised within the lithography machine that has high operating frequency band-width.

- The desired degrees of freedom (DOF) must appear at the first three mode shapes of design in order to avoid any parasitic mode shape at low frequencies.

- The coupling effect between the desired in-plane translational motions along x- and y-axes must be minimised.

The mechanism design of the proposed SMBR is introduced and justified in this chapter. The operating principle of the proposed SMBR is then explained considering three case scenarios, including

1. in-plane translational motions along x- or y-axes,

2. in-plane θ_z-rotational motion around z-axis, and

3. a combination of the in-plane translational and rotational motions.

The specifications of the proposed SMBR and its ability to simultaneously perform in-plane translational and rotational motions are further discussed in this chapter.

The static properties of the proposed SMBR are analyzed in terms of compliance, workspace, and stress in order to determine its main characteristics. The stiffness of the proposed SMBR is investigated based on Castigliano's second theorem. The static and stress analysis are thereafter studied by deriving analytical models, which are verified by FEM using *ANSYS*. The workspace and the safety factor of the proposed SMBR are then determined.

Using the Lagrange approach, the dynamic equation of undamped free vibration of the proposed SMBR is derived for conducting the modal analysis. FEM then verifies the modal analysis carried out by the Lagrange approach. In addition, the effect of implementing the piezoelectric actuators in the proposed SMBR is investigated.

The optimum dimensions of the proposed SMBR are finally defined using Grey Wolf Optimizer (GWO) to minimize the settling time of the proposed SMBR. This has been done after an extensive parametric study applied to the proposed SMBR in order to determine the parameters that have the most influence on the settling time.

The chapter ends with expressing the in-plane output displacement of the proposed SMBR in terms of the input voltages supplied to the piezoelectric actuators.

2.2 Mechanism Design for the Proposed Smart Materials-Based Reticle

This section states the mechanism design of the proposed SMBR. The layout of the proposed SMBR is demonstrated in Figure 2.1. As can be observed, a flexure hinge-based mechanism is adopted to design the proposed SMBR. The elastic deformation of the flexure hinges ensures achieving rotational and translational motions without using the traditional joints. In addition, the inherent advantages of no clearance and no lubrication needed for flexure hinge-based mechanisms will lead to a high resolution. It also has the advantages of no hysteresis, ease of fabrication, and compactness [68].

The proposed SMBR consists of twelve limbs, a mobile platform that holds the squared reticle with 152.3 mm side length, and a fixing base frame. Besides, twelve ($P - 888.91$[1]) piezoelectric actuators by *Physik Instrumente* are proposed to be im-

[1] Highly Reliable Multilayer Piezoelectric Actuator provided by the Physik Instrumente company.

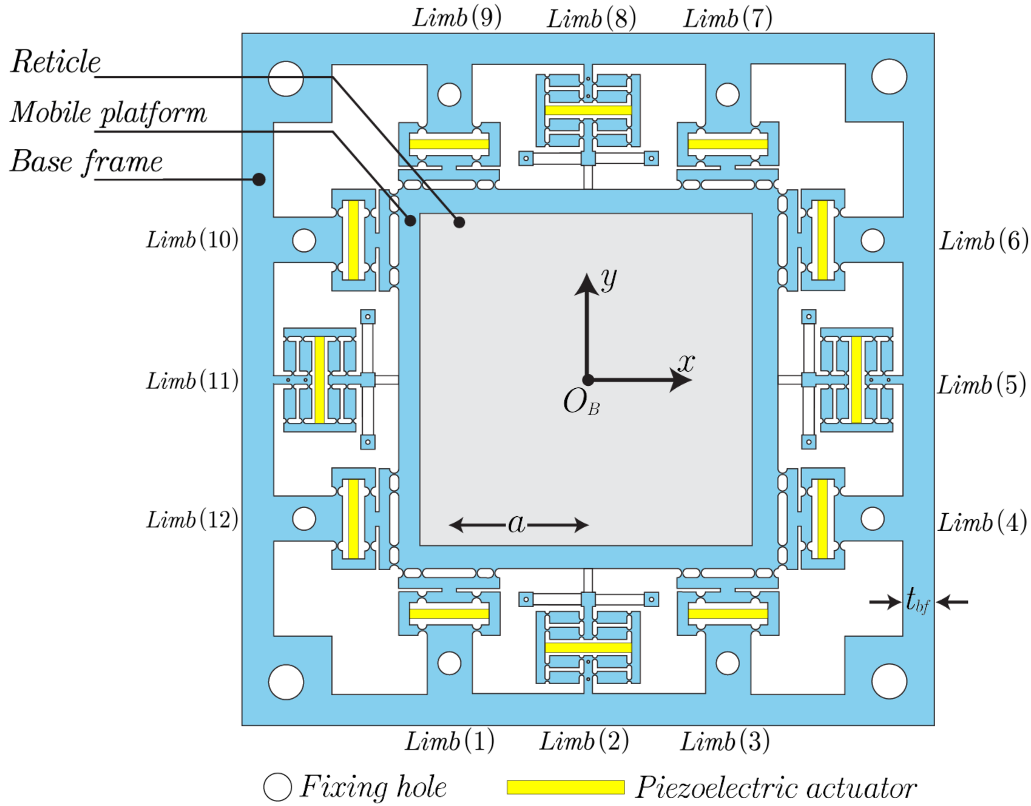

Figure 2.1: The proposed SMBR

plemented in order to provide the proposed flexure hinge-based mechanism with the required forces to move the reticle. This kind of actuator is utilized because the structure has large stiffness, and it requires large input forces. Besides, this type of actuator has low mass (can be less than 20 g), high reliability, excellent dynamics, and it can provide micrometer output displacement with a time constant of micro-seconds and displacement resolution of sub-nanometers.

All the limbs are connected to the mobile platform in parallel to assure having high precision, resolution, accuracy, velocity, rigidity, and load-carrying capacity [69]. Each limb employs multiple flexure hinges to transmit the motion from the piezoelectric

It is made from PIC252 ceramic. Its dimensions are 10 mm × 10 mm × 36 mm. It can provide an output displacement up to 38 μm, and a maximum force of 3800 N. Its stiffness is 100 N/μm, and its resonant frequency is 40 kHz.

actuators to the mobile platform. The input displacement of the piezoelectric actuator is transmitted as a vertical output displacement at the output end of the limb through these hinges. Besides, some limbs utilize right-circular flexure hinges, and others utilize leaf springs orthogonal to the lower part of the limbs to increase the stiffness along the x- and y-axes. This increases the natural frequencies of the proposed SMBR, which is essential in this work since the proposed SMBR will be integrated into the semiconductor manufacturing machines, which have working frequencies above 2 kHz. Some limbs utilize lateral leaf springs to attain a decoupling property in the in-plane translational motions along x- and y-axes. Compared with the other types of flexure hinges, the right-circular flexure hinges possess the smallest magnitude of center-shift value. Hence, this type of hinges is adopted in the proposed SMBR.

The limbs are bonded to the fixing base frame that is fixed on a stationary frame with fixing holes. This avoids the out-of-plane parasitic motion along the z-axis. The proposed SMBR has a double symmetric property along the x- and y-axes in order to guarantee a low value of cross-axis coupling error between these axes (to ensure good output decoupling property). Besides, the monolithic structure of the proposed SMBR possesses the advantage of easing the manufacturing process.

Limbs 2, 5, 8, and 11 are placed in the proposed SMBR in such a way that the actuation axes of the piezoelectric actuators at these limbs intersect at one common point at the center of gravity (CoG) of the reticle, O_B. This scheme is adopted to avoid any undesired internal moment when the piezoelectric actuators in these limbs are activated. As a result, activating these actuators provide pure in-plane output translational motions along x- and y-axes, without any rotation around z-axis. On the other hand, the other limbs, namely limbs 1, 3, 4, 6, 7, 9, 10, and 12, are placed in such a way that the actuation axes of the piezoelectric actuators in these limbs are apart from the center of gravity (CoG) of the reticle with a distance

a, in order to generate the required internal moment for producing a pure in-plane output θ_z-rotational motion around z-axis when activating those actuators, without any translational motions along x- or y-axes.

7075 Aluminum is chosen as the material of the flexure hinge-based mechanism because of its machinability and favorable density-to-stiffness ratio [70]. However, the material of the reticle is kept to be *Fused Silica* due to its low coefficient of thermal expansion (CTE) and transparency for the illumination light in the lithography process [3].

2.2.1 Stage's Working Principle

As depicted in Figure 2.2, the stage has three DOFs arising from (i) in-plane output translational motion along x-axis, which can be accomplished by activating PZTs 5 and 11 in opposite directions; (ii) in-plane output translational motion along y-axis, realized by activating PZTs 2 and 8 in opposite directions; and (iii) in-plane output θ_z-rotational motion around z-axis, accomplished by activating PZTs 1, 4, 7, and 10 in a certain direction, and PZTs 3, 6, 9, and 12 in the opposite direction. The other DOFs (out-of-plane translational motion along z-axis, θ_x-rotational motion around x-axis, and θ_y-rotational motion around y-axis) are constrained.

It is noteworthy that the in-plane output translational motions along x- and y-axes, and the in-plane output θ_z-rotational motion around z-axis can be achieved all at the same instant by activating a proper combination of piezoelectric actuators. For example, suppose that the workspace of the proposed SMBR is denoted by $\delta_{\max,x} \times \delta_{\max,y} \times \delta_{\max,\theta_z}$, and the maximum stroke of the piezoelectric actuators is denoted by $q_{\max}$ then:

- To achieve a pure in-plane output translational motion along x-axis with an

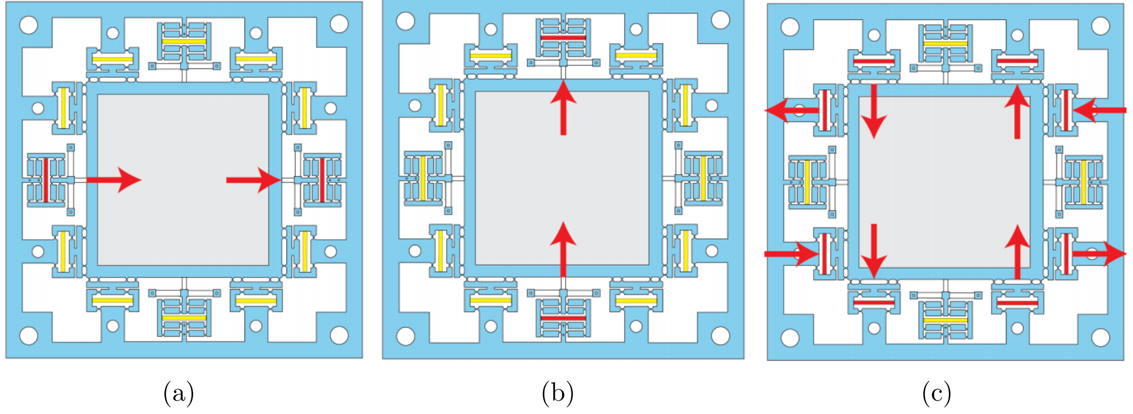
(a) (b) (c)

Figure 2.2: The proposed SMBR's operation principle in the xy-plane: (a) the in-plane output translational motion along x-axis, (b) the in-plane output translational motion along y-axis, and (c) the in-plane output θ_z-rotational motion around z-axis. *The red bars represent the active piezoelectric actuators, whereas the yellow bars represent the inactive actuators.*

amount of $\delta_{\max,x}$, the piezoelectric actuators in limbs 5 and 11 must be activated with its maximum stroke ($q_{\max}$) while keeping the remaining actuators unactivated.

- To achieve a pure in-plane output θ_z-rotational motion around z-axis with an amount of $\delta_{\max,\theta_z}/2$, the piezoelectric actuators in limbs 1, 4, 7, and 10 must be activated with half stroke ($q_{\max}/2$) in a specific direction, and the piezoelectric actuators in limbs 3, 6, 9, and 12 in the opposite direction, while keeping the remaining actuators unactivated.
- To achieve a combination motion of in-plane output translational motions along x- and y-axes, and in-plane output θ_z-rotational motion around z-axis with an amount of $\delta_{\max,x}$, $\delta_{\max,y}$, and $\delta_{\max,\theta_z}$, all piezoelectric actuators must be activated with its maximum strokes ($q_{\max}$). Consequently, in order to achieve a combination motion of in-plane output translational motions along x- and y-axes, and in-plane output θ_z-rotational motion around z-axis with certain

amount and direction, all piezoelectric actuators must be activated with the required stroke values and directions.

2.3 Compliance Analysis

In most previous work in literature, the motion of the flexure hinge-based mechanisms is considered to be obtained from the elastic deformation of the flexure hinges, while the links are regarded as rigid bodies [26]. However, in this work, the links and reticle stiffness have been taken into consideration although they have higher stiffness compared with the flexure hinges stiffness. The presence of the reticle inside the proposed flexure hinge-based mechanism is a payload that has a major effect on the resulted in-plane output motions of the flexure mechanism.

Figure 2.3 illustrates the layout of the right-circular flexure hinge and rectangular flexure hinge, respectively. These hinges have six DOFs, with a 6×6 compliance matrix, $\mathbf{C}_i$.

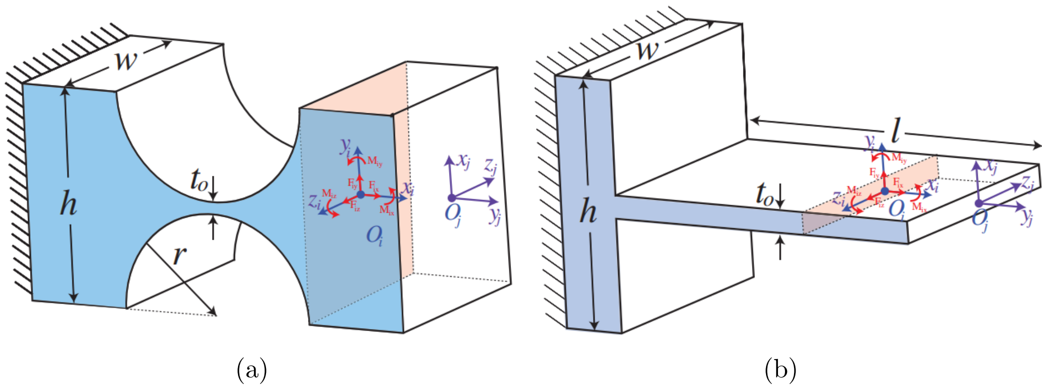

Figure 2.3: The flexure hinges used in the proposed stage: (a) right-circular flexure hinge, and (b) rectangular flexure hinge (leaf spring).

To determine the compliance entries of the flexure hinges, Castigliano's second theorem is adopted in [26] and [71] to derive the compliance matrix for flexure hinges; such that the equation that relates the hinge's deformations of a flexure hinge with the corresponding wrench can be expressed as

$$\begin{bmatrix} u_i \\ v_i \\ w_i \\ \theta_{x_i} \\ \theta_{y_i} \\ \theta_{z_i} \end{bmatrix} = \begin{bmatrix} C_{ui,F_{xi}} & 0 & 0 & 0 & 0 & 0 \\ 0 & C_{vi,F_{y_i}} & 0 & 0 & 0 & C_{vi,M_{zi}} \\ 0 & 0 & C_{wi,F_{zi}} & 0 & C_{wi,F_{y_i}} & 0 \\ 0 & 0 & 0 & C_{\theta xi,M_{xi}} & 0 & 0 \\ 0 & 0 & C_{\theta y_{i},F_{zi}} & 0 & C_{\theta y_{i},M_{y_i}} & 0 \\ 0 & C_{\theta zi,F_{y_i}} & 0 & 0 & 0 & C_{\theta zi,M_{zi}} \end{bmatrix} \begin{bmatrix} F_{x_i} \\ F_{y_i} \\ F_{z_i} \\ M_{x_i} \\ M_{y_i} \\ M_{z_i} \end{bmatrix} \tag{2.1}$$

where u_i, v_i, w_i, θ_{x_i}, θ_{y_i}, and θ_{z_i} are the local deformations of a flexure hinge at point i along the x-, y-, and z-axes, and around x-, y-, and z-axes, respectively. F_{x_i}, F_{y_i}, F_{z_i}, M_{x_i}, M_{y_i}, and M_{z_i} are the wrench applied at the same point.

The local compliance matrix for the hinge, $\mathbf{C}_i$, is transformed to a common global frame chosen to describe the mechanism using $\mathbf{C}_i^j = \mathbf{T}_i^j \mathbf{C}_i \left(\mathbf{T}_i^j\right)^T$, where $\mathbf{T}_i^j$ is the transformation matrix from frame O_i to frame O_j. Then, these compliances which are connected with each other in serial and parallel configurations can be added together to obtain the equivalent stiffness of the flexure hinge-based mechanism.

2.3.1 Compliance Modelling for Limb 1

With reference to Figure 2.4, the compliance matrices of the ith hinge and the jth link are denoted by $\mathbf{C}_{H_i}$ and $\mathbf{C}_{L_j}$, respectively. Based on Figure 2.4(b), the compliance of the lower part of the limb (shaded in green) at point D_1, can be derived by considering

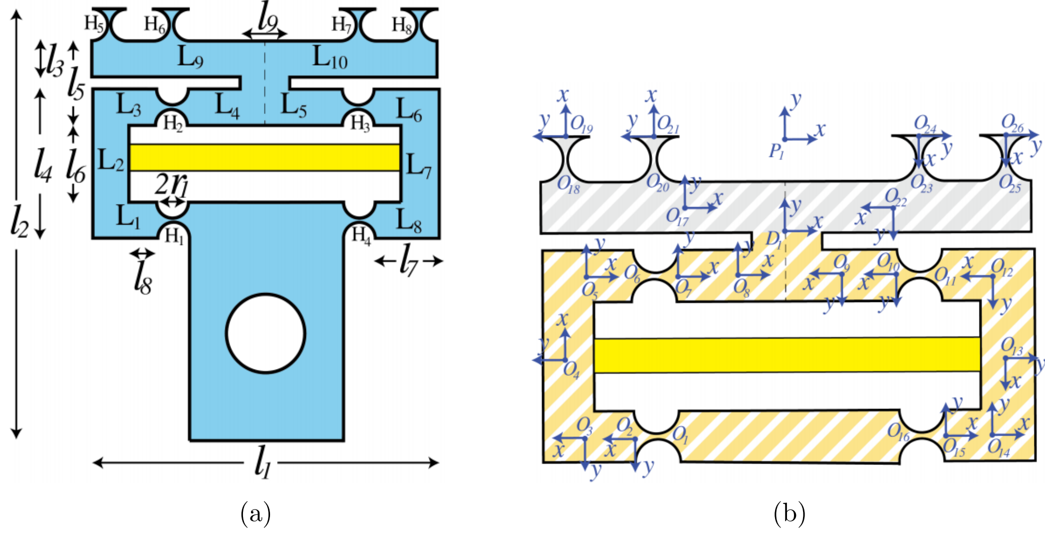

Figure 2.4: The design parameters and dimensions for limb 1: (a) the entire limb, and (b) the upper part of the limb.

the parallel connection between the two chains, $H_1L_1L_2L_3H_2L_4$ and $L_5H_3L_6L_7L_8H_4$.

$$\mathbf{C}_{D_1,l} = \mathbf{T}_2^{D_1}\mathbf{C}_{H_1}\left(\mathbf{T}_2^{D_1}\right)^T + \mathbf{T}_3^{D_1}\mathbf{C}_{L_1}\left(\mathbf{T}_3^{D_1}\right)^T + \mathbf{T}_4^{D_1}\mathbf{C}_{L_2}\left(\mathbf{T}_4^{D_1}\right)^T + \mathbf{T}_5^{D_1}\mathbf{C}_{L_3}\left(\mathbf{T}_5^{D_1}\right)^T + \mathbf{T}_7^{D_1}\mathbf{C}_{H_2}\left(\mathbf{T}_7^{D_1}\right)^T + \mathbf{T}_8^{D_1}\mathbf{C}_{L_4}\left(\mathbf{T}_8^{D_1}\right)^T \tag{2.2}$$

Similarly, $\mathbf{C}_{D_1,r}$ can be obtained. Hence, $\mathbf{C}_{D_1}$ can be expressed as

$$\mathbf{C}_{D_1} = \left[\left(\mathbf{C}_{D_1,l}\right)^{-1} + \left(\mathbf{C}_{D_1,r}\right)^{-1}\right]^{-1} \tag{2.3}$$

The compliance of the upper part of the limb (shaded in blue), at point P_1, with respect to point D_1, can be derived by considering the parallel connection between the two chains, $H_5H_6L_9$ and $H_7H_8L_{10}$, namely,

$$\mathbf{C}_{P_1,l}^{D_1} = \mathbf{T}_{19}^{P_1}\mathbf{C}_{H_5}\left(\mathbf{T}_{19}^{P_1}\right)^T + \mathbf{T}_{21}^{P_1}\mathbf{C}_{H_6}\left(\mathbf{T}_{21}^{P_1}\right)^T + \mathbf{T}_{17}^{P_1}\mathbf{C}_{L_9}\left(\mathbf{T}_{17}^{P_1}\right)^T \tag{2.4}$$

By the same token, $\mathbf{C}_{P_1,r}^{D_1}$ can be obtained. Then $\mathbf{C}_{P_1}^{D_1}$ can be derived:

$$\mathbf{C}_{P_1}^{D_1} = \left[\left(\mathbf{C}_{P_1,l}^{D_1} \right)^{-1} + \left(\mathbf{C}_{P_1,r}^{D_1} \right)^{-1} \right]^{-1} \tag{2.5}$$

Finally, the output compliance of the entire limb at point P_1 can be formulated as

$$\mathbf{C}_{\text{limb},1} = \mathbf{C}_{P_1}^{D_1} + \mathbf{T}_{D_1}^{P_1} \mathbf{C}_{D_1} \left(\mathbf{T}_{D_1}^{P_1} \right)^T \tag{2.6}$$

and consequently, $\mathbf{K}_{\text{limb},1} = \mathbf{C}_{\text{limb},1}^{-1}$.

2.3.2 Compliance Modelling for Limb 2

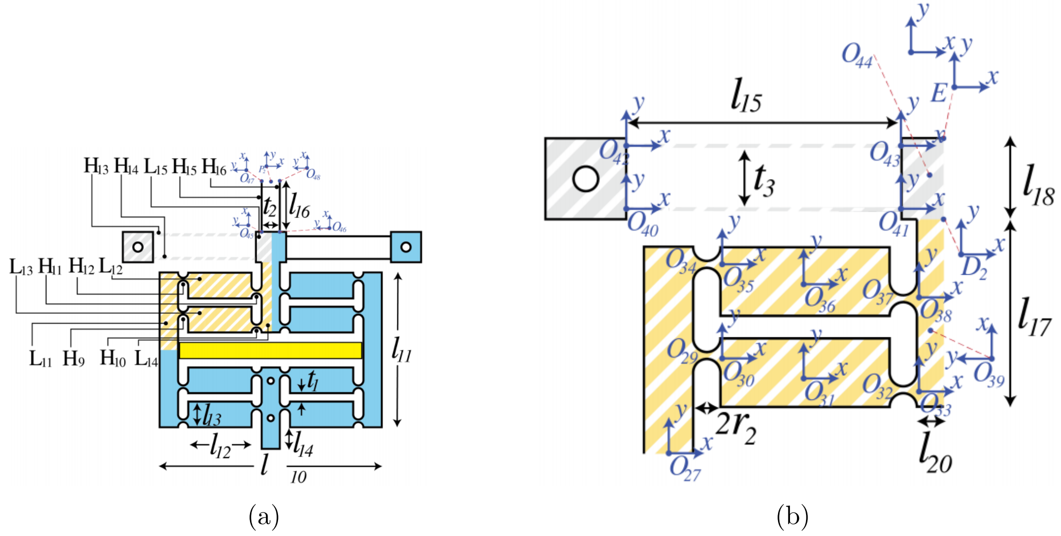

(a) (b)

Figure 2.5: The design parameters and dimensions for limb 2: (a) the entire limb, and (b) the top-left part of the limb.

As shown in Figure 2.5, since the amplifier has double symmetric property, left-right symmetry and up-down symmetry, the compliance matrix is derived for only one quarter of the amplifier. The compliance of the output point D_2 with respect to

the input point O_{27} for the top-left part of the amplifier can be derived considering the parallel connections between the two chains $H_9L_{12}H_{10}$ and $H_{11}L_{13}H_{12}$, namely,

$$\mathbf{C}_{D_2}^{29} = \mathbf{T}_{30}^{D_2}\mathbf{C}_{H_9}\left(\mathbf{T}_{30}^{D_2}\right)^T + \mathbf{T}_{31}^{D_2}\mathbf{C}_{L_{12}}\left(\mathbf{T}_{31}^{D_2}\right)^T + \mathbf{T}_{33}^{D_2}\mathbf{C}_{H_{10}}\left(\mathbf{T}_{33}^{D_2}\right)^T \tag{2.7}$$

Similarly, $\mathbf{C}_{D_2}^{34}$ can be obtained. Therefore, $\mathbf{C}_{D_2,tl}^{27}$ can be formulated as

$$\mathbf{C}_{D_2,tl}^{27} = \mathbf{T}_{28}^{D_2}\mathbf{C}_{L_{11}}\left(\mathbf{T}_{28}^{D_2}\right)^T + \left[\left(\mathbf{C}_{D_2}^{29}\right)^{-1} + \left(\mathbf{C}_{D_2}^{34}\right)^{-1}\right]^{-1} + \mathbf{T}_{39}^{D_2}\mathbf{C}_{L_{14}}\left(\mathbf{T}_{39}^{D_2}\right)^T \tag{2.8}$$

Since the amplifier has top-down and left-right symmetry, the compliance matrix of the whole amplifier can be derived as follows

$$\begin{aligned} \mathbf{C}_{D_2,l}^{27} &= \mathbf{C}_{D_2,tl}^{27} + \mathbf{T}_d^t\mathbf{C}_{D_2,tl}^{27}\left(\mathbf{T}_d^t\right)^T \\ \mathbf{C}_{D_2} &= \left[\left(\mathbf{C}_{D_2,l}^{27}\right)^{-1} + \left(\mathbf{T}_r^l\mathbf{C}_{D_2,l}^{27}\left(\mathbf{T}_r^l\right)^T\right)^{-1}\right]^{-1} \end{aligned} \tag{2.9}$$

where $\mathbf{T}_d^t$ and $\mathbf{T}_r^l$ are the transformation matrices that transform the compliance matrix from down to top and right to left parts of the limb, respectively. Considering the parallel connection between H_{13}, H_{14}, and L_{15}, the compliance of the left upper part at point E with respect to point D_2, can be derived as below

$$\mathbf{C}_{E,\,l}^{D_2} = \left[\left(\mathbf{T}_{41}^{E}\mathbf{C}_{H_{13}}\left(\mathbf{T}_{41}^{E}\right)^T\right)^{-1} + \left(\mathbf{T}_{43}^{E}\mathbf{C}_{H_{14}}\left(\mathbf{T}_{43}^{E}\right)^T\right)^{-1} + \left(\mathbf{T}_{44}^{E}\mathbf{C}_{L_{15}}\left(\mathbf{T}_{44}^{E}\right)^T\right)^{-1}\right]^{-1} \tag{2.10}$$

Hence, the compliance of the entire upper part of the limb at point E with respect to point D_2 can be expressed as

$$\mathbf{C}_{E}^{D_2} = \left[\left(\mathbf{C}_{E,\,l}^{D_2}\right)^{-1} + \left(\mathbf{T}_r^l\mathbf{C}_{E,\,l}^{D_2}\left(\mathbf{T}_r^l\right)^T\right)^{-1}\right]^{-1} \tag{2.11}$$

Considering the parallel connection between H_{15} and H_{16}, we obtain

$$\mathbf{C}_{P2}^{E} = \left[\left(\mathbf{T}_{47}^{P2} \mathbf{C}_{H_{15}} \left(\mathbf{T}_{47}^{P2} \right)^{T} \right)^{-1} + \left(\mathbf{T}_{48}^{P2} \mathbf{C}_{H_{16}} \left(\mathbf{T}_{48}^{P2} \right)^{T} \right)^{-1} \right]^{-1} \tag{2.12}$$

Finally, the output compliance of the entire limb at point $P2$ can be derived, namely,

$$\mathbf{C}_{\text{limb},2} = \mathbf{C}_{P2}^{E} + \mathbf{T}_{E}^{P2} \mathbf{C}_{E}^{D_2} \left(\mathbf{T}_{E}^{P2} \right)^{T} + \mathbf{T}_{D_2}^{P2} \mathbf{C}_{D_2} \left(\mathbf{T}_{D_2}^{P2} \right)^{T} \tag{2.13}$$

and consequently, $\mathbf{K}_{\text{limb},2} = \mathbf{C}_{\text{limb},2}^{-1}$.

2.3.3 Compliance Modelling for the Reticle

The compliance matrix of the reticle can be obtained by considering a rectangular plate made of fused silica. The 6×6 stiffness matrix for a rectangular plate is given by

$$\mathbf{K}_R = \begin{bmatrix} d_{11} & d_{12} & 0 & 0 & 0 & 0 \\ d_{12} & d_{22} & 0 & 0 & 0 & 0 \\ 0 & 0 & d_{66} & 0 & 0 & 0 \\ & & & D_{11} & D_{12} & 0 \\ & \text{sym} & & D_{12} & D_{22} & 0 \\ & & & 0 & 0 & D_{66} \end{bmatrix} \tag{2.14}$$

where $d_{11} = d_{22} = E_r w_r/(1 - {\nu_r}^2)$, $d_{12} = \nu_r d_{11}$, and $d_{66} = d_{11}(1 - \nu_r)/2$. Besides, $D_{11} = D_{22} = E_r w_r^3/12(1 - {\nu_r}^2)$, $d_{12} = \nu_r d_{11}$, $D_{12} = \nu_r D_{11}$, and $D_{66} = D_{11}(1 - \nu_r)/2$. In which w_r is the thickness of the reticle, E_r and ν_r being its Young's modulus and Poisson's ratio, respectively.

2.3.4 Compliance Modelling of the Entire Smart Materials-Based Reticle

As can be observed in Figure 2.1, all the limbs are connected to the reticle in parallel. Hence the output stiffness of the proposed SMBR (including the limbs and the reticle) can be expressed as

$$\mathbf{K}_B = \mathbf{K}_R^B + \sum_{i=1}^{12} \mathbf{K}_{\text{limb,i}}^B \tag{2.15}$$

where $\mathbf{K}_R^B$ is the equivalent stiffness matrix of the reticle expressed in the global frame O_B, and $\mathbf{K}_{\text{limb,i}}^B$ is the stiffness matrix of limb i expressed in the global frame O_B.

2.4 Static and Stress Analysis

The in-plane output displacements of the proposed SMBR under static loading can be determined by the equation below

$$\begin{bmatrix} K_x & K_{xy} & 0 \\ K_{yx} & K_y & 0 \\ 0 & 0 & K_{\theta_z} \end{bmatrix} \begin{bmatrix} x_{\text{out}} \\ y_{\text{out}} \\ \theta_{z\text{out}} \end{bmatrix} = \begin{bmatrix} f_x \\ f_y \\ M_{\theta_z} \end{bmatrix} \tag{2.16}$$

where f_x and f_y are the resultant input forces provided by the piezoelectric actuators along x- and y-axes, respectively, M_{θ_z} is the resultant input moment produced by the piezoelectric actuators around z-axis. Based on [70], the nominal displacement of the ith piezoelectric actuator can be expressed as

$$q_{p_i,n} = \frac{F_{p_i}}{k_{p_i}\left[1 - k_{p_i}/(k_{p_i} + K_{\text{load}})\right]} \tag{2.17}$$

where F_{p_i} and k_{p_i} are the force and stiffness of the ith piezoelectric actuator, respectively, and K_{load} is the stiffness of the load. As in [72], due to the high stiffness of the structure and the piezoelectric actuator, the actual output displacement of the piezoelectric actuator is

$$q_{p_i,a} = \frac{k_{p_i}}{k_{p_i} + K_s} q_{p_i,n} \tag{2.18}$$

where K_s is the equivalent output stiffness of the stage expressed in O_B, and the subscript s stands for the direction of motion that the piezoelectric actuator causes, namely, x, y, or θ_z. For example, with reference to Figure 2.6, the piezoelectric actuator in limb 2 is responsible for the in-plane output translational motion along y-axis. Hence, the actual output displacement of this piezoelectric actuator is

$$q_{p_2,a} = \frac{k_{p_2} q_{p_2,n}}{k_{p_2} + K_y} \tag{2.19}$$

The generated in-plane output motions are given by

$$x_{\text{out}} = q_{p_5,a} + q_{p_{11},a} + \Delta x \tag{2.20}$$

$$y_{\text{out}} = q_{p_2,a} + q_{p_8,a} + \Delta y \tag{2.21}$$

$$\theta_{z\text{out}} = \frac{1}{a} \sum_{m=i} q_{p_i,a} \tag{2.22}$$

where $i = 1, 3, 4, 6, 7, 9, 10, 12$, and a represents the horizontal distance between the line of actuation of the ith piezoelectric actuator and the center of gravity (CoG) of the reticle. $\Delta x = (F_{p_2} + F_{p_8})/K_{yx}$ and $\Delta y = (F_{p_5} + F_{p_11})/K_{xy}$ are the generated in-plane parasitic coupling motions along x- and y-axes, respectively.

In order to verify the derived analytical modelling, static analysis for the proposed SMBR is conducted using *ANSYS*. Figure 2.7 illustrates the primary in-plane output translational displacements along x- and y-axes, and the primary in-plane out-

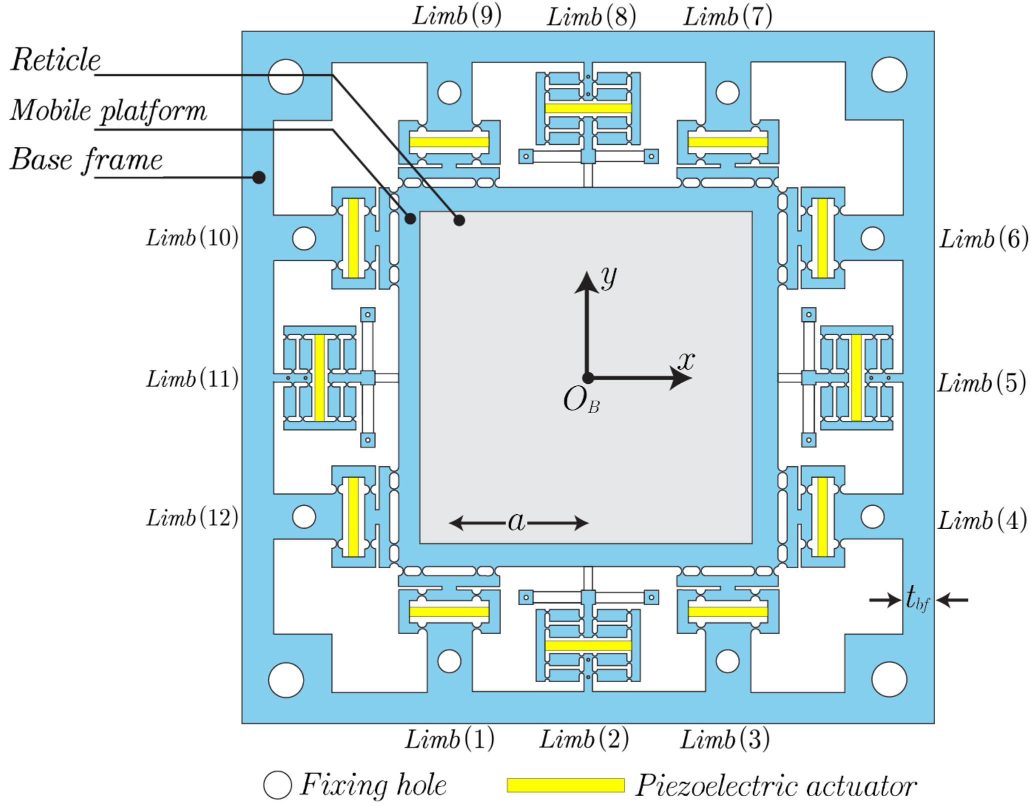

Figure 2.6: The proposed SMBR

put θ_z-rotation about z-axis, of the proposed SMBR under various values of loads. The maximum stroke of the piezoelectric actuators, $F_{p_i,\max}$, is set to be 2400 N. In addition, Figure 2.8 illustrates the parasitic in-plane coupling displacements of the proposed SMBR during the primary motion along x- and y-axes.

Based on Figure 2.7, the derived analytical model overestimates the translational in-plane output displacements of the proposed SMBR by 36.83%, and underestimates the rotational in-plane output displacements of the proposed SMBR by 22.08%. These deviations are mainly due to the approximations that have been adopted through calculating the equivalent stiffness matrix and the compliance entities. It is noteworthy that compensation factors (η_x, η_y, and η_θ) are adopted in order to take into consideration these deviations. Considering these factors, the analytical in-plane output

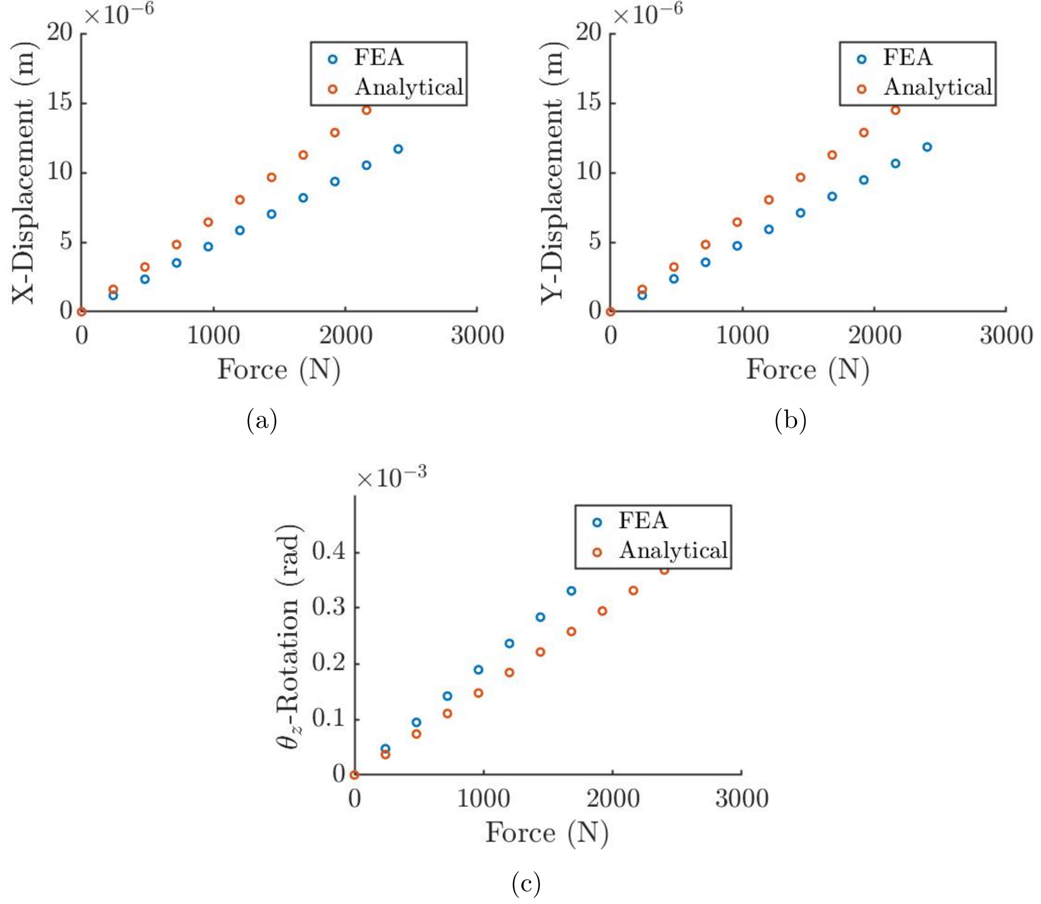

Figure 2.7: The primary in-plane displacements of the proposed SMBR under various values of loads: (a) the translational displacement along x-axis, (b) the translational displacement along y-axis, and (c) the θ_z-rotation about z-axis.

displacements of the proposed SMBR, which are expressed earlier in Equation (2.22), can be expressed as

$$x_{\text{out}} = \eta_x \left(q_{p_{5,a}} + q_{p_{11,a}} + \Delta x \right) \tag{2.23}$$

$$y_{\text{out}} = \eta_y \left(q_{p_{2,a}} + q_{p_{8,a}} + \Delta y \right) \tag{2.24}$$

$$\theta_{z\text{out}} = \frac{\eta_\theta}{a} \sum_{m=i} q_{p_{i,a}} \tag{2.25}$$

where $\eta_x = \eta_y = 0.73$ and $\eta_\theta = 1.28$. Figure 2.9 illustrates the primary in-plane output translational displacements along x- and y-axes, and the primary in-plane

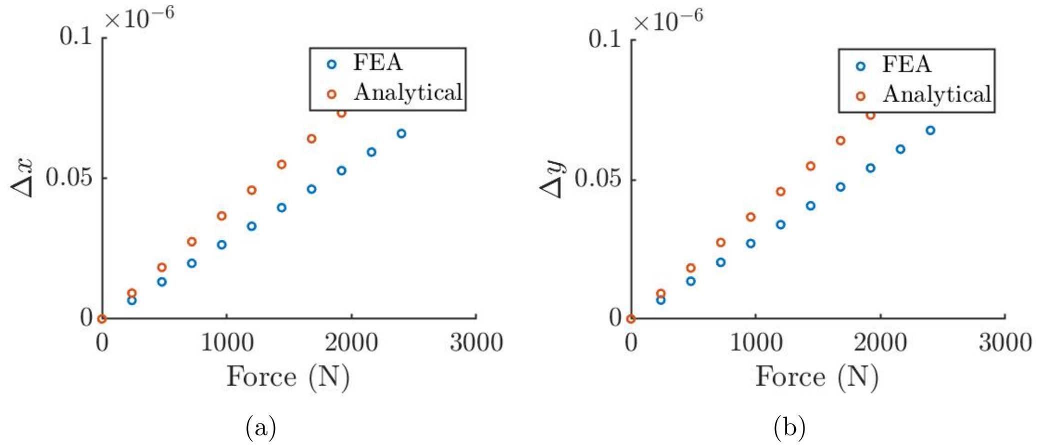

Figure 2.8: The parasitic in-plane coupling displacements of the proposed SMBR during the primary motions: (a) along x-axis and (b) along y-axis

output θ_z-rotation about z-axis, of the proposed SMBR under various values of loads taking into consideration the compensation factors.

Based on Figure 2.10, the parasitic in-plane coupling displacements during the primary in-plane translational displacements along x- and y-axes, are less than 0.572% of the primary in-plane displacements.

In the proposed SMBR, two piezoelectric actuators are responsible for the translational motion along x-axis, another two piezoelectric actuators are responsible for the translational motion along y-axis, and eight piezoelectric actuators are responsible for the rotational motion around z-axis. All these actuators can be activated independently to perform the desired motion(s) with the desired value(s) and direction(s), as demonstrated in Table 2.1 where F_{p_x} is the input force provided by each piezoelectric actuator in limbs 5 and 11, F_{p_y} is the input force provided by each piezoelectric actuator in limbs 2 and 8, and $F_{p\theta_z}$ is the input force provided by each piezoelectric actuator in limbs 1, 3, 4, 6, 7, 9, 10, and 12.

The workspace of the proposed SMBR is determined by the maximum allowable

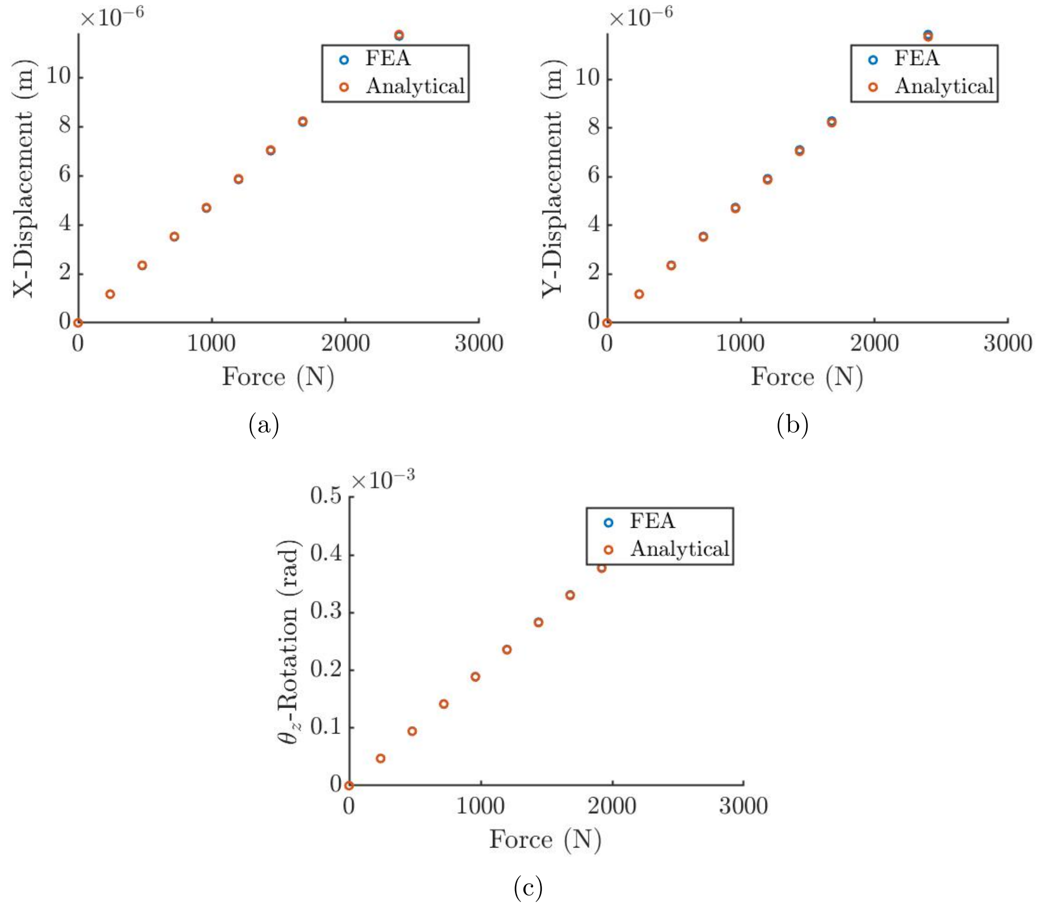

Figure 2.9: The primary in-plane displacements of the proposed SMBR under various values of loads taking into consideration the compensation factors: (a) the translational displacement along x-axis, (b) the translational displacement along y-axis, and (c) the θ_z-rotation about z-axis.

Table 2.1: Various operating case scenarios of the proposed SMBR.

Desired motion(s)			**Required input force(s)**		
δx [μm]	δy [μm]	$\delta\theta_z$ [mrad]	F_{p_x} [N]	F_{p_y} [N]	$F_{p_{\theta_z}}$ [N]
2.6	0	0	534.21	0	0
0	10.2	0	0	2095.74	0
0	0	0.1	0	0	509.21
5.5	3.2	0.25	1130.06	657.49	1273.03
-1.6	8.1	-0.3	328.74	1664.26	1527.64

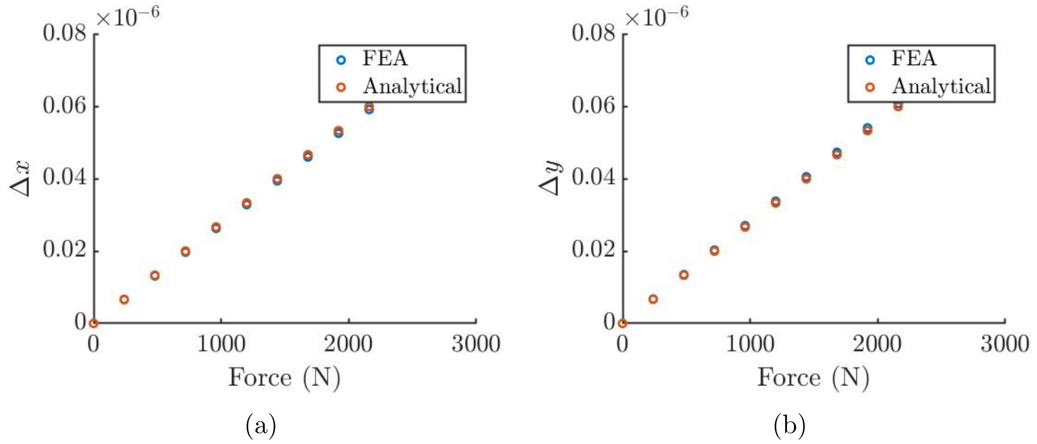

Figure 2.10: The parasitic in-plane coupling displacements of the proposed SMBR, taking into consideration the compensation factors, during the primary motions: (a) along x-axis and (b) along y-axis

stress, and the maximum stroke of the piezoelectric actuators which is given by

$$F_{p_i,\max} = k_{p_i}\left(1 - \frac{k_{p_i}}{k_{p_i} + K_s}\right) q_{p_i,n,\max} \tag{2.26}$$

where $q_{p_i,n,\max}$ is the maximum nominal displacement of the ith piezoelectric actuator.

Substituting Equation (2.26) into Equations (2.17)-(2.25) leads to the maximum workspace of the proposed SMBR as long as the maximum stress in the structure remains within the allowable stress, σ_a, of the material. In order to guarantee having the maximum stress in the structure within the allowable stress, stress analysis is conducted for the proposed SMBR.

The proposed SMBR involves numerous geometry features, however, the maximum stress mainly occurs at the thinnest features, namely, the root of the leaf hinges and the thinnest part of the right circular flexure hinges. Hence, the calculation of stresses is accomplished in such sections.

Since the axial tensile and compression deformations of a flexure hinge are far less than the bending deformation of the flexure hinge, only the bending deformation

due to the in-plane rotation of the flexure hinge is taken into account in the stress analysis. Thus, the following rule must be satisfied in the proposed SMBR:

$$\sigma_r^{\max} \leq \sigma_a = \sigma_y / n_a \tag{2.27}$$

where $\sigma_r^{\max}$ is the maximum stress due to rotations of the flexure hinge, σ_y being the yield stress of the material, and n_a being the assigned factor of safety of the proposed SMBR, $n_a > 1$. The maximum angular displacement of the flexure hinge, $\theta_{\max}$, around its rotational axis due to the bending moment occurred when the maximum stress due to rotations of the flexure hinge, $\sigma_r^{\max}$, reaches the yield stress, σ_y. According to [73], the relation between the maximum stress due to rotations of the flexure hinge, $\sigma_r^{\max}$, and the maximum angular displacement of the flexure hinge due to the bending moment, $\theta_{\max}$, can be expressed as

$$\sigma_r^{\max} = \frac{E_s\,(1+\beta)^{9/20}}{\beta^2 f(\beta)} \theta_{\max} \tag{2.28}$$

where $\beta = t_o/2r$ is a dimensionless geometry factor with a valid range of $0 < \beta < 2.3$, and $f(\beta)$ is a dimensionless compliance factor defined as

$$f(\beta) = \frac{1}{2\beta+\beta^2}\left[\frac{3+4\beta+2\beta^2}{(1+\beta)\,(2\beta+\beta^2)} + \frac{6(1+\beta)}{(2\beta+\beta^2)^{3/2}} \tan^{-1}\sqrt{\frac{2+\beta}{\beta}}\right] \tag{2.29}$$

Assuming that the maximum input forces are provided by the piezoelectric actuators in limbs 2 and 8. Hence, the maximum in-plane output translational motion of the proposed SMBR along y-axis, y_{out}, is achieved due to the maximum angular displacement of the hinges, $\theta_{\max}$. Based on the geometry of the limb, the maximum angular displacement may occur in the right circular flexure hinges or in the leaf

springs. The maximum rotational angles of the hinges can be derived as follows

$$\begin{aligned} \theta_{H_4}^{\max} &= \frac{y_{\text{out}}/2}{l_7}, & \theta_{H_9}^{\max} &= \frac{y_{\text{out}}/2}{\sqrt{l_{12}^2 + l_{13}^2}} \\ \theta_{H_{13}}^{\max} &= \frac{y_{\text{out}}}{l_{15}}, & \theta_{H_{15}}^{\max} &= \frac{x_{\text{out}}/2}{l_{16}} \end{aligned} \tag{2.30}$$

Substituting Equation (2.30) into Equation (2.28) yields expressions for the maximum stresses due to rotational motions of the flexure hinges, $\sigma_r^{\max}$. Then, by using Equation (2.27), the following expressions can be obtained

$$\begin{aligned} \sqrt{l_{12}^2 + l_{13}^2} &\geq \frac{y_{\text{out}} E_s (1+\beta)^{9/20} n_a}{2\sigma_y \beta^2 f(\beta)} \\ l_{15} &\geq \frac{y_{\text{out}} E_s (1+\beta)^{9/20} n_a}{\sigma_y \beta^2 f(\beta)} \\ l_{16} &\geq \frac{x_{\text{out}} E_s (1+\beta)^{9/20} n_a}{\sigma_y \beta^2 f(\beta)} \\ l_7 &\geq \frac{y_{\text{out}} E_s (1+\beta)^{9/20} n_a}{2\sigma_y \beta^2 f(\beta)} \end{aligned} \tag{2.31}$$

These expressions are used as guidelines for the dimensional optimisation of the proposed stage to avoid the risk of inelastic deformations in the proposed SMBR during performing the desired motions. The equivalent von Mises stress is calculated in *ANSYS* at various load values for the translational motions along x- and y-axes, and the θ_z-rotational motion around z-axis. Figure 2.11 demonstrates the maximum equivalent von Mises stress at the critical locations at different load values. The critical locations exist at the hinges in limbs 2 and 8 for the output translational motion of the proposed SMBR along y-axis, at the hinges in limbs 5 and 11 for the output translational motion of the proposed SMBR along x-axis, and at the hinges in limbs 1, 3, 4, 6, 7, 9, 10, and 12 for the θ_z-rotational motion of the proposed SMBR around z-axis, as shown in Figure 2.12.

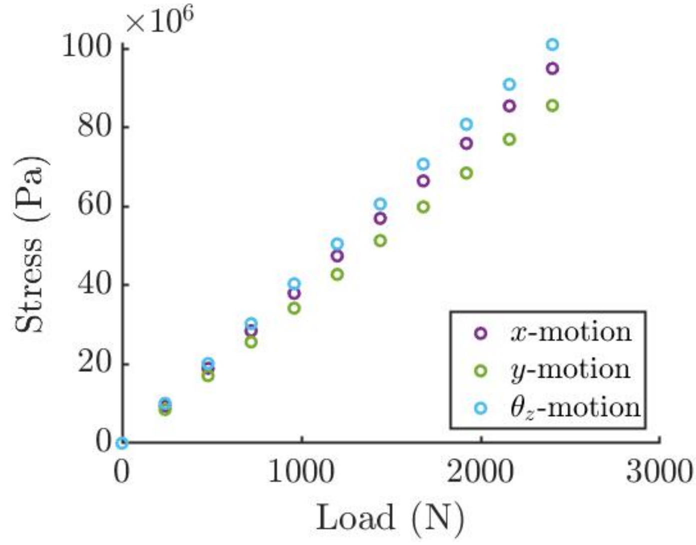

Figure 2.11: The maximum equivalent von-Mises stress at the critical locations at different load values for the translational motions along x- and y-axes, and the θ_z-rotational motion around z-axis.

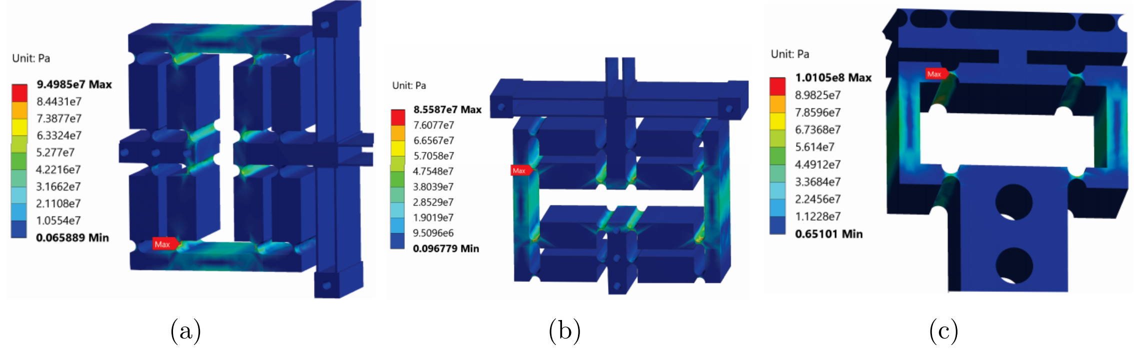

(a) (b) (c)

Figure 2.12: The critical locations at which the maximum stress occur during (a) translational motion along x-axis, (b) translational motion along y-axis, and (c) θ_z-rotational motion around z-axis.

Based on this analysis, the workspace of the proposed SMBR is 11.7462 μm $\times$ 11.7462 μm $\times$ 0.4713 mrad for the translational motions along x- and y-axes, and the θ_z-rotational motion around z-axis, respectively. Besides, based on on Figure 2.11, and taking into consideration the yield stress, σ_y, of the *7075 Aluminum* and *Fused Silica*, the minimum achievable factor of safety of the proposed SMBR is 4.98 for the

mentioned workspace, as demonstrated in Figure 2.13.

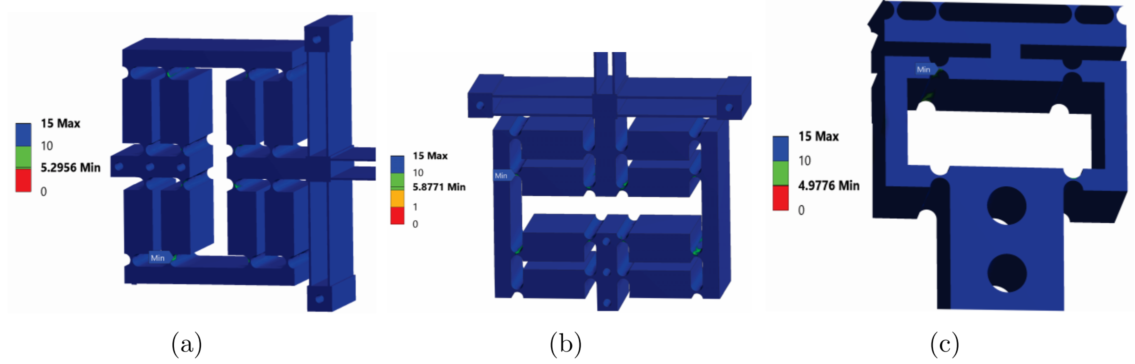

(a) (b) (c)

Figure 2.13: The minimum value of the factor of safety in the proposed SMBR during the (a) translational motion along x-axis, (b) translational motion along y-axis, and (c) θ_z-rotational motion around z-axis.

2.5 Modal Analysis

The Lagrangian approach, which depends on energy balance, is employed to derive the dynamics equation of the in-plane undamped free vibration of the proposed smart materials-based reticle (including the piezoelectric actuators) in which the generalized coordinates are chosen to be as follows

$$\mathbf{u} = [q_1 \ q_2 \ q_3 \ q_4 \ q_5 \ q_6 \ q_7 \ q_8 \ q_9 \ q_{10} \ q_{11} \ q_{12} \ x_{\text{out}} \ y_{\text{out}} \ \theta_{z\text{out}}]^T, \tag{2.32}$$

where q_i represents the input displacement of the ith piezoelectric actuator, x_{out}, y_{out}, and $\theta_{z\text{out}}$ are the output displacements of the proposed SMBR.

The kinetic energy and potential energy of limb 1 are expressed as

$$
\begin{aligned}
T_1 = & \frac{1}{2}m_p\dot{q}_1^2 + 2J_{m_1}\left(\dot{\theta}_{c_1}^2 + \dot{\beta}_{c_1}^2\right) + m_2\left(\dot{q}_1/2\right)^2 + J_{m_2}\dot{\beta}_{c_1}^2 \\
& + \frac{1}{2}m_3\left(\dot{D}_1^2 + \dot{y}_{\text{out}}^2\right) + J_{m_9}\dot{\theta}_{L_9}^2 + m_9\dot{y}_{\text{out}}^2 + \frac{1}{2}J_c\dot{\theta}_{c_1}^2 \\
& + \left(J_{m_3} + J_{m_9}\right)\dot{\theta}_{\text{zout}}^2 + \left(m_4 + m_9\right)\left(\dot{d}_x^2 + \dot{d}_y^2\right)
\end{aligned} \tag{2.33}
$$

$$
V_1 = 2K_{rc_1}\left(\theta_{c_1}^2 + y_{\text{out}}^2\right) + \frac{1}{2}\left(4K_{rc_1}C^2 + k_p\right)q_1^2 + K_{rc_1}\theta_{\text{zout}}^2 \tag{2.34}
$$

where m_i and J_{m_i} are the mass and moment of inertia of link i, respectively. m_p is the mass of the piezoelectric actuator. θ_{c_1} and β_{c_1} are the rotational angles of the circular flexure hinges in limb 1 during the translational motions along x- and y-axes, respectively. θ_{L_9} is the rotational angle of link 9 during the translational motion along y-axis. d_x and d_y are the displacements of the links L_4, L_5, L_9, and L_{10} along x- and y-axes, respectively, during the θ_z-rotational motion around z-axis. D_1 is the displacement of point D_1. K_{rc_1} is the rotational stiffness of the circular flexure hinges in limb 1.

The kinetic energy and potential energy of limb 2 are expressed as

$$
\begin{aligned}
T_2 = & \frac{1}{4}\left(m_{14} + m_{15}\right)\dot{D}_2^2 + \left(m_{11} + \frac{1}{8}m_{12}\right)\left(\dot{q}_2^2 + \dot{D}_2^2\right) \\
& + \frac{8}{2}\frac{1}{12}m_{12}\left(l_{12}^2 + l_{13}^2\right)\dot{\theta}_{L_{12}}^2 + \frac{1}{8}m_2\left(\dot{q}_2^2 + 3\dot{D}_2{}^2\right) \\
& + \frac{1}{2}m_p\dot{q}_2^2
\end{aligned} \tag{2.35}
$$

$$
V_2 = \frac{8}{2}K_{rc_2}\theta_{c_2}{}^2 + K_{rl}\theta_l{}^2 + \frac{1}{2}k_pq_2^2 \tag{2.36}
$$

where D_2 is the displacement of point D_2. $\theta_{L_{12}}$, θ_{c_2}, and θ_l are the rotational angles of link 12, circular flexure hinges, and of the leaf hinges, respectively, in limb 2. K_{rc_2} and

K_{rl} are the stiffness of the circular flexure hinges, and of the leaf hinges, respectively, in limb 2.

The kinetic energy of the reticle and mobile platform is expressed as

$$T_{\mathrm{R-mp}} = \frac{1}{2}\left(m_{\mathrm{R}} + m_{\mathrm{mp}}\right)\left(\dot{x}_{\mathrm{out}}^2 + \dot{y}_{\mathrm{out}}^2\right) + \frac{1}{2}J_{\mathrm{R-mp}}\dot{\theta}_{\mathrm{zout}}^2 \tag{2.37}$$

where m_{R} and m_{mp} are the masses of the reticle and mobile platform, respectively. $J_{\mathrm{R-mp}}$ the moment of inertia of the reticle and mobile platform.

Then, the total kinetic energy, T_{tot}, and total potential energy, V_{tot}, of the entire proposed smart materials-based reticle (including the limbs, piezoelectric actuators, mobile platform, and the reticle) can be expressed as

$$T_{\mathrm{tot}} = 8T_1 + 4T_2 + T_{\mathrm{R-mp}} \tag{2.38}$$

$$V_{\mathrm{tot}} = 8V_1 + 4V_2 \tag{2.39}$$

Substituting Equations (2.38) and (2.39) into Lagrange's equation, namely,

$$\frac{d}{dt}\frac{\partial T_{\mathrm{tot}}}{\partial \dot{\mathbf{u}}_i} - \frac{\partial T_{\mathrm{tot}}}{\partial \mathbf{u}_i} + \frac{\partial V_{\mathrm{tot}}}{\partial \mathbf{u}_i} = 0 \tag{2.40}$$

leads to the dynamic equation that describes the free motion of the proposed SMBR, namely, $\mathbf{M}\ddot{\mathbf{u}}+\mathbf{K}\mathbf{u} = 0$, where $\mathbf{M}$ and $\mathbf{K}$ are the equivalent mass and stiffness matrices, respectively, of the proposed smart materials-based reticle.

Using the obtained dynamic equation, the modal equation is derived as

$$\left(\mathbf{K} - \omega_j^2\mathbf{M}\right)\mathbf{\Phi}_j = \mathbf{0} \tag{2.41}$$

where $\mathbf{\Phi}_j$, (for $j = 1, 2, ..., 15$), are the eigenvectors which represent the modal shapes,

and ω_j^2 are eigenvalues which describe the corresponding natural cyclic frequency for each modal shape. This can be obtained by solving the characteristic equation $\left|\mathbf{K} - \omega_j^2\mathbf{M}\right| = 0$. Then, the natural frequency can be computed as $f_j = (1/2\pi)\omega_j$. The lowest one can be taken as the resonant frequency of the proposed smart materials-based reticle.

A finite element model has been built using *ANSYS*, where fixed-support constraints were applied at all fixing holes. In addition, fine and smooth mesh is applied at all bodies, and the quality of the mesh has been studied and verified through various quality measures, as discussed below

1. **Orthogonal quality:** (where the worst value is 0 and the best value is 1).

   95.37% of the mesh has value of 0.995

   3.55% of the mesh has value of 0.865

   The rest has a value range between $0.595 - 0.775$

2. **Element quality:** (where the worst value is 0 and the best value is 1).

   86.5% of the mesh has value of 0.951

   7.77% of the mesh has value of 0.852

   1.73% of the mesh has value of 0.753

   0.995% of the mesh has value of 0.654

   The rest has a value range between $0.16 - 0.556$

3. **Skewness:** (where the worst value is 1 and the best value is 0).

   65.11% of the mesh has value of 0.045

   15.8% of the mesh has value of 0.135

   8.83% of the mesh has value of 0.225

   6.14% of the mesh has value of 0.315

   The rest has a value range between $0.405 - 0.585$

4. **Aspect ratio:** (where the worst value is ∞ and the best value is 1).

   99.5% of the mesh has value of 3.55

   The rest has a value range between 8.62–18.8

5. **Jacobian Ratio (MAPDL):** (where the worst value is ∞ and the best value is 1).

   99.28% of the mesh has value of 2.39

   The rest of the mesh has value of 5.18

6. **Jacobian Ratio (Gauss Points):** (where the worst value is -1 and the best value is 1).

   79.7% of the mesh has value of 0.9

   15.2% of the mesh has value of 0.7

   4.29% of the mesh has value of 0.5

   The rest of the mesh has value of 0.3

The derived modal analysis is verified using FEA. Figure 2.14 illustrates the first six mode shapes extracted using *ANSYS*, the first two mode shapes correspond to the translational motions of the proposed SMBR along x- and y-axes, and the third mode shape corresponds to the θ_z-rotational motion around z-axis.

Considering the FEA results as the benchmark, Table 2.2 demonstrates the deviation in the natural frequencies values between FEA and Lagrange's approach. The source of the offset is mainly due to compliance of the links, which are assumed as rigid bodies, between the flexure hinges through Lagrange's approach.

Based on Table 2.2 and Figure 2.14, the first two mode shapes have (almost) equal natural frequencies, since the design is symmetric along the x- and y-axes. In practical, it is impossible to obtain a pure single mode shape. There will be always noise from other mode shapes, but there is always a dominant one. To provide

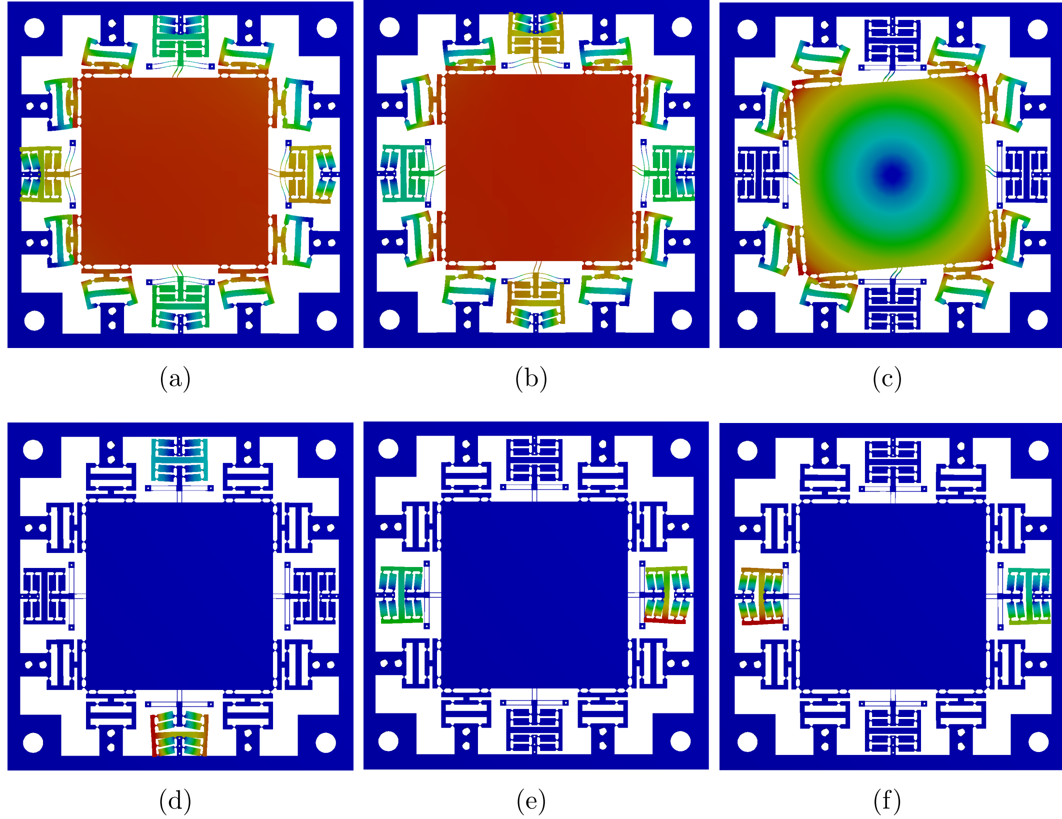

Figure 2.14: The first six mode shapes of the proposed SMBR extracted by *ANSYS*: (a) Mode 1 at 859.14 Hz, (b) Mode 2 at 860.14 Hz, (c) Mode 3 at 1112.9 Hz, (d) Mode 4 at 1328.6 Hz, (e) Mode 5 at 1346.9 Hz, and (f) Mode 6 at 1370.4 Hz.

Table 2.2: In-plane resonant frequencies of the stage (Hz).

	y-motion	**x-motion**	θ_z**-motion**
Lagrange	741.29	741.29	884.06
FEA	860.14	859.14	1112.9
Deviation (%)	13.82	13.72	20.56

an insight about the percentage of contribution of certain mode shape in the other mode shapes, and in order to determine which mode shapes will be dominant when we apply the load in certain direction, the *mass participation factor*, Γ, and *modal effective mass*, m_{eff}, are used.

The mass participation factor, Γ, represents the portion of mass that will con-

tribute in the response of certain mode shape when the proposed SMBR is excited in certain direction. Hence it gives an insight about how much mass will contribute in the response and how much mass will remain stationary.

Each mode shape has its own mass participation factor, Γ_i, and its own modal effective mass, $m_{\mathrm{eff_i}} = \Gamma_i^2$, where i represents the number of the mode shape. The summation of mass participation factors for all mode shapes in any direction will equal to the total mass of the structure that will contribute in the response in that direction, m_x, m_y, m_z, I_{θ_x}, I_{θ_y}, and I_{θ_z}.

When the load is applied in certain direction, the contribution of mode shape i in the response of the proposed SMBR is determined by ratio of the modal effective mass of that mode, $m_{\mathrm{eff_i}}$, to the total mass in that direction, m_j. Hence, the participation percentage of the ith mode shape in the jth response can be expressed as

$$\Omega_{i,j} = \frac{m_{\mathrm{eff_i}}}{m_j} \times 100\% \tag{2.42}$$

where j represent the direction of the response, namely, x, y, z, θ_x, θ_y, and θ_z. In addition, the mass participation percentage in the j response, Ψ_j, can be expressed as

$$\Psi_j = \frac{m_j}{m_{\mathrm{sys}}} \times 100\% \quad \text{and} \quad \Psi_{\mathrm{j}} = \frac{\mathrm{I_j}}{\mathrm{I_{sys}}} \times 100\% \tag{2.43}$$

where m_{sys} and I_{sys} are the total mass of the proposed SMBR (including the limbs, piezoelectric actuators, and the reticle) and its moment of inertia, respectively.

Based on Tables 2.3 and 2.4, if the exciting load is applied by piezoelectric actuators in limbs 5 and 11 to excite translational motion along x-axis, the first mode shape is dominant in the response by 76.33% and the second mode shape contributes

in that response by 23.54% which represents the parasitic in-plane coupling displacement along y-axis during the translational motion along x-axis. In addition, 50.33% of the structure will contribute in that response.

Table 2.3: Modal effective mass and inertia of the proposed SMBR

		Modal effective mass m_{eff} (kg)			Modal effective inertia I_{eff} (kg.m^2)		
Mode	f (Hz)	T_x	T_y	T_z	R_x	R_y	R_z
1	859.14	1.938	0.598	1.1e-5	9.3e-5	3.1e-4	7.1e-7
2	860.14	0.598	1.941	9.8e-7	3.1e-4	8.1e-5	5.3e-9
3	1112.9	6.7e-5	1.4e-5	2.6e-3	1.3e-11	5.5e-8	1.7e-2
4	1328.6	9.7e-7	5.9e-5	6.5e-8	1.7e-8	3.3e-7	3.8e-7
5	1346.9	7.1e-5	2.1e-5	2.3e-6	1.1e-9	6e-9	1.4e-6
6	1370.4	3.2e-3	5.8e-7	9.7e-9	1e-8	8.9e-7	2.9e-6
		m_x	m_y	m_z	I_{θ_x}	I_{θ_y}	I_{θ_z}
Total (kg, kg.m^2)		2.539	2.539	0.003	4e-4	4e-4	1.7e-2
Ψ_j (%)		50.33	50.34	0.05	0.804	0.799	17.3

Table 2.4: Mass participation percentage of the proposed SMBR

		Participation percentage Ω (%)					
Mode	f (Hz)	T_x	T_y	T_z	R_x	R_y	R_z
1	859.14	76.33	23.57	0.4	23.05	77.47	4.2e-3
2	860.14	23.54	76.43	0.04	76.95	22.49	3.2e-5
3	1112.9	2.6e-3	5.7e-4	99.47	3.1e-6	0.01	99.97
4	1328.6	3.8e-5	2.3e-3	2.5e-3	4.1e-3	8.2e-4	2.3e-3
5	1346.9	2.8e-3	8.1e-4	0.09	2.6e-4	1.5e-3	0.01
6	1370.4	0.12	2.3e-5	3.7e-4	2.6e-3	0.02	0.02

Similarly, if the exciting load is applied by piezoelectric actuators in limbs 2 and 8 to excite translational motion along y-axis, the second mode shape is dominant in the response by 76.43% and the first mode shape contributes in that response by 23.54% which represents the parasitic in-plane coupling displacement along x-axis during the

translational motion along y-axis. In addition, 50.34% of the structure will contribute in that response.

If the exciting load is applied by piezoelectric actuators in limbs 1, 3, 4, 6, 7, 9, 10, and 12 to excite θ_z-rotational motion around z-axis, the third mode shape is dominant in the response by 99.47%. The first and the second mode shapes have almost no contribution in that response, and that means the parasitic in-plane coupling displacements along x- and y-axes are negligible during the θ_z-rotational motion. In addition, 17.3% of the structure will contribute in that response.

From the first rows in Tables 2.3 and 2.4, we conclude that the first mode shape has mainly translational motion along x-axis with a percent of 76.33%, and it has only a 23.57% of translational motion along y-axis. Besides, the parasitic out-of-plane motion along z-axis has almost no contribution in this mode shape. The θ_x- and θ_y-rotational motions around x- and y-axes, respectively, have big contributions in this mode shape, 23.05% and 77.47%, respectively. However, since only 0.804% and 0.799% of the entire proposed SMBR exhibit these rotations, this contribution has no effect on the primary translational motion along x-axis.

Similarly, from the second row in Tables 2.3 and 2.4, we conclude that the second mode shape has mainly translational motion along y-axis with a percent of 76.43%, and it has only a 23.54% of translational motion along x-axis. Besides, the parasitic out-of-plane motion along z-axis has almost no contribution in this mode shape. The θ_x- and θ_y-rotational motions around x- and y-axes, respectively, have big contributions in this mode shape, 76.95% and 22.49%, respectively. However, since only 0.804% and 0.799% of the entire proposed SMBR exhibit these rotations, this contribution has no effect on the primary translational motion along x-axis.

Finally, from the third row in Tables 2.3 and 2.4, we conclude that the third mode shape has mainly θ_z-rotational motion with a percent of 99.47%, and the other types

of motions have negligible effects.

2.6 Dimensional Optimisation of the Proposed Smart Materials-Based Reticle

Based on the previous analysis, it is obvious that the dimensions of the proposed SMBR must be chosen properly since it has direct influence on the static and dynamic characteristics of the proposed SMBR. In other words, the determination of the dimensions is an essential step at this stage.

Many factors must be taken into consideration; for example, (i) the desired workspace, (ii) the resulted resonant frequencies, (iii) the piezoelectric actuator specifications, (iv) material properties, (v) machinability, (vi) the design's factor of safety, and so on.

In this study, the dimensions are optimized to minimize the settling time in order to guarantee a rapid correction in a time duration less than the settling time of the short-stroke. The displacement responses of the proposed SMBR must exhibit oscillatory under-damped behaviour, in which the amplitude of the responses decay each cycle by a specific logarithmic decrements, δ, that depends on the damping ratio, ζ, of the proposed SMBR as follows:

$$\delta = \frac{2\pi\zeta}{\sqrt{1-\zeta^2}} \tag{2.44}$$

Besides, the amplitude of the displacement response after n cycles, A_n, can be expressed as

$$A_n = A_0 e^{-n\delta} \tag{2.45}$$

where A_0 is the maximum amplitude in the displacement response, A_n is the desired

amplitude. Equation (2.45) can be expressed as

$$ln\left(\frac{A_0}{A_n}\right) = n\delta \tag{2.46}$$

Substituting Equation (2.44) into Equation (2.46), and taking into consideration that $\omega_d = \omega_n\sqrt{(1-\zeta^2)}$, the settling time for the proposed SMBR can be expressed as

$$t_s = \frac{ln(A_0/A_n)}{2\pi\omega_{n_s}\zeta} \tag{2.47}$$

where ω_{ns} is the undamped resonant frequency of the proposed SMBR, in which the subscript s stands for the direction of motion, namely, x, y, or θ_z.

Based on Equation (2.47), for a given desired amplitude in certain direction, minimizing the settling time can be achieved by maximizing the resonant frequency of the proposed SMBR in the desired direction. Hence, in order to obtain the optimal dimensions which assure acquiring the minimum settling time, the main objective of the optimization algorithm is set to maximize the in-plane stiffness of the proposed SMBR along x- and y-axes, and around z-axis, namely, K_x, K_y, and K_{θ_z}.

As illustrated in Figure 2.15, a comprehensive parametric study is performed in order to determine the parameters that have the largest effect on the stiffness of the proposed SMBR. This study shows that (t_4, l_6, l_{20}, $t_{0,1}$, r_1, S_1, S_2, and S_3) are the parameters that have the most influence on the stiffness of the proposed SMBR. These parameters are optimised to maximize the stiffness of the proposed SMBR. The optimisation problem can be summarized as follows:

1. **Objective:** to maximize the in-plane stiffness along x- and y-axes, and around z-axis, namely, K_x, K_y, and K_{θ_z}.

2. **Parameters to be optimized:** t_4, l_6, l_{20}, $t_{0,1}$, r_1, S_1, S_2, and S_3.

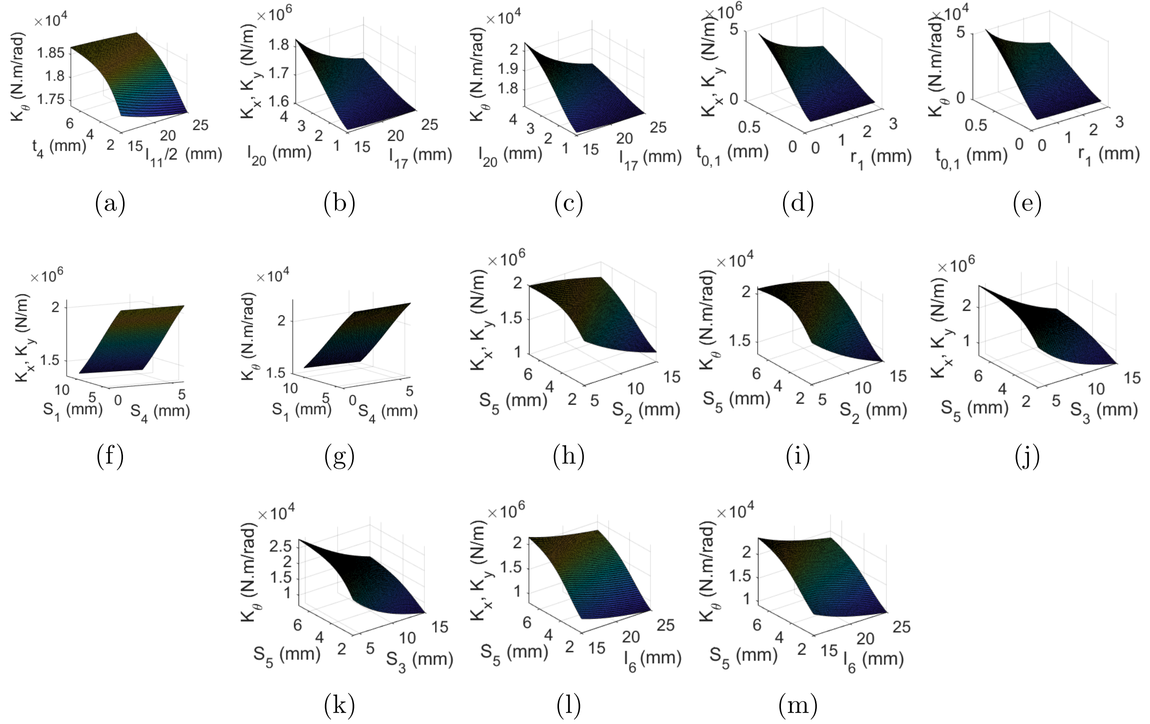

Figure 2.15: Parametric study for the effecting parameters: (a) the influence of t_4 and l_{11} on K_x and K_y, (b) the influence of t_4 and l_{11} on K_{θ_z}, (c) the influence of l_{17} and l_{20} on K_x and K_y, (d) the influence of l_{17} and l_{20} on K_{θ_z}, (e) the influence of r_1 and $t_{0,1}$ on K_x and K_y, (f) the influence of r_1 and $t_{0,1}$ on K_{θ_z}, (g) the influence of S_1 and S_4 on K_x and K_y, (h) the influence of S_1 and S_4 on K_{θ_z}, (i) the influence of S_2 and S_5 on K_x and K_y, (j) the influence of S_2 and S_5 on K_{θ_z}, (k) the influence of S_3 and S_5 on K_x and K_y, (l) the influence of S_3 and S_5 on K_{θ_z}, (m) the influence of l_6 and S_5 on K_x and K_y, and (n) the influence of l_6 and S_5 on K_{θ_z}.

3. **Constraints:**

   (a) Parameters of flexure hinges: $0 \leq t_0/2r \leq 2.3$;

   (b) Constraint in Equation (2.31);

   (c) Ranges of parameters (mm): $2 \leq t_4 \leq 8$, $1 \leq l_6 \leq 5$, $0.19 \leq l_{20} \leq 0.8$, $0.34 \leq t_{0,1} \leq 3$, $4 \leq r_1 \leq 10$, $8 \leq S_1 \leq 14$, $5 \leq S_2 \leq 12$, and $11 \leq S_3 \leq 23$.

   (d) Additional rules must be satisfied: $S_2 + 2r_2 + S_3 - S_5 > 18$ mm, $l_{20} + 4r_1 + l_{12} > 18$ mm, $l_{11}/2 - 2l_{13} - t_1 > 5$ mm;

The constraints are determined by considering several factors, as follows:

1. The value of $t_0/2r$ is restrained to guarantee the accuracy of Equation (2.28) in estimating the maximum angular displacement of the flexure hinges.

2. Equation (2.31) is taken into consideration to avoid plastic deformation of the structure.

3. The thinnest portion of the flexure hinges, $t_{0,1}$, must be not less than 0.34 mm to guarantee the machinability of the flexural mechanism using the Wire Electrical Discharge Machining (WEDM) technology, since this technology can achieve a tolerance of 0.01 mm when the thickness is greater than 0.34 mm.

4. In order to attain a compact structure, the upper bounds of the dimensions are kept within reasonable values.

5. The additional rules that must be satisfied are chosen to ensure having enough space for the piezoelectric actuators.

The optimisation is performed using Grey Wolf Optimizer (GWO) through *MATLAB*, the searching for the optimum values terminates at the 4698th iteration, the stiffness values remained almost constant after that. The convergent process is illustrated in Figure 2.16.

In addition, the algorithm is carried out 10 times to ensure that the obtained values of the parameters were the optimum ones. Figure 2.17 demonstrates the maximum stiffness histories over all iterations.

The optimum results are (in mm): t_4 =7.83247, l_{20} =1.1598, $t_{0,1}$ =0.79301, r_1 =2.97102, S_1 =4.23626, S_2 =11.1703, S_3 =5.59173, and l_6 =11.0167. Considering the accuracy of the WEDM, we modify the dimensions as follows: t_4 =7.83,

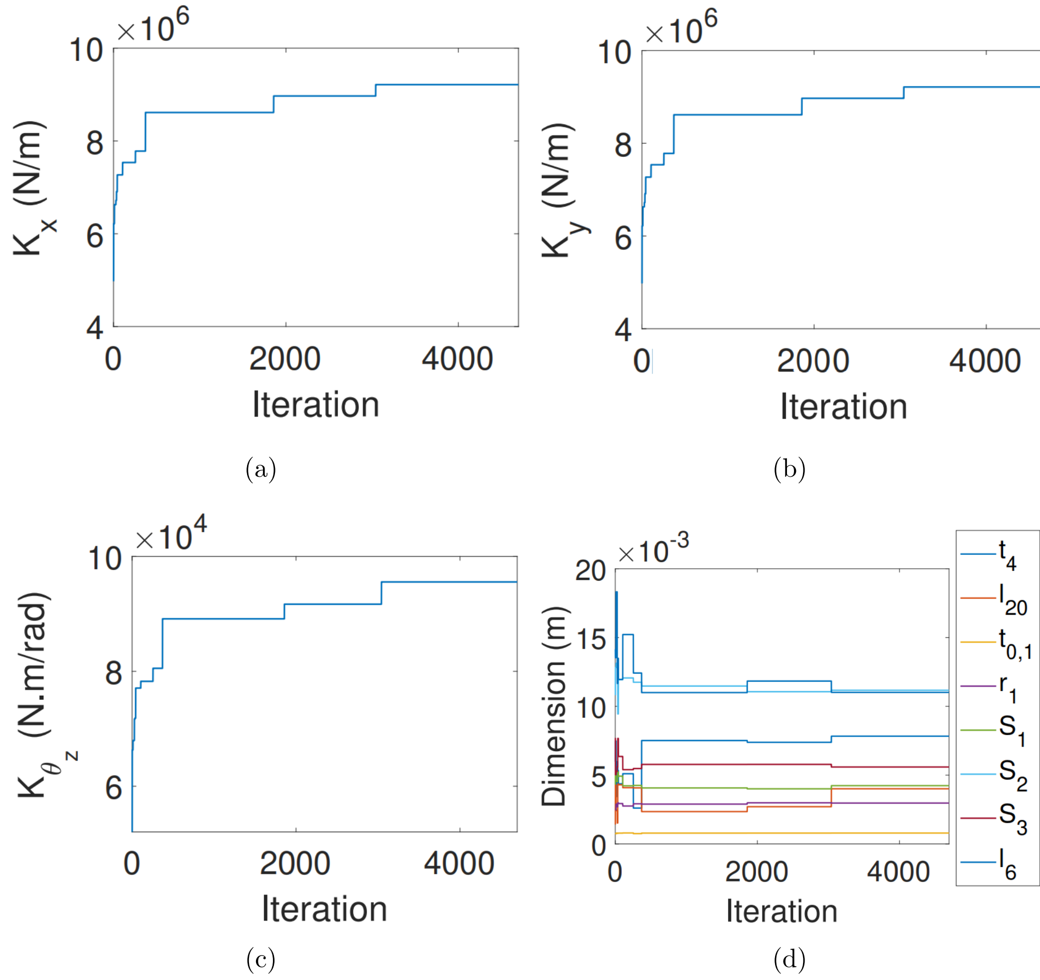

Figure 2.16: The convergent process of the GWO: (a) K_x convergence, (b) K_y convergence, (c) K_{θ_z} convergence, and (d) optimising parameters convergence.

l_{20} =1.16, $t_{0,1}$ =0.79, r_1 =2.97, S_1 =4.24, S_2 =11.17, S_3 =5.59, and l_6 =11.01. All dimensions of the proposed SMBR are shown in Table 2.5 and its material properties are shown in Table 2.6.

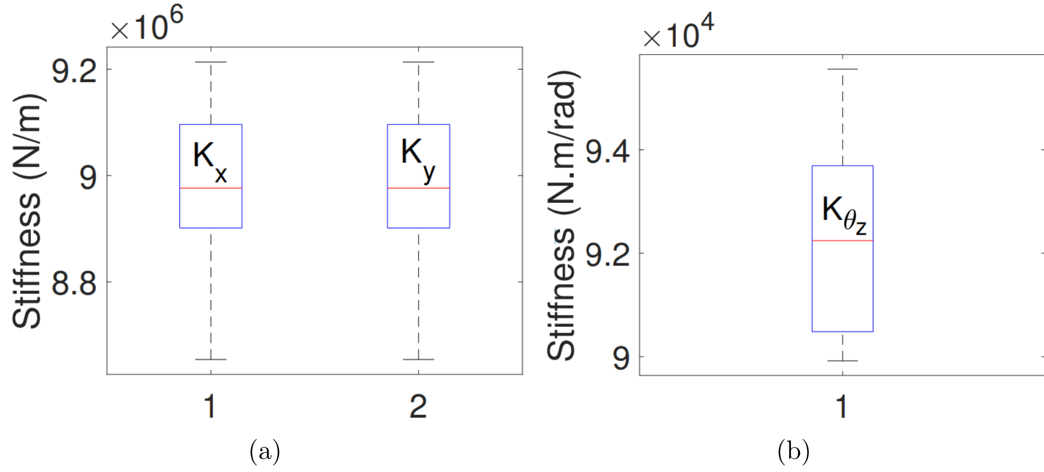

Figure 2.17: Maximum stiffness histories over all repetitions: (a) the K_x and K_y histories, and (b) K_{θ_z} history.

Table 2.5: The architecture parameters of the proposed SMBR (mm)

Parameter	Value	Parameter	Value	Parameter	Value	Parameter	Value
l_1	49	l_{11}	41	w	25	t_{mp}	15
l_2	64	l_{12}	15	a	66.65	t_{bf}	15
l_3	4.5	l_{13}	7	r_1	2.97	S_1	4.24
l_4	27	l_{14}	3	r_2	1.5	S_2	11.17
l_5	12	l_{15}	24.5	$t_{0,1}$	0.79	S_3	5.59
l_6	11.01	l_{16}	11	$t_{0,2}$	0.5		
l_7	9	l_{17}	19	t_1	2		
l_8	4.5	l_{18}	6	t_2	4		
l_9	6	l_{19}	4	t_3	4		
l_{10}	55	l_{20}	1.16	t_4	7.83		

2.7 Expressing the Output Displacements in Terms of Input Voltage

The proposed SMBR implements twelve piezoelectric actuators. These actuators provide the proposed flexure hinge-based mechanism with the required forces to move the reticle. The piezoelectric actuators are provided with the required input voltages to achieve the desired in-plane output motions. The required input voltage to the ith

Table 2.6: Material properties of the proposed SMBR

Material properties						
E_s	E_r	ν_s	ν_r	ρ_s	ρ_r	$\sigma_{y,Al}$
[GPa]	[GPa]	$[-]$	$[-]$	$[kg/m^3]$	$[kg/m^3]$	[MPa]
71.7	72.6	0.33	0.16	2810	2200	503

piezoelectric actuator is expressed as

$$V_{p_i} = \frac{q_{p_i,n}}{n_{p_i} \times d_{33p_i}} \tag{2.48}$$

where n_{p_i} is the number of layers of the ith piezoelectric actuator, and d_{33p_i} being the strain coefficient of the ith piezoelectric actuator.

Substituting Equations (2.17) and (2.18) into Equations (2.23), (2.24), and (2.25), and taking into consideration Equation (2.48), the following expressions can be obtained

$$V_{p_i} = \frac{k_{p_i} + K_x}{2\eta_x k_{p_i} n_{p_i} d_{33p_i}} x_{\text{out}} \tag{2.49}$$

$$V_{p_j} = \frac{k_{p_j} + K_y}{2\eta_y k_{p_j} n_{p_j} d_{33p_j}} y_{\text{out}} \tag{2.50}$$

$$V_{p_m} = \frac{a\left(k_{p_m} + K_{\theta_z}\right)}{8\eta_\theta k_{p_m} n_{p_m} d_{33p_m}} \theta_{zout} \tag{2.51}$$

where V_{p_i}, V_{p_j} and V_{p_m} are the input voltages to the ith, j^{th} and m^{th} piezoelectric actuators, respectively. These voltages are responsible for the translational motion along x-axis, translational motion along y-axis, and θ_z-rotational motion around z-axis, respectively. Equations (2.49), (2.50), and (2.51) express the required input voltages to drive the piezoelectric actuators in terms of the desired in-plane output motions of the proposed SMBR. Figure 2.18 demonstrates the required input voltages

to achieve various in-plane output displacement functions.

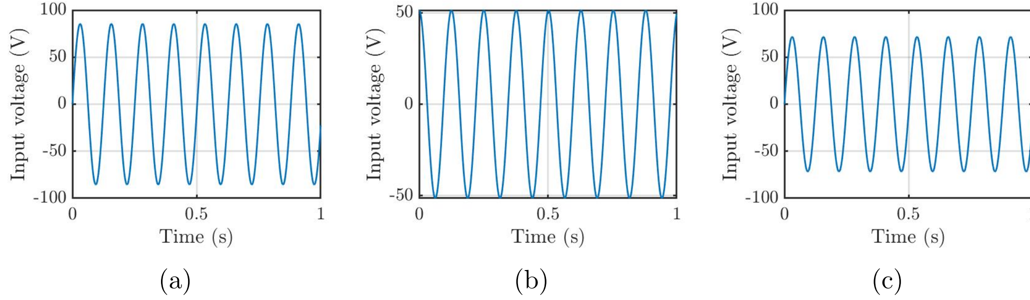

Figure 2.18: The required input voltage to be supplied to the piezoelectric actuators in order the proposed SMBR achieves a desired in-plane output displacement function: (a) $x_{\text{out}} = 5\sin(50t)$ μm, (b) $y_{\text{out}} = 3\cos(50\text{t})$ μm, and (c) $\theta_{\text{zout}} = 0.2\sin(50\text{t})$ mrad.

2.8 Conclusions of the Chapter

- A novel design of smart materials-based reticle is proposed. The proposed SMBR is able to reduce the relative in-plane micro-positioning error in the synchronization motion between the reticle and the wafer stages, by implementing piezoelectric actuators.

- This chapter showcases the design characteristics that can perform translational motions along x- and y-axes, and θ_z-rotational motion around z-axis at the same instant.

- Compliance analysis for the proposed SMBR has been done in order to determine its equivalent stiffness.

- Based on the derived static models, the proposed SMBR is able to perform an output motion of 16 μm along the x- and y-axes, and 0.3682 mrad around z-axis when a maximum force of 2400 N is provided by each piezoelectric actuator.

- In comparison with the static modeling conducted using *ANSYS*, the derived analytical model overestimates the translational output displacements of the proposed SMBR by 36.83%, and underestimates the rotational output displacements of the stage by 22.08%. Hence, compensation factors have been adopted in the analytical model in order to take into consideration this deviation.

- Taking into consideration the compensation factors, the proposed SMBR has a workspace of 11.7462 μm $\times$ 11.7462 μm $\times$ 0.4713 mrad for the translational motions along x- and y-axes, and the θ_z-rotational motion around z-axis, respectively.

- Expressions for the stress analysis have been derived to be used as guidelines for the dimensional optimisation of the proposed SMBR.

- Assigning *7075 Aluminum* as the material of the flexure hinge-based mechanism, the achieved factor of safety is 4.98 for the mentioned workspace.

- During the primary in-plane translational motions of the proposed SMBR along x- and y-axes, there are parasitic in-plane coupling displacements less than 0.572% of the primary in-plane displacements. Hence, the proposed SMBR has good output decoupling property.

- Lagrange's approach is used to derive the dynamics equation of undamped free vibration of the proposed SMBR in order to determine its natural frequencies.

- Based on Lagrange's approach, the first three natural frequencies of the proposed SMBR are 741.29 Hz, 741.29 Hz, and 884.06 Hz. These frequencies correspond to the translational motions of the proposed SMBR along x- and y-axes, and to the θ_z-rotational motion around z-axis, respectively.

- In comparison with FEA, the analytical dynamic model of the proposed SMBR using Lagrange's approach underestimates the first three natural frequencies by 13.82%, 13.72%, and 20.56%, respectively.

- Due to the unique mechanism design, the proposed SMBR has higher working frequency compared with the published flexural mechanisms in the literature, which is essential since the proposed SMBR will be implemented in lithography machines which have high working frequencies (greater than 2 kHz).

- Since it is crucial to achieve the desired correcting output displacements by the proposed SMBR before the short-stroke motion finishes, the dimensional optimisation, using Grey Wolf Optimizer (GWO), has been carried out with the objective of minimizing the settling time of the proposed SMBR.

- Since the proposed SMBR will be operated, basically, by providing the piezo-electric actuator with the required input voltage, expressions for the in-plane output displacements of the proposed SMBR have been derived in terms in input voltages.

- Implementing the proposed SMBR in lithography machines facilitates manufacturing higher density of electronic circuit in the chip, and this enables a higher CPU processing capability and memory size.

Chapter 3

Dynamic Analysis of the Proposed Smart Materials-Based Reticle Integrated Into the Short-Stroke

The proposed smart materials-based reticle (SMBR) is designed to be integrated into the short-stroke of the reticle stage. It is important to obtain a dynamic model that includes the proposed SMBR within the short-stroke dynamics in the reticle stage. In this way, the dynamic characteristics of the entire stage (the proposed SMBR, piezoelectric actuators, and short-stroke) can be obtained. These include the frequency bandwidth and the settling time of the entire stage with the proposed design.

This chapter includes three sections. The first section introduces the objective of implementing the proposed SMBR into the short-stroke of the reticle stage. Section 3.2 develops the dynamic model of the entire stage. The harmonic and transient analyses are presented in Section 3.3. Finally, Section 3.4 concludes this chapter.

3.1 Introduction

The reticle stage and wafer stage simultaneously control the position of the reticle and the silicon wafer during the step-and-scan imaging process through synchronization motions. These synchronization motions consist of trajectories in x-, y-, z-, θ_x-, θ_y- and θ_z-directions. The semiconductor manufacturing machines adopt long-stroke and short-stroke motions to attain high precision synchronization motions between the reticle and wafer stages [3]. As a result, the step-and-scan imaging process in the semiconductor manufacturing machines are able to cover a large range with high positioning accuracy [10].

There are micro-positioning errors in the synchronization motions in the x-, y-, and θ_z-directions between the reticle and the wafer stages. These errors lead to in-plane shifting of the formed pattern on the silicon wafer, and cause overlay errors in the formed ICs. Consequently, these errors degrade the efficiency of the manufactured ICs [11]. As shown in Figures 3.1 and 3.2, the proposed SMBR is designed to be integrated into the short-stroke of the reticle stage in order to reduce the in-plane errors by adjusting the reticle's position in the x-, y-, and θ_z-directions during the step-and-scan imaging process.

The proposed SMBR is designed to be integrated into the short-stroke of the reticle stage, and it is designed to be operated within frequency bandwidth of more than 550 Hz and small settling time of less than 10 ms. In order to meet these requirements, it is essential to obtain a dynamic model that includes the proposed SMBR within the short-stroke of the reticle stage. Using such model, the dynamic characteristics of the whole system can be investigated over different operating conditions through harmonic and transient analyses. Through the derived dynamic model:

- We can assure having

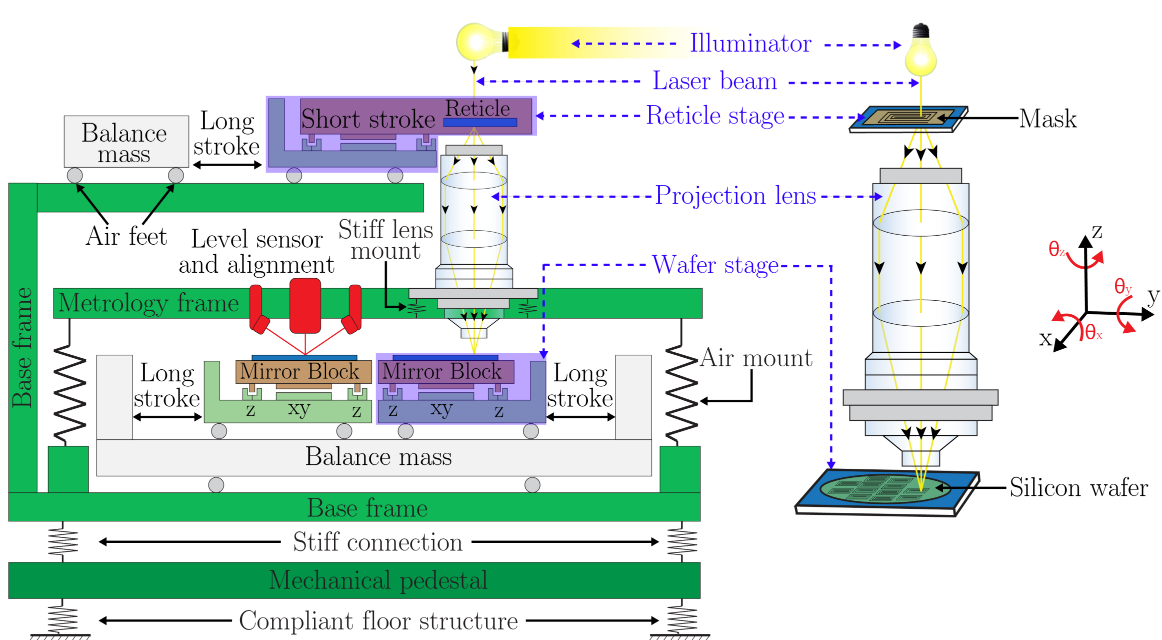

Figure 3.1: A schematic representation of the lithography machine architecture, which consists of three main parts: (i) the reticle stage, (ii) the projection lenses, and (iii) the wafer stage. The y-direction represents the scanning direction, and the reticle stage is our working scope.

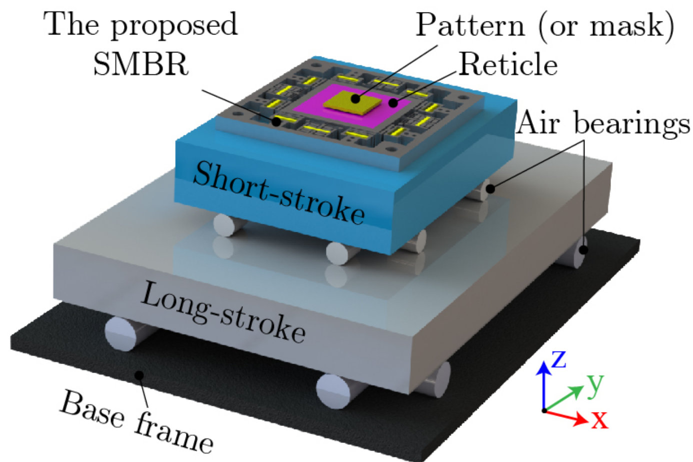

Figure 3.2: A schematic representation of the proposed SMBR stage within the short-stroke of the scanning motion system in lithography machine.

1. high operating frequency bandwidth of more than 550 Hz,

2. stable operation within operating frequencies of less than 550 Hz, and

3. settling time of less than 10 ms.

- The transfer functions between the in-plane output displacements (in x-, y-, and θ_z-directions) and the input forces of the Lorentz actuators and piezoelectric actuators can be obtained.

- Illustrations on how the proposed SMBR can enhance the synchronisation motion and correct the errors can be presented.

3.2 Development of Dynamic Model of the Proposed SMBR Within the Short-Stroke

The proposed SMBR with the piezoelectric actuators is characterized as a lumped mass-spring system as shown in Figure 3.3.

The piezoelectric actuators which are proposed to be implemented in the SMBR are identical. Each actuator has a mass of m_p, a stiffness of k_p and a damping coefficient of c_p. The contacts between the piezoelectric actuators and the flexure hinge-based mechanism have a stiffness of k_c and a damping coefficient of c_c. The equations of motion of the twelve piezoelectric actuators can be derived as follows

$$m_p\ddot{q}_i+C_1\dot{q}_i-\frac{ac_c}{8}\dot{\theta}_r+K_1q_i-\frac{ak_c}{8}\theta_r=F_{p_i} \quad , \text{ for } \; i=1,\;4,\;7,\;10 \tag{3.1}$$

$$m_p\ddot{q}_i+C_1\dot{q}_i+\frac{ac_c}{8}\dot{\theta}_r+K_1q_i+\frac{ak_c}{8}\theta_r=F_{p_i} \quad , \text{ for } \; i=3,\;6,\;9,\;12 \tag{3.2}$$

$$m_p\ddot{q}_i+C_1\dot{q}_i-c_c\dot{y}_r+K_1q_i-k_cy_r=F_{p_i} \quad , \text{ for } \; i=2,\;8 \tag{3.3}$$

$$m_p\ddot{q}_i+C_1\dot{q}_i-c_c\dot{x}_r+K_1q_i-k_cx_r=F_{p_i} \quad , \text{ for } \; i=5,\;11 \tag{3.4}$$

where $C_1=c_p+c_c$ and $K_1=k_p+k_c$; F_{p_i} is the input force provided by the ith piezoelectric actuator ($i=1,2,\ldots,12$) to the proposed SMBR; q_i represents the output

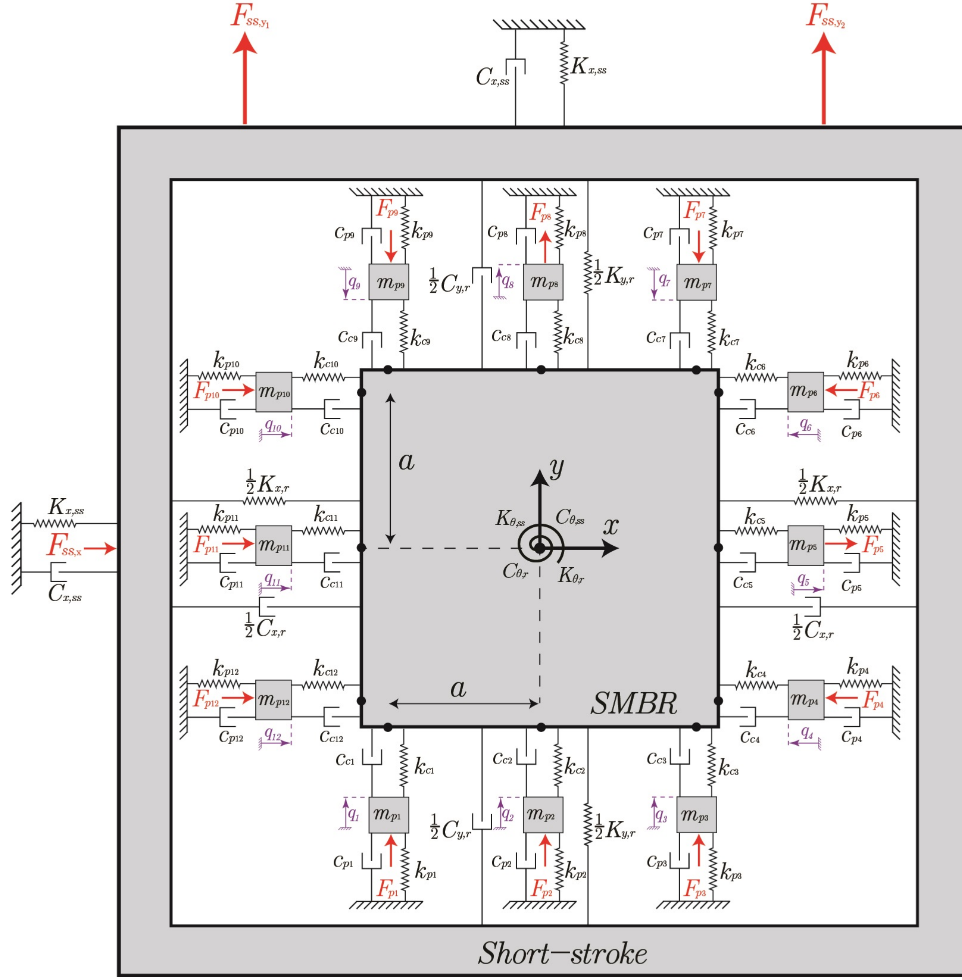

Figure 3.3: An equivalent lumped mass-spring model of the proposed SMBR within the short-stroke.

displacement of the ith piezoelectric actuator; x_r and y_r are the output displacements of the proposed SMBR during the translational motions along x- and y-axes; θ_r is the output displacements of the proposed SMBR during the θ_z-rotational motion about z-axis; and a is the horizontal distance between the line of actuation of the ith piezoelectric actuator and the center of gravity (CoG) of the reticle, O_B. The equation of

motion of the reticle along x-axis can be formulated below:

$$m_{x,r}\ddot{x}_r+C_2\dot{x}_r-C_{x,r}\dot{x}_{ss}-c_c\left(\dot{q}_5+\dot{q}_{11}\right)+K_2x_r-K_{x,r}x_{ss}-k_c\left(q_5+q_{11}\right)=0 \tag{3.5}$$

where $C_2=C_{x,r}+2c_c$ and $K_2=K_{x,r}+2k_c$; $m_{x,r}$ is the effective mass of the proposed SMBR along the x-axis; x_{ss} is the output displacement of the short-stroke along x-axis; $C_{x,r}$ is the equivalent damping coefficient of the proposed SMBR along x-axis; and $K_{x,r}$ is the equivalent stiffness of the proposed SMBR along x-axis. The equation of the short-stroke along x-axis can be formulated below:

$$m_{x,ss}\ddot{x}_{ss}+C_3\dot{x}_{ss}-C_{x,r}\dot{x}_r+K_3x_{ss}-K_{x,r}x_r=F_{x,ss} \tag{3.6}$$

where $C_3=C_{x,r}+C_{x,ss}$ and $K_3=K_{x,r}+K_{x,ss}$; $F_{x,ss}$ is the input force to the short-stroke along x-axis provided by the Lorentz actuators; $m_{x,ss}$ is the effective mass of the short-stroke along the x-axis; $C_{x,ss}$ is the equivalent damping coefficient of the short-stroke along x-axis; and $K_{x,ss}$ is the equivalent stiffness of the short-stroke along x-axis. The equation of motion of the reticle about z-axis can be formulated below

$$J_r\ddot{\theta}_r+C_4\dot{\theta}_r-C_{\theta_r}\dot{\theta}_{ss}-c_ca\left(\sum_{j=\{1,4,7,10\}}\dot{q}_j-\sum_{n=\{3,6,9,12\}}\dot{q}_n\right)-k_ca\left(\sum_{j=\{1,4,7,10\}}q_j-\sum_{n=\{3,6,9,12\}}q_n\right)$$
$$+K_4\theta_r-K_{\theta_r}\theta_{ss}=0 \tag{3.7}$$

where $C_4=C_{\theta_r}+c_ca^2$ and $K_4=K_{\theta_r}+k_ca^2$; J_r is the equivalent moment of inertia of the proposed SMBR about z-axis; $C_{\theta,r}$ is the equivalent damping coefficient of the proposed SMBR about z-axis; and $K_{\theta,r}$ is the equivalent stiffness of the proposed SMBR about z-axis. The equation of the short-stroke about z-axis can be formulated

below

$$J_{ss}\ddot{\theta}_{ss}+C_5\dot{\theta}_{ss}-C_{\theta_r}\dot{\theta}_r+K_5\theta_{ss}-K_{\theta_r}\theta_r=M_{ss} \tag{3.8}$$

where $C_5=C_{\theta_{ss}}+C_{\theta r}$ and $K_5=K_{\theta_{ss}}+K_{\theta r}$; M_{ss} is the input moment about z-axis provided by the Lorentz actuators to the short-stroke; J_{ss} is the equivalent moment of inertia of the short-stroke about z-axis; $C_{\theta,ss}$ is the equivalent damping coefficient of the short-stroke about z-axis; and $K_{\theta,ss}$ is the equivalent stiffness of the short-stroke about z-axis.

As shown in Section 2.4, the parasitic in-plane coupling displacements during the primary in-plane translational displacements along x- and y-axes, are less than 0.572% of the primary in-plane displacements. Consequently, the translational motions along x- and y-axes, and the θ_z-rotational motion about z-axis can be formulated follows.

Using Equations (3.4 – 3.6), the dynamic model of the translational motion along x-axis can be presented as follows

$$\mathbf{M}_x\ddot{\mathbf{x}}_{\text{stage}}+\mathbf{C}_x\dot{\mathbf{x}}_{\text{stage}}+\mathbf{K}_x\mathbf{x}_{\text{stage}}=\mathbf{F}_{x_{\text{stage}}} \tag{3.9}$$

where $\mathbf{F}_{x_{\text{stage}}}=[F_{p_5},\ F_{p_{11}},\ 0,\ F_{x,ss}]^T$ is the input force vector; $\mathbf{x}_{\text{stage}}=[q_5,\ q_{11},\ x_r,\ x_{ss}]^T$ being the displacement vector; $\mathbf{M}_x$, $\mathbf{C}_x$, and $\mathbf{K}_x$ being the equivalent mass, damping, and stiffness matrices, respectively, along x-axis as expressed below

$$\mathbf{M}_x=\text{diag}\{m_p\ \ m_p\ \ m_{x,r}\ \ m_{x,ss}\}$$

$$\mathbf{C}_x=\begin{bmatrix} C_1 & 0 & -c_c & 0 \\ 0 & C_1 & -c_c & 0 \\ -c_c & -c_c & C_2 & -C_{x,r} \\ 0 & 0 & -C_{x,r} & C_3 \end{bmatrix},\ \mathbf{K}_x=\begin{bmatrix} K_1 & 0 & -k_c & 0 \\ 0 & K_1 & -k_c & 0 \\ -k_c & -k_c & K_2 & -K_{x,r} \\ 0 & 0 & -K_{x,r} & K_3 \end{bmatrix}$$

Equation (3.9) can be written in the state-space representation as follows

$$\dot{\mathbf{x}}_{\mathbf{x}}=\mathbf{A}_{\mathbf{x}}\mathbf{x}_{\mathbf{x}}+\mathbf{B}_{\mathbf{x}}\mathbf{u}_{\mathbf{x}} \tag{3.10}$$

$$\mathbf{y}_{\mathbf{x}}=\mathbf{C}_{\mathbf{x}}\mathbf{x}_{\mathbf{x}} \tag{3.11}$$

where $\mathbf{x}_{\mathbf{x}} = [x_1,\ x_2,\ x_3,\ x_4,\ q_5,\ q_{11},\ x_r,\ x_{ss}]^T$; $\mathbf{y}_{\mathbf{x}} = [y_1,\ y_2,\ y_3,\ y_4]^T$; and $\mathbf{u}_{\mathbf{x}} = [F_{p_5},\ F_{p_{11}},\ F_{x,ss}]^T$. The state matrix $\mathbf{A}_{\mathbf{x}}$, the input matrix $\mathbf{B}_{\mathbf{x}}$, and the output matrix $\mathbf{C}_{\mathbf{x}}$, can be expressed as below

$$\mathbf{A}_{\mathbf{x}} = \begin{bmatrix} \mathbf{A}_{x_1} & \mathbf{A}_{x_2} \\ \mathbf{A}_{x_3} & \mathbf{A}_{x_4} \end{bmatrix},\quad \mathbf{B}_{\mathbf{x}} = [\mathbf{B}_{x_1},\ \mathbf{B}_{x_2}]^T,\quad \mathbf{C}_{\mathbf{x}} = [\mathbf{C}_{x_1},\ \mathbf{C}_{x_2}]^T$$

where

$$\mathbf{A}_{x_1} = \begin{bmatrix} \frac{-C_1}{m_p} & 0 & \frac{c_c}{m_p} & 0 \\ 0 & \frac{-C_1}{m_p} & \frac{c_c}{m_p} & 0 \\ \frac{c_c}{m_{x,r}} & \frac{c_c}{m_{x,r}} & \frac{-C_2}{m_{x,r}} & \frac{C_{x,r}}{m_{x,r}} \\ 0 & 0 & \frac{C_{x,r}}{m_{x,ss}} & \frac{-C_3}{m_{x,ss}} \end{bmatrix},\ \mathbf{A}_{x_2} = \begin{bmatrix} \frac{-K_1}{m_p} & 0 & \frac{k_c}{m_p} & 0 \\ 0 & \frac{-K_1}{m_p} & \frac{k_c}{m_p} & 0 \\ \frac{k_c}{m_{x,r}} & \frac{k_c}{m_{x,r}} & \frac{-K_2}{m_{x,r}} & \frac{K_{x,r}}{m_{x,r}} \\ 0 & 0 & \frac{K_{x,r}}{m_{x,ss}} & \frac{-K_3}{m_{x,ss}} \end{bmatrix},$$

$$\mathbf{A}_{x_3} \in \mathbf{I}_{4\times4},\ \mathbf{A}_{x_4} \in \mathbf{O}_{4\times4},\ \mathbf{B}_{x_1} = \begin{bmatrix} \frac{1}{m_p} & 0 & 0 \\ 0 & \frac{1}{m_p} & 0 \\ 0 & 0 & 0 \\ 0 & 0 & \frac{1}{m_{x,ss}} \end{bmatrix},\ \mathbf{B}_{x_2} \in \mathbf{O}_{4\times4},$$

$\mathbf{C}_{x_1} \in \mathbf{O}_{4\times4}$, and $\mathbf{C}_{x_2} \in \mathbf{I}_{4\times4}$.

Accordingly, the transfer functions for the motion along x-axis can be obtained as follows

$$\mathbf{G}_x(s) = \mathbf{C_x}\left(s\mathbf{I} - \mathbf{A_x}\right)^{-1}\mathbf{B_x} \tag{3.12}$$

Using Equation (3.12), the transfer functions of the proposed SMBR and short-stroke for the motion along x-axis can be expressed as follows

$$G_{x,r}(s){=}\frac{\sum\limits_{j=0}^{5} a_j s^j}{\sum\limits_{j=0}^{8} b_j s^j} \tag{3.13}$$

$$G_{x,ss}(s){=}\frac{\sum\limits_{j=0}^{6} c_j s^j}{\sum\limits_{j=0}^{8} b_j s^j} \tag{3.14}$$

where $G_{x,r}(s)$ is transfer function of the proposed SMBR for the motion along x-axis; $G_{x,ss}(s)$ is transfer function of the short-stroke for the motion along x-axis; $a_0{=}44.726 \times 10^{28}$, $a_1{=}1.524 \times 10^{24}$, $a_2{=}1.232 \times 10^{21}$, $a_3{=}1.562 \times 10^{15}$, $a_4{=}2.097 \times 10^{10}$, $a_5{=}1.025 \times 10^{4}$, $b_0{=}2.279 \times 10^{37}$, $b_1{=}1.118 \times 10^{33}$, $b_2{=}1.003 \times 10^{30}$, $b_3{=}1.563 \times 10^{25}$, $b_4{=}3.675 \times 10^{21}$, $b_5{=}5.923 \times 10^{15}$, $b_6{=}1.23 \times 10^{11}$, $b_7{=}9.399 \times 10^{4}$, $b_8{=}1$, $c_0{=}3.409 \times 10^{28}$, $c_1{=}4.421 \times 10^{23}$, $c_2{=}1.466 \times 10^{20}$, $c_3{=}2.309 \times 10^{14}$, $c_4{=}4.914 \times 10^{9}$, $c_5{=}3712$, and $c_6{=}0.04$.

Similarly, the dynamic model for the translational motion of the stage along y-axis can be presented as follows

$$\mathbf{M}_y\ddot{\mathbf{y}}_{\text{stage}} + \mathbf{C}_y\dot{\mathbf{y}}_{\text{stage}} + \mathbf{K}_y\mathbf{y}_{\text{stage}} = \mathbf{F}_{y_{\text{stage}}} \tag{3.15}$$

where $\mathbf{F}_{y_{\text{stage}}} = \left[F_{p_2},\ F_{p_8},\ 0,\ F_{y,ss}\right]^T$ is the input force vector; $\mathbf{y}_{\text{stage}} = \left[q_2,\ q_8,\ y_r,\ y_{ss}\right]^T$ being the displacement vector; $\mathbf{M}_y$, $\mathbf{C}_y$, and $\mathbf{K}_y$ are the equivalent mass, damping,

and stiffness matrices, respectively, along y-axis as expressed below

$$\mathbf{M}_y = \text{diag}\left\{m_p \quad m_p \quad m_{y,r} \quad m_{y,ss}\right\}$$

$$\mathbf{C}_y = \begin{bmatrix} C_1 & 0 & -c_c & 0 \\ 0 & C_1 & -c_c & 0 \\ -c_c & -c_c & C_{2,y} & -C_{y,r} \\ 0 & 0 & -C_{y,r} & C_{3,y} \end{bmatrix}, \; \mathbf{K}_y = \begin{bmatrix} K_1 & 0 & -k_c & 0 \\ 0 & K_1 & -k_c & 0 \\ -k_c & -k_c & K_{2,y} & -K_{y,r} \\ 0 & 0 & -K_{y,r} & K_{3,y} \end{bmatrix}$$

Equation (3.15) can be written in the state-space representation as follows

$$\dot{\mathbf{x}}_\mathbf{y} = \mathbf{A}_\mathbf{y}\mathbf{x}_\mathbf{y} + \mathbf{B}_\mathbf{y}\mathbf{u}_\mathbf{y} \tag{3.16}$$

$$\mathbf{y}_\mathbf{y} = \mathbf{C}_\mathbf{y}\mathbf{x}_\mathbf{y} \tag{3.17}$$

where $\mathbf{x}_\mathbf{y} = [x_1,\ x_2,\ x_3,\ x_4,\ q_2,\ q_8,\ y_r,\ y_{ss}]^T$; $\mathbf{y}_\mathbf{y} = [y_1,\ y_2,\ y_3,\ y_4]^T$; and $\mathbf{u}_\mathbf{y} = [F_{p_2},\ F_{p_8},\ F_{y,ss}]^T$. The state matrix $\mathbf{A}_\mathbf{y}$, the input matrix $\mathbf{B}_\mathbf{y}$, and the output matrix $\mathbf{C}_\mathbf{y}$, can be expressed as below

$$\mathbf{A}_\mathbf{y} = \begin{bmatrix} \mathbf{A}_{y_1} & \mathbf{A}_{y_2} \\ \mathbf{A}_{y_3} & \mathbf{A}_{y_4} \end{bmatrix}, \quad \mathbf{B}_\mathbf{y} = [\mathbf{B}_{y_1},\ \mathbf{B}_{y_2}]^T, \quad \mathbf{C}_\mathbf{y} = [\mathbf{C}_{y_1},\ \mathbf{C}_{y_2}]^T$$

where

$$\mathbf{A}_{y_1} = \begin{bmatrix} \frac{-C_1}{m_p} & 0 & \frac{c_c}{m_p} & 0 \\ 0 & \frac{-C_1}{m_p} & \frac{c_c}{m_p} & 0 \\ \frac{c_c}{m_{y,r}} & \frac{c_c}{m_{y,r}} & \frac{-C_{2,y}}{m_{y,r}} & \frac{C_{y,r}}{m_{y,r}} \\ 0 & 0 & \frac{C_{y,r}}{m_{y,ss}} & \frac{-C_{3,y}}{m_{y,ss}} \end{bmatrix}, \; \mathbf{A}_{y_2} = \begin{bmatrix} \frac{-K_1}{m_p} & 0 & \frac{k_c}{m_p} & 0 \\ 0 & \frac{-K_1}{m_p} & \frac{k_c}{m_p} & 0 \\ \frac{k_c}{m_{y,r}} & \frac{k_c}{m_{y,r}} & \frac{-K_{2,y}}{m_{y,r}} & \frac{K_{y,r}}{m_{y,r}} \\ 0 & 0 & \frac{K_{y,r}}{m_{y,ss}} & \frac{-K_{3,y}}{m_{y,ss}} \end{bmatrix},$$

$$\mathbf{A}_{y_3} \in \mathbf{I}_{4\times4},\ \mathbf{A}_{y_4} \in \mathbf{O}_{4\times4},\ \mathbf{B}_{y_1} = \begin{bmatrix} \frac{1}{m_p} & 0 & 0 \\ 0 & \frac{1}{m_p} & 0 \\ 0 & 0 & 0 \\ 0 & 0 & \frac{1}{m_{y,ss}} \end{bmatrix},\ \mathbf{B}_{y_2} \in \mathbf{O}_{4\times4},$$

$\mathbf{C}_{y_1} \in \mathbf{O}_{4\times4}$, and $\mathbf{C}_{y_2} \in \mathbf{I}_{4\times4}$.

Accordingly, the transfer functions for the motion along y-axis can be obtained as follows

$$\mathbf{G}_y(s) = \mathbf{C_y}\left(s\mathbf{I} - \mathbf{A_y}\right)^{-1}\mathbf{B_y} \tag{3.18}$$

Using Equation (3.18), the transfer functions of the proposed SMBR and short-stroke for the motion along y-axis can be expressed as follows

$$G_{y,r}(s) = \frac{\sum_{j=0}^{5} a_j s^j}{\sum_{j=0}^{8} b_j s^j} \tag{3.19}$$

$$G_{y,ss}(s) = \frac{\sum_{j=0}^{6} c_j s^j}{\sum_{j=0}^{8} b_j s^j} \tag{3.20}$$

where $G_{y,r}(s)$ is transfer function of the proposed SMBR for the motion along y-axis, and $G_{y,ss}(s)$ is transfer function of the short-stroke for the motion along y-axis.

The dynamic model for the θ_z-rotational motion of about z-axis can be presented

using Equations (3.1), (3.2), (3.7) and (3.8), as follows

$$\mathbf{M}_{\theta_z}\ddot{\theta}_{\text{z,stage}} + \mathbf{C}_{\theta_z}\dot{\theta}_{\text{z,stage}} + \mathbf{K}_{\theta_z}\theta_{\text{z,stage}} = \mathbf{F}_{\theta_{\text{z,stage}}} \tag{3.21}$$

where $\mathbf{F}_{\theta_{\text{z,stage}}} = [F_{p_1},\ F_{p_3},\ F_{p_4},\ F_{p_6},\ F_{p_7},\ F_{p_9},\ F_{p_{10}},\ F_{p_{12}},\ 0,\ M_{ss}]^T$ is the input wrench vector; $\theta_{\text{z,stage}} = [q_1,\ q_3,\ q_4,\ q_6,\ q_7,\ q_9,\ q_{10},\ q_{12},\ \theta_r,\ \theta_{ss}]^T$ being the displacement vector; $\mathbf{M}_{\theta_z}$, $\mathbf{C}_{\theta_z}$, and $\mathbf{K}_{\theta_z}$ are the equivalent mass, damping, and stiffness matrices, respectively, for the θ_z-rotational motion about z-axis, as expressed below

$$\mathbf{M}_{\theta_z} = \text{diag}\left\{\mathbf{h}m_p\ J_r\ J_{ss}\right\}$$

$$\mathbf{C}_{\theta_z} = \begin{bmatrix} \mathbf{C}_{\theta_{\text{z},1}} & \mathbf{C}_{\theta_{\text{z},2}} & \mathbf{p} \\ 8\mathbf{C}^T_{\theta_{\text{z},2}} & C_4 & -C_{\theta_r} \\ \mathbf{p}^T & -C_{\theta_r} & C_5 \end{bmatrix},\quad \mathbf{K}_{\theta_z} = \begin{bmatrix} \mathbf{K}_{\theta_{\text{z},1}} & \mathbf{K}_{\theta_{\text{z},2}} & \mathbf{p} \\ 8\mathbf{K}^T_{\theta_{\text{z},2}} & K_4 & -K_{\theta_r} \\ \mathbf{p}^T & -K_{\theta_r} & K_5 \end{bmatrix}$$

where $\mathbf{h} \in \mathbf{1}_{1\times 8}$, $\mathbf{p} \in \mathbf{O}_{8\times 1}$, $\mathbf{C}_{\theta_{\text{z},1}} = \text{diag}\left\{\mathbf{h}C_1\right\}$, $\mathbf{C}_{\theta_{\text{z},2}} = \frac{a}{8}\left[-c_c,\ c_c,\ -c_c,\ c_c,\ -c_c,\ c_c,\ -c_c,\ c_c\ \right]^T$, $\mathbf{K}_{\theta_{\text{z},1}} = \text{diag}\left\{\mathbf{h}K_1\right\}$, and $\mathbf{K}_{\theta_{\text{z},2}} = \frac{a}{8}\left[-k_c,\ k_c,\ -k_c,\ k_c,\ -k_c,\ k_c,\ -k_c,\ k_c\ \right]^T$. Equation (3.21) can be written in the state-space representation as follows

$$\dot{\mathbf{x}}_\theta = \mathbf{A}_\theta \mathbf{x}_\theta + \mathbf{B}_\theta \mathbf{u}_\theta \tag{3.22}$$

$$\mathbf{y}_\theta = \mathbf{C}_\theta \mathbf{x}_\theta. \tag{3.23}$$

where $\mathbf{x}_\theta = [x_1,\ x_2,\ x_3,\ x_4,\ x_5,\ x_6,\ x_7,\ x_8,\ x_9,\ x_{10},\ q_1,\ q_3,\ q_4,\ q_6,\ q_7,\ q_9,\ q_{10},\ q_{12},\ \theta_r,\ \theta_{ss}]^T$,
$\mathbf{y}_\theta = [y_1,\ y_2,\ y_3,\ y_4,\ y_5,\ y_6,\ y_7,\ y_8,\ y_9,\ y_{10}]^T$,
$\mathbf{u}_\theta = [F_{p_1},\ F_{p_3},\ F_{p_4},\ F_{p_6},\ F_{p_7},\ F_{p_9},\ F_{p_{10}},\ F_{p_{12}},\ M_{ss}]^T$. The state matrix $\mathbf{A}_\theta$,

the input matrix $\mathbf{B}_\theta$, and the output matrix $\mathbf{C}_\theta$, can be expressed as below

$$\mathbf{A}_\theta = \begin{bmatrix} \mathbf{A}_{\theta_1} & \mathbf{A}_{\theta_2} \\ \mathbf{A}_{\theta_3} & \mathbf{A}_{\theta_4} \end{bmatrix}, \quad \mathbf{B}_\theta = \left[\mathbf{B}_{\theta_1},\ \mathbf{B}_{\theta_2},\ \mathbf{B}_{\theta_3}\right]^{\mathbf{T}}, \quad \mathbf{C}_\theta = \left[\mathbf{C}_{\theta_1},\ \mathbf{C}_{\theta_2}\right]$$

where

$$\mathbf{A}_{\theta_1} = \begin{bmatrix} \mathbf{A}_{\theta_{1,1}} & \mathbf{A}_{\theta_{1,2}} & \mathbf{p} \\ \mathbf{A}_{\theta_{1,3}} & -C_4/J_r & C_{\theta_r}/J_r \\ \mathbf{p}^T & C_{\theta_r}/J_{ss} & -C_5/J_{ss} \end{bmatrix}, \quad \mathbf{A}_{\theta_2} = \begin{bmatrix} \mathbf{A}_{\theta_{2,1}} & \mathbf{A}_{\theta_{2,2}} & \mathbf{p} \\ \mathbf{A}_{\theta_{2,3}} & -K_4/J_r & K_{\theta_r}/J_r \\ \mathbf{p}^T & K_{\theta_r}/J_{ss} & -K_5/J_{ss} \end{bmatrix}$$

$\mathbf{A}_{\theta_3} \in \mathbf{I}_{10\times10},\ \mathbf{A}_{\theta_4} \in \mathbf{O}_{10\times10},\ \mathbf{B}_{\theta_1} = \text{diag}\left\{\mathbf{h}/m_p\ 0\right\},\ \mathbf{B}_{\theta_2} = \left[\mathbf{p}^T\ 1/J_{ss}\right],$

$\mathbf{B}_{\theta_3} \in \mathbf{O}_{10\times9},\ \mathbf{C}_{\theta_1} \in \mathbf{O}_{10\times10}, \mathbf{C}_{\theta_2} \in \mathbf{I}_{\mathbf{10\times10}},\ \mathbf{A}_{\theta_{1,1}} = \text{diag}\left\{-\mathbf{h}C_1/m_p\right\}$

$\mathbf{A}_{\theta_{1,2}} = \dfrac{a}{8m_p}\left[c_c,\ -c_c,\ c_c,\ -c_c,\ c_c,\ -c_c,\ c_c,\ -c_c\ \right]^T,$

$\mathbf{A}_{\theta_{1,3}} = \dfrac{a}{J_r}\left[c_c,\ -c_c,\ c_c,\ -c_c,\ c_c,\ -c_c,\ c_c,\ -c_c\ \right]$

$\mathbf{A}_{\theta_{2,1}} = \text{diag}\left\{-\mathbf{h}K_1/m_p\right\},\ \mathbf{A}_{\theta_{2,2}} = \dfrac{a}{8m_p}\left[k_c,\ -k_c,\ k_c,\ -k_c,\ k_c,\ -k_c,\ k_c,\ -k_c\ \right]^T,$

and $\mathbf{A}_{\theta_{2,3}} = \dfrac{a}{J_r}\left[k_c,\ -k_c,\ k_c,\ -k_c,\ k_c,\ -k_c,\ k_c,\ -k_c\ \right].$

Accordingly, the transfer functions for the θ_z-rotational motion about z-axis can be obtained as follows

$$\mathbf{G}_{\theta_z}(s) = \mathbf{C}_\theta\left(s\mathbf{I} - \mathbf{A}_\theta\right)^{-1}\mathbf{B}_\theta \tag{3.24}$$

Using Equation (3.24), the transfer functions of the proposed SMBR and short-

stroke for the motion about z-axis can be expressed as follows

$$G_{\theta,r}(s)=\frac{\sum_{j=0}^{17} e_j s^j}{\sum_{j=0}^{20} n_j s^j} \tag{3.25}$$

$$G_{\theta,ss}(s)=\frac{\sum_{j=0}^{18} u_j s^j}{\sum_{j=0}^{20} n_j s^j} \tag{3.26}$$

where $G_{\theta,r}(s)$ is transfer function of the proposed SMBR for the motion about z-axis; $G_{\theta,ss}(s)$ is transfer function of the short-stroke for the motion about z-axis; e_0=6.699×10^{94}, e_1=8.977×10^{89}, e_2=1.05×10^{86}, e_3=6.441×10^{80}, e_4=1.302×10^{76}, e_5=6.175×10^{70}, e_6=6.895×10^{65}, e_7=2.598×10^{60}, e_8=1.984×10^{55}, e_9=5.911×10^{49}, e_{10}=3.341×10^{44}, e_{11}=7.661×10^{38}, e_{12}=3.287×10^{33}, e_{13}=5.468×10^{27}, e_{14}=1.748×10^{22}, e_{15}=1.843×10^{16}, e_{16}=3.867×10^{10}, e_{17}=1.666×10^{4}, n_0=3.686×10^{102}, n_1=1.752×10^{98}, n_2=1.282×10^{95}, n_3=1.885×10^{90}, n_4=1.936×10^{86}, n_5=1.265×10^{81}, n_6=2.704×10^{76}, n_7=1.366×10^{71}, n_8=1.657×10^{66}, n_9=6.704×10^{60}, n_{10}=5.685×10^{55}, n_{11}=1.842×10^{50}, n_{12}=1.189×10^{45}, n_{13}=3.029×10^{39}, n_{14}=1.551×10^{34}, n_{15}=2.967×10^{28}, n_{16}=1.229×10^{23}, n_{17}=1.601×10^{17}, n_{18}=5.398×10^{11}, n_{19}=3.665×10^{5}, n_{20}=1, u_0=7.367×10^{93}, u_1=2.951×10^{89}, u_2=2.426×10^{86}, u_3=1.483×10^{81}, u_4=3.603×10^{76}, u_5=1.763×10^{71}, u_6=2.262×10^{66}, u_7=8.965×10^{60}, u_8=7.864×10^{55}, u_9=2.511×10^{50}, u_{10}=1.66×10^{45}, u_{11}=4.178×10^{39}, u_{12}=2.18×10^{34}, u_{13}=4.127×10^{28}, u_{14}=1.738×10^{23}, u_{15}=2.241×10^{15}, u_{16}=7.673×10^{11}, u_{17}=5.158×10^{5}, and u_{18}=11.429.

3.3 Numerical Results

Harmonic and transient analyses are conducted using the derived dynamic model, presented in Equations (3.10), (3.11), (3.16), (3.17), (3.22), and (3.23), with the parameters listed in Table 3.1.

Table 3.1: The parameters used in the harmonic and transient analyses.

Parameter	Value	Unit
ρ_{pzt}	7800	kg/m^3
m_d	3.6422	kg
m_{ss}	25	kg
m_r	1.2757	kg
J_r	0.1	kg.m^2
J_{ss}	0.7	kg.m^2
k_p	100	N/μm
k_c	5×10^8	N/m
$K_{x,r},\ K_{y,r}$	4.1098×10^8	N/m
$K_{x,ss},\ K_{y,ss}$	5.5×10^8	N/m
K_{θ_r}	2.72×10^6	N.m/rad
$K_{\theta_{ss}}$	5×10^8	N.m/rad

3.3.1 Harmonic Analysis

In this section, the derived dynamic models are implemented to conduct harmonic analysis. Figure 3.4 demonstrates the harmonic response of the derived dynamic model for the output translational motion along x-axis. As depicted in Figure 3.4(a), three peaks appear at 795 Hz, 2.49 kHz, and 37.5 kHz, corresponding to the resonant responses of the motion along x-axis of the proposed SMBR, the short-stroke, and the piezoelectric actuators, respectively. The first peak at 795 Hz corresponds to the resonant response of the proposed SMBR. Based on the FEA results presented in Sec-

tion 2.5 the resonant frequencies of the proposed SMBR (including the piezoelectric actuators) for the translational motions along x- and y-axes occur at 859.14 Hz and 860.14 Hz, respectively. Hence, the analytical model, based on Newton's approach, underestimates the resonant frequencies for the translational motions along x- and y-axes of the proposed SMBR by 7.44% and 7.54%, respectively. The source of the offset might be due to considering the piezoelectric actuators as spring-mass-damper systems through Newton's second law.

In addition, Figure 3.5 demonstrates the harmonic response of the analytical model of the entire stage for the output θ_z-rotational motion about z-axis. As depicted in Figure 3.5(a), three peaks appear, which represent the resonant responses for the θ_z-rotational motion about z-axis of the proposed SMBR, the short-stroke, and the piezoelectric actuators, respectively.

The first peak, representing the resonant response of the proposed SMBR, occurs at 871.36 Hz. Based on the FEA results showed in Section 2.5, the resonant frequency of the proposed SMBR (including the piezoelectric actuators) for the θ_z-rotational motion about z-axis occurs at 1112.9 Hz. Hence, the analytical model, based on Newton's approach, underestimates the resonant frequency for the θ_z-rotational motion about z-axis of the proposed SMBR by 21.7%. The source of the offset might be due to considering the piezoelectric actuators as spring-mass-damper systems through Newton's second law.

Based on Figures 3.4 and 3.5, the resonant frequencies of the piezoelectric actuators are higher than those of the short-stroke. This matches with the operating frequency bandwidth of the short-stroke, since the proposed SMBR acquires high operating frequency bandwidth (below 841.16 Hz).

As a special case, when the proposed SMBR is deactivated from the short-stroke, this case is simulated by assigning a zero value to all contact stiffness between the

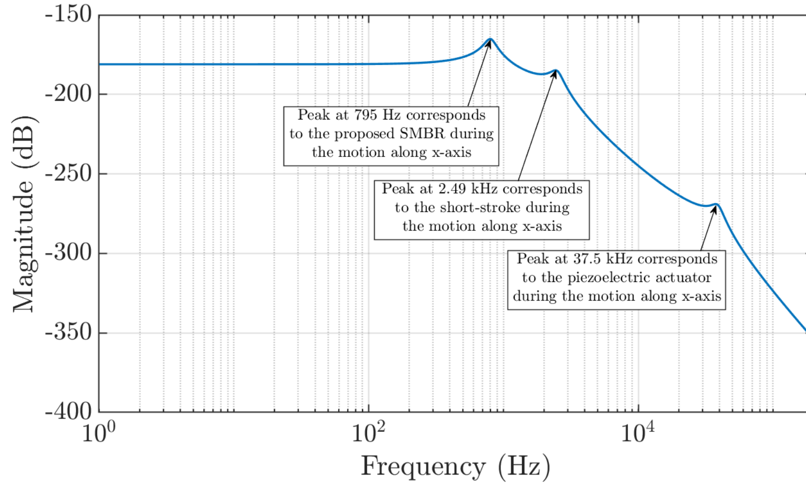

(a)

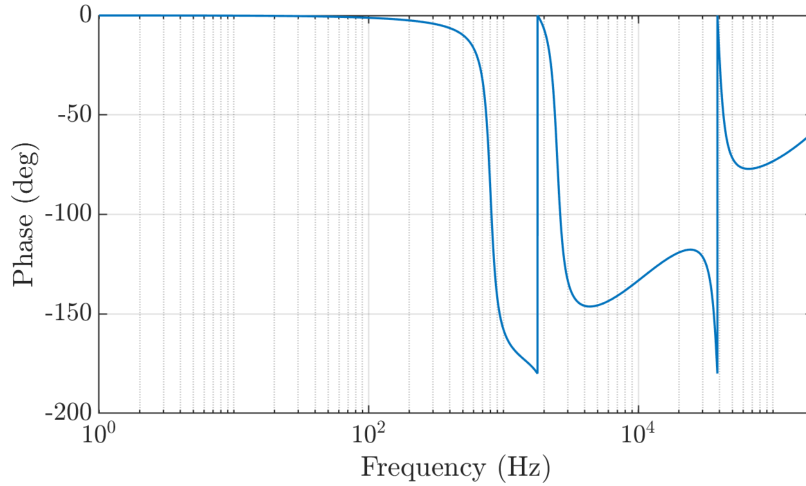

(b)

Figure 3.4: Bode plot of the derived model for the output motion along x-axis: (a) the frequency response, and (b) the phase angle of the response.

piezoelectric actuators and the flexure hinge-based mechanism. In this way, the output motions of the piezoelectric actuators cannot affect the motion of the reticle. The simulation results are shown in Figure 3.6 for the translational motions along x-axis and the θ_z-rotational motion about z-axis, respectively.

Based on Figure 3.6, the peaks of the piezoelectric actuators vanish when the

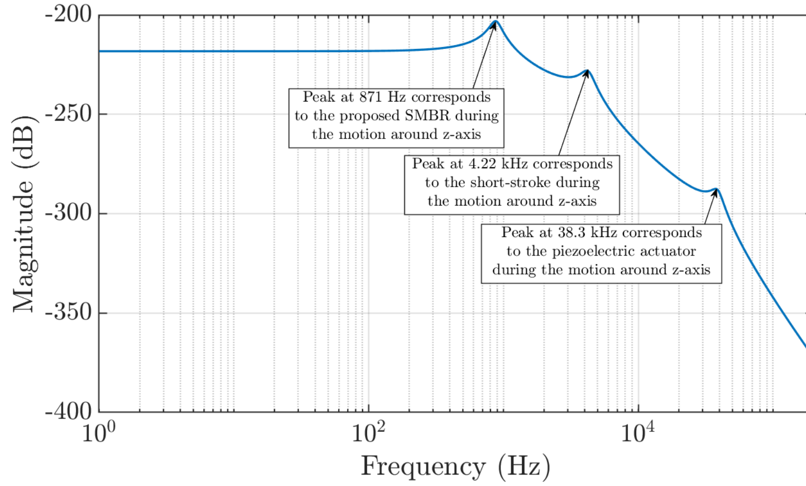

(a)

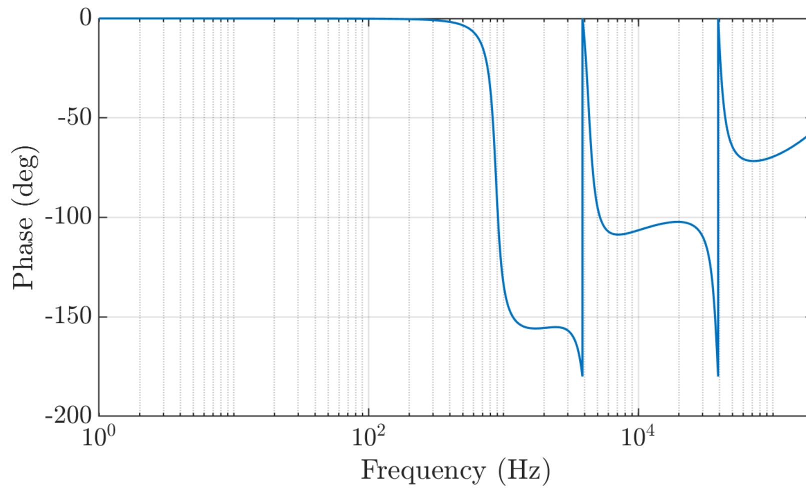

(b)

Figure 3.5: Bode plot of the derived model for the output motion around z-axis: (a) the frequency response, and (b) the phase angle of the response.

piezoelectric actuators disconnect from the stage. In addition, the resonant frequencies of the proposed SMBR and short-stroke are decreased because deactivating the piezoelectric actuators reduces the overall stiffness of the entire stage.

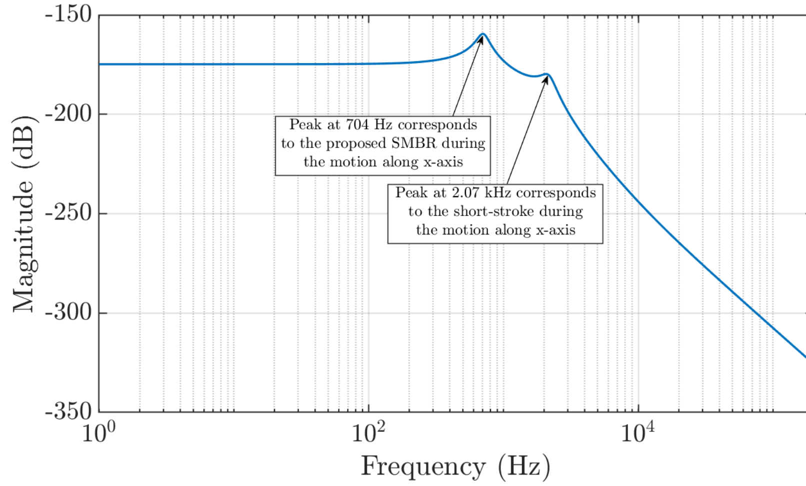

(a)

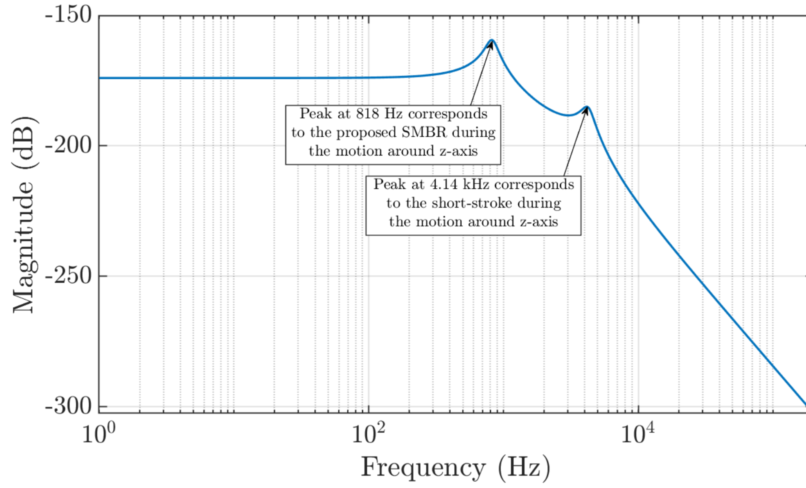

(b)

Figure 3.6: Bode plot of the derived model for the output motions: (a) along x-axis and (b) around z-axis, while the piezoelectric actuators are deactivated

3.3.2 Transient Analysis

In this section, the derived dynamic models are implemented to conduct transient analysis. Figure 3.7 demonstrates the simulation scheme for the translational motions along x- and y-axes, and the θ_z-rotational motion about z-axis.

In Figure 3.7, $G_{x,r}$ and $G_{y,r}$, are the transfer functions between (i) the translational

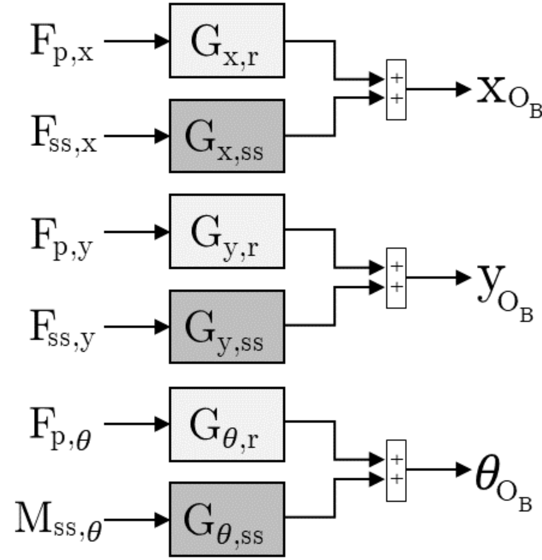

Figure 3.7: The simulation scheme for the translational motions along x- and y-axes, and the θ_z-rotational motion about z-axis, where the transfer functions are obtained using the Equations (3.12) and (3.24).

output displacements of the proposed SMBR along x- and y-axes, respectively, and (ii) the input forces provided by the corresponding piezoelectric actuators (F_{p_x} and F_{p_y}), namely, PZTs 5 and 11 for the motion along x-axis, and PZTs 2 and 8 for the motion along y-axis. Similarly, $G_{\theta,r}$ is the transfer function between (i) the θ_z-rotational output displacement of the proposed SMBR about z-axis, and (ii) the input forces provided by the corresponding piezoelectric actuators (F_{p_θ}), namely, PZTs 1, 3, 4, 6, 7, 9, 10, and 12.

In addition, $G_{\mathrm{x,ss}}$ and $G_{\mathrm{y,ss}}$, are the transfer functions between (i) the translational output displacement of the short-stroke along x- and y-axes, respectively, and (ii) the input forces provided by the Lorentz actuators ($F_{\mathrm{ss,x}}$ and $F_{\mathrm{ss,y}}$). Similarly, $G_{\theta,ss}$ is the transfer function between (i) the θ_z-rotational output displacement of the short-stroke about z-axis, and (ii) the input moment provided by the Lorentz actuators ($M_{\mathrm{ss},\theta}$).

Besides, x_{O_B} and y_{O_B}, are the total translational displacements of the center of gravity (CoG) of the proposed SMBR along x- and y-axes, respectively, due to the

translational displacements of the proposed SMBR and the short-stroke, along x- and y-axes, respectively. $\theta_{z_{O_B}}$ is the total θ_z-rotational displacement of the center of gravity (CoG) of the proposed SMBR about z-axis due to the θ_z-rotational displacements of the proposed SMBR and the short-stroke about z-axis.

Three cases are considered in the transient analysis to demonstrate the working principle of the proposed SMBR when it is integrated to the short-stroke.

3.3.2.1 Case 1: Activating the Proposed Smart Materials-Based Reticle Only

In this case, the proposed SMBR is activated at full stroke in order to achieve maximum translational motions along x- and y-axes, and maximum θ_z-rotational motion about z-axis, namely, $11.7\ \mu\text{m} \times 11.8\ \mu\text{m} \times 0.473$ mrad, respectively. The short-stroke is kept inactive. The simulation results are shown in Figure 3.8.

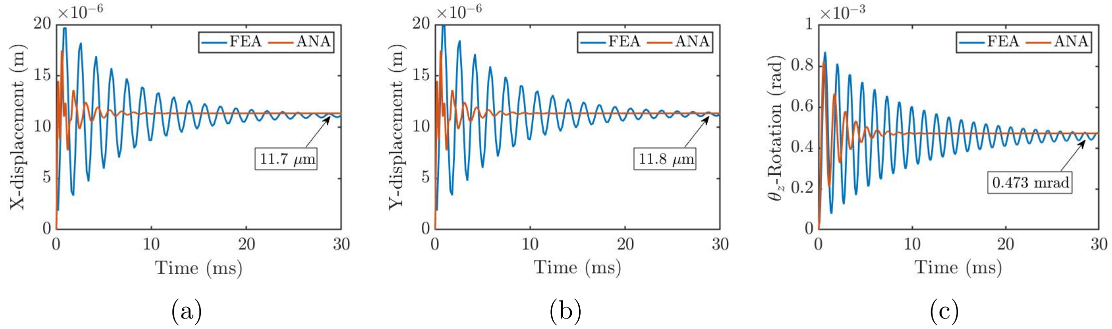

Figure 3.8: A comparison between the FEA results and the analytical results for the output in-plane displacement responses measured at the center of gravity (CoG) of the proposed SMBR, O_B, when the proposed SMBR is activated at full stroke while the short-stroke is kept inactive: (a) the translational motion along x-axis, (b) the translational motion along y-axis, and (c) the θ_z-rotational motion about z-axis.

Based on Figure 3.8, the center of gravity (CoG) of the proposed SMBR has undergone in-plane displacements equal to the maximum workspace of the SMBR, as

expected.

3.3.2.2 Case 2: Activating the Short-Stroke Only

In this case, the short-stroke is activated at full stroke in order to achieve maximum translational motions along x- and y-axes, and maximum θ_z-rotational motion about z-axis, namely, 1 mm $\times$ 1 mm $\times$ 1 mrad, respectively. The proposed SMBR is kept inactive. The simulation results are shown in Figure 3.9.

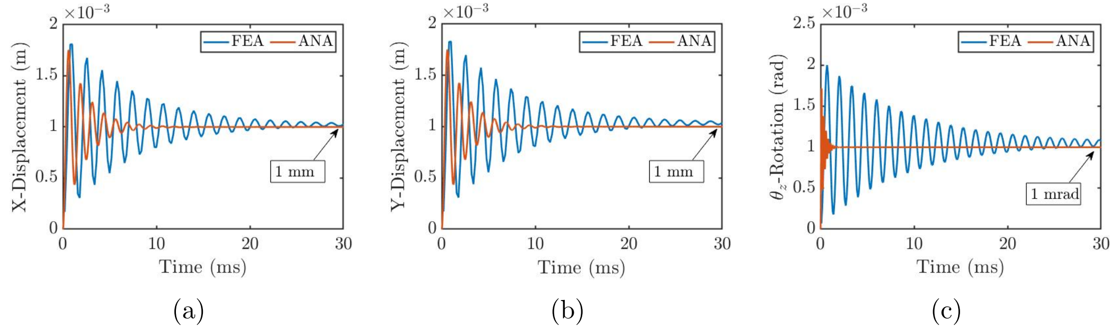

Figure 3.9: A comparison between the FEA results and the analytical results for the output in-plane displacement responses measured at the center of gravity (CoG) of the proposed SMBR, O_B, when the short-stroke is activated at full stroke while the proposed SMBR is kept inactive: (a) the translational motion along x-axis, (b) the translational motion along y-axis, and (c) the θ_z-rotational motion about z-axis.

Based on Figure 3.9, the center of gravity (CoG) of the proposed SMBR has undergone in-plane displacements equal to the maximum workspace of the short-stroke, as expected.

3.3.2.3 Case 3: Activating both the Proposed Smart Materials-Based Reticle and the Short-Stroke at Full Stroke

In this case, both the proposed SMBR and the short-stroke are activated at full stroke in order to achieve maximum translational motions along x- and y-axes, and maxi-

mum θ_z-rotational motion about z-axis, namely, 1011.7 μm $\times$ 1011.8 μm $\times$ 1.473 mrad, respectively. The simulation results are shown in Figure 3.10.

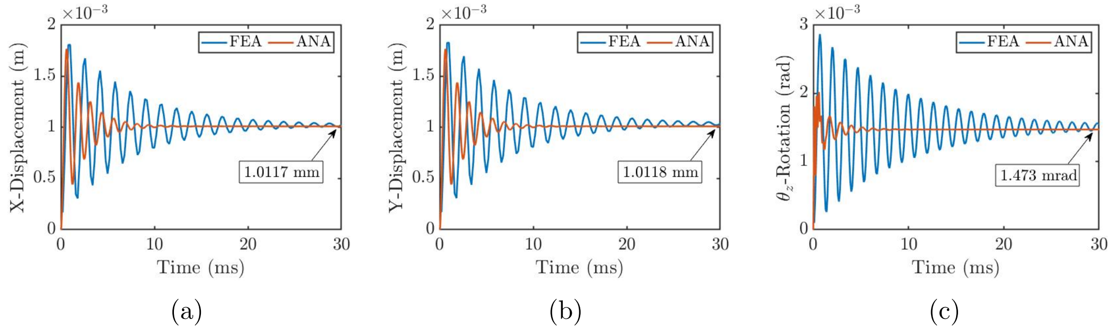

Figure 3.10: A comparison between the FEA results and the analytical results for the output in-plane displacement responses measured at the center of gravity (CoG) of the proposed SMBR, O_B, when both the proposed SMBR and the short-stroke are activated at full stroke: (a) the translational motion along x-axis, (b) the translational motion along y-axis, and (c) the θ_z-rotational motion about z-axis.

Based on Figure 3.10, the center of gravity (CoG) of the proposed SMBR has undergone in-plane displacements equal to the maximum workspaces of the SMBR and the short-stroke, as expected.

3.4 Conclusions of the Chapter

- A dynamic model for the proposed SMBR with the short-stroke is formulated in order to investigate the dynamic characteristics of the whole stage (including the proposed SMBR, the piezoelectric actuator, and the short-stroke).
- From the derived dynamic model, the transfer functions between the in-plane output displacements of the whole stage and each input force have been determined.
- Using the derived dynamic model, harmonic analysis and transient analysis of

the whole stage are performed and then verified by FEA using *ANSYS*.

- The harmonic analysis proved that implementing piezoelectric actuators does not have negative impact on the short-stroke in lithography machines since piezoelectric actuators have much higher resonant frequency than that of the short-stroke. In addition, this analysis illustrated that the entire stage still have high frequency bandwidth even after implementing the proposed SMBR.

- Using the obtained transfer functions of the whole stage, transient analysis is conducted in order to simulate three case scenarios of operating the proposed SMBR with the short-stroke.

Chapter 4

Conclusions and Future Work

The main focus of this thesis was on utilizing a novel smart materials-based reticle (SMBR) in lithography machines. The aim of proposed SMBR is to reduce the relative in-plane micro-positioning error in the synchronization motion between the reticle and the wafer stages. Consequently, manufacturing higher density of electronic circuit in the chip can be attained, and this enables a higher CPU processing capability and memory size.

This has been accomplished by implementing twelve piezoelectric actuators at the reticle stage; such that the proposed SMBR can perform translational motions along x- and y-axes, and θ_z-rotational motion around z-axis at the same instant.

The compliance analysis and the static modelling for the proposed SMBR demonstrated its capability to perform an output motions of 11.7462 μm $\times$ 11.7462 μm $\times$ 0.473 mrad for the translational motions along x- and y-axes, and the θ_z-rotational motion around z-axis, respectively. In addition, the FEA and the derived analytical static model showed a parasitic in-plane coupling displacements of less than 0.572% of the primary in-plane translational displacements along x- and y-axes.

The dynamic modelling of the proposed SMBR integrated within the short-stroke of the lithography machines provided a way to predict the influence of the proposed SMBR on the (i) achieved accuracy, (ii) operating frequency band-width. It has shown that implementing such stage will enhance the lithography process by reducing the micro-scale in-plane errors. Besides, the unique mechanism design of the proposed flexure stage led to high natural frequencies compared with the ones in the literature. In addition, it has been proved that the piezoelectric actuators have higher resonant frequency than the resonant frequency of the short-stroke. Hence, implementing these actuators within the lithography machine does not have negative impact on the operating frequency bandwidth of the machine.

The transient analysis of the proposed SMBR integrated within the short-stroke of the lithography machines explored the capability of the proposed stage in achieving higher precision, where three case scenarios of operating the proposed SMBR within the short-stroke have been simulated to illustrate the achievable precision.

Overall, this research has developed an understanding of the importance of enhancing the achievable accuracy of the micro-positioning scanning stages in lithography machines to produce more efficient integrated circuits. It is reasonable to conclude that the use of piezo-driven micro-stages in lithography machines can improve the positioning accuracy of the scanning system in these machines. However, further investigations on the influence of such implementation on the machine's performance parameters must be conducted, For example, the effect of utilizing the proposed SMBR on the (i) throughput, (ii) maximum speed and acceleration, (iii) settling time, (iv) reticle slip phenomena, ...etc.

Moreover, there are some natural extensions to this work that would help expand and strengthen the results. Validating the analytical and FE results by experimental data is crucial to confirm the capability of the proposed stage in enhancing the

precision of the micro-positioning scanning systems, and to determine the required measurement systems and sensors to achieve the desired tracking performance. Besides, a more detailed analytical dynamic model for the entire lithography machine is important to capture the coupling effect at all stage levels, to model the actual error propagation through all machine's components, and to include the effect of the parasitic vibrations on the achieved positioning accuracy.

In addition, designing a control system of the whole scanning system (the proposed SMBR and the short-stroke) is essential to achieve an enhanced tracking performance of the scanning trajectory. Moreover, structural health monitoring of the proposed SMBR is very important to detect and localize any failure occurs in the stage since getting access to the interior components of lithography machines to perform inspection or troubleshooting tasks is unpreferable because the machine is so sensitive and the lithography process is costly.

Bibliography

[1] M. F. Heertjes, B. Van der Velden, and T. Oomen, “Constrained iterative feedback tuning for robust control of a wafer stage system,” *IEEE Transactions on Control Systems Technology*, vol. 24, no. 1, pp. 56–66, 2016.

[2] H. Butler, “Position control in lithographic equipment,” *IEEE Control Systems Magazine*, vol. 31, no. 5, pp. 28–47, 2011.

[3] C. L. Valentin, “Curvature manipulation of photomasks - enhancing the imaging performance of immersion lithography equipment,” Ph.D. dissertation, Dept. Precision and Microsystems Engineering. TU Delft, Delft University of Technology, Delft, Netherlands, 2013.

[4] A. Haber, “Estimation and control of large-scale systems with an application to adaptive optics for EUV lithography,” Ph.D. dissertation, Delft Center for Systems and Control. TU Delft, Delft University of Technology, Delft, Netherlands, 2014.

[5] C. Mack, *Fundamental principles of optical lithography: The science of microfabrication.* Hoboken, NJ, USA: John Wiley & Sons, 2008.

[6] R. Munnig Schmidt, G. Schitter, and J. van Eijk, *The design of high performance mechatronics: high-tech functionality by multidisciplinary system integration*. Amsterdam, the Netherlands: IOS Press, 2011.

[7] H. Butler and W. Simons, "Position control in lithographic equipment," in *Proceedings of the ASPE 2013 Spring Topical Meeting MIT Laboratory for Manufacturing and Productivity Annual Summit, Cambridge, Massachusetts*, 2013, pp. 7–12.

[8] D. Amin-Shahidi and D. L. Trumper, "Design and control of a piezoelectric driven reticle assist device for prevention of reticle slip in lithography systems," *Mechatronics*, vol. 24, no. 6, p. 562 – 571, 2014.

[9] G. Naaijkens, "Reticle side wall clamping," Ph.D. dissertation, Dept. of Mechanical Engineering. Technische Universiteit Eindhoven, Eindhoven, Netherlands, 2013.

[10] J. van Zundert, T. Oomen, J. Verhaegh, W. Aangenent, D. J. Antunes, and W. P. M. H. Heemels, "Beyond performance/cost tradeoffs in motion control: A multirate feedforward design with application to a dual-stage wafer system," *IEEE Transactions on Control Systems Technology*, vol. 28, no. 2, pp. 1–14, 2018.

[11] H. Butler, "A perspective on stage dynamics and control," in *Proceedings of the ASPE 2008 Spring Topical Meeting "Precision Mechanical Design and Mechatronics for Sub-50 nm Semiconductor Equipment", Berkeley, California*, 2008, pp. 1–3.

[12] Y. Otsu, K. Somaya, and S. Yoshimoto, "High-speed stability of a rigid rotor supported by aerostatic journal bearings with compound restrictors," *Tribology International*, vol. 44, no. 1, pp. 9–17, 2011.

[13] R. Dupont, “Robust rotor dynamics for high-speed air bearing spindles,” *Precision Engineering*, vol. 40, pp. 7–13, 2015.

[14] T. Aoyama, K. Koizumi, Y. Kakinuma, and Y. Kobayashi, “Numerical and experimental analysis of transient state micro-bounce of aerostatic guideways caused by small pores,” *CIRP annals*, vol. 58, no. 1, pp. 367–370, 2009.

[15] Y. Ye, X. Chen, Y. Hu, and X. Luo, “Effects of recess shapes on pneumatic hammering in aerostatic bearings,” *Proceedings of the Institution of Mechanical Engineers, Part J: Journal of Engineering Tribology*, vol. 224, no. 3, pp. 231–237, 2010.

[16] D. de Roover, “Motion control of a wafer stage: A design approach for speeding up ic production,” 1997.

[17] T. Oomen, R. van Herpen, S. Quist, M. van de Wal, O. Bosgra, and M. Steinbuch, “Connecting system identification and robust control for next-generation motion control of a wafer stage,” *IEEE Transactions on Control Systems Technology*, vol. 22, no. 1, pp. 102–118, 2013.

[18] W.-j. Kim and D. L. Trumper, “High-precision magnetic levitation stage for photolithography,” *Precision engineering*, vol. 22, no. 2, pp. 66–77, 1998.

[19] M.-t. Oh and J.-h. Kim, “Kinematic analysis of the reticle stage for lithography with gamma ratio mapping method,” in *2009 International Conference on Mechatronics and Automation, Changchun, China*. IEEE, 2009, pp. 1255–1262.

[20] E. Evers, M. van de Wal, and T. Oomen, “Beyond decentralized wafer/reticle stage control design: A double-youla approach for enhancing synchronized motion,” *Control Engineering Practice*, vol. 83, p. 21 – 32, 2019.

[21] M. Heertjes, D. Hennekens, and M. Steinbuch, "Mimo feed-forward design in wafer scanners using a gradient approximation-based algorithm," *Control Engineering Practice*, vol. 18, no. 5, pp. 495–506, 2010.

[22] M. Baggen, M. Heertjes, and R. Kamidi, "Data-based feed-forward control in mimo motion systems," in *American Control Conference, Seattle, WA, USA*, June 2008, pp. 3011–3016.

[23] M. O. Navarrete, M. F. Heertjes, and R. H. M. Schmidt, "Common zeros in synchronization of high-precision stage systems," in *IEEE International Conference on Mechatronics (ICM), Nagoya, Japan*, March 2015, pp. 602–607.

[24] B. Xia, S. Wu, Y. Tian, K. Yang, and X. Li, "Adaptive sliding mode control for magnetic suspension short-stroke stage in a reticle stage," in *International Conference on Advances in Mechanical Engineering and Industrial Informatics*. Atlantis Press, 2015.

[25] J. M. McCarthy, *21st century kinematics*. London, UK: Springer, 2014.

[26] N. Lobontiu, *Compliant mechanisms: Design of flexure hinges*. Boca Raton, Florida, USA: CRC Press, 2002.

[27] Q. Xu, *Design and implementation of large-range compliant micropositioning systems*. Singapore: John Wiley & Sons, 2017.

[28] K.-B. Choi, J. J. Lee, G. H. Kim, and H. J. Lim, "A compliant parallel mechanism with flexure-based joint chains for two translations," *International Journal of Precision Engineering and Manufacturing*, vol. 13, no. 9, pp. 1625–1632, 2012.

[29] Q. Meng, "A design method for flexure-based compliant mechanisms on the basis of stiffness and stress characteristics," Ph.D. dissertation, The University of Bologna, Italy, 2012.

[30] D. Y. Choi and C. N. Riviere, "Flexure-based manipulator for active handheld microsurgical instrument," in *2005 IEEE Engineering in Medicine and Biology 27th Annual Conference*. IEEE, 2006, pp. 2325–2328.

[31] A. Woronko, J. Huang, and Y. Altintas, "Piezoelectric tool actuator for precision machining on conventional cnc turning centers," *Precision Engineering*, vol. 27, no. 4, pp. 335–345, 2003.

[32] N. Lobontiu and E. Garcia, "Analytical model of displacement amplification and stiffness optimization for a class of flexure-based compliant mechanisms," *Computers & structures*, vol. 81, no. 32, pp. 2797–2810, 2003.

[33] Q. Meng, Y. Li, and J. Xu, "A novel analytical model for flexure-based proportion compliant mechanisms," *Precision Engineering*, vol. 38, no. 3, pp. 449 – 457, 2014.

[34] Y. Tian, B. Shirinzadeh, and D. Zhang, "Design and dynamics of a 3-dof flexure-based parallel mechanism for micro/nano manipulation," *Microelectronic engineering*, vol. 87, no. 2, pp. 230–241, 2010.

[35] Y. Li and Q. Xu, "Design and analysis of a totally decoupled flexure-based xy parallel micromanipulator," *IEEE transactions on robotics*, vol. 25, no. 3, pp. 645–657, 2009.

[36] G. Berselli, "On designing compliant actuators based on dielectric elastomers," Ph.D. dissertation, The University of Bologna, Italy, 2009.

[37] Q. Meng, G. Berselli, R. Vertechy, and V. P. Castelli, "An improved method for designing flexure-based nonlinear springs," in *ASME 2012 International Design Engineering Technical Conferences and Computers and Information in Engineering Conference*. American Society of Mechanical Engineers Digital Collection, 2012, pp. 211–219.

[38] H. Tang and Y. Li, "Design, analysis, and test of a novel 2-dof nanopositioning system driven by dual mode," *IEEE Transactions on Robotics*, vol. 29, no. 3, pp. 650–662, 2013.

[39] Y. Tian, B. Shirinzadeh, and D. Zhang, "A flexure-based five-bar mechanism for micro/nano manipulation," *Sensors and Actuators A: Physical*, vol. 153, no. 1, pp. 96–104, 2009.

[40] Y. Tian and B. Shirinzadeh, "Performance evaluation of a flexure-based five-bar mechanism for micro/nano manipulation," in *2009 IEEE/ASME International Conference on Advanced Intelligent Mechatronics, Singapore*. IEEE, 2009, pp. 76–81.

[41] M. Malosio and Z. Gao, "Multi-stage piezo stroke amplifier," in *2012 IEEE/ASME International Conference on Advanced Intelligent Mechatronics (AIM), Kachsiung, Taiwan*. IEEE, 2012, pp. 1086–1092.

[42] Y. K. Yong, S. S. Aphale, and S. R. Moheimani, "Design, identification, and control of a flexure-based xy stage for fast nanoscale positioning," *IEEE Transactions on Nanotechnology*, vol. 8, no. 1, pp. 46–54, 2008.

[43] H. C. Liaw and B. Shirinzadeh, "Enhanced adaptive motion tracking control of piezo-actuated flexure-based four-bar mechanisms for micro/nano manipulation," *Sensors and Actuators A: Physical*, vol. 147, no. 1, pp. 254–262, 2008.

[44] Y.-j. Choi, S. Sreenivasan, and B. J. Choi, "Kinematic design of large displacement precision xy positioning stage by using cross strip flexure joints and over-constrained mechanism," *Mechanism and Machine Theory*, vol. 43, no. 6, pp. 724–737, 2008.

[45] H. C. Liaw and B. Shirinzadeh, "Neural network motion tracking control of piezo-actuated flexure-based mechanisms for micro-/nanomanipulation," *IEEE/ASME Transactions on Mechatronics*, vol. 14, no. 5, pp. 517–527, 2009.

[46] J. Pinskier, B. Shirinzadeh, L. Clark, Y. Qin, and S. Fatikow, "Design, development and analysis of a haptic-enabled modular flexure-based manipulator," *Mechatronics*, 2016.

[47] J.-W. Lee, Y.-C. Li, K.-S. Chen, and Y.-H. Liu, "Design and control of a cascaded piezoelectric actuated two-degrees-of-freedom positioning compliant stage," *Precision Engineering*, vol. 45, pp. 374–386, 2016.

[48] X.-r. Liu, W.-q. Huang, and Y. Wang, "A novel 2D piezo-nanopositioning stage based on triangle amplifier mechanism," in *Symposium on Piezoelectricity, Acoustic Waves, and Device Applications (SPAWDA), Xi'an, China*, 2016, pp. 314–318.

[49] Y. Du, T. Li, Y. Jiang, and H. Wang, "Design and analysis of a 2-degree-of-freedom flexure-based micro-motion stage," *Advances in Mechanical Engineering*, vol. 8, no. 3, pp. 1–13, 2016.

[50] C. Lin, X. Cui, K. Cheng, and S. Yu, "Design and analysis of 5-DOF micro/nano-positioning stage," *Journal of Software*, vol. 7, no. 5, pp. 1038–1044, 2012.

[51] Y. Li, S. Xiao, L. Xi, and Z. Wu, "Design, modeling, control and experiment for a 2-DOF compliant micro-motion stage," *International Journal of Precision Engineering and Manufacturing*, vol. 15, no. 4, pp. 735–744, 2014.

[52] Z. Wu, Y. Li, and M. Hu, "Design and optimization of full decoupled micro/nano-positioning stage based on mathematical calculation," *Mechanical Sciences*, vol. 9, no. 2, p. 417–429, 2018.

[53] S. Awtar and G. Parmar, "Design of a large range XY nanopositioning system," in *ASME International Design Engineering Technical Conferences and Computers and Information in Engineering Conference, Montreal, Quebec, Canada*, 2010, pp. 387–399.

[54] S. Awtar and A. H. Slocum, "Constraint-based design of parallel kinematic xy flexure mechanisms," *Journal of Mechanical Design*, vol. 129, no. 8, pp. 816–830, 2007.

[55] S. Wan and Q. Xu, "Design and analysis of a new compliant XY micropositioning stage based on roberts mechanism," *Mechanism and Machine Theory*, vol. 95, pp. 125–139, 2016.

[56] Q. Xu, "New flexure parallel-kinematic micropositioning system with large workspace," *IEEE Transactions on Robotics*, vol. 28, no. 2, pp. 478–491, 2012.

[57] X. Zhang, Y. Zhang, and Q. Xu, "Design and control of a novel piezo-driven XY parallel nanopositioning stage," *Microsystem Technologies*, vol. 23, no. 4, pp. 1067–1080, 2017.

[58] S.-C. Huang and T.-P. Dao, "Design and computational optimization of a flexure-based XY positioning platform using fea-based response surface methodology,"

International Journal of Precision Engineering and Manufacturing, vol. 17, no. 8, pp. 1035–1048, 2016.

[59] M. Olfatnia, L. Cui, P. Chopra, and S. Awtar, "Large range dual-axis micro-stage driven by electrostatic comb-drive actuators," *Journal of Micromechanics and Microengineering*, vol. 23, no. 10, 2013.

[60] Y. Li and Q. Xu, "Modeling and performance evaluation of a flexure-based XY parallel micromanipulator," *Mechanism and machine Theory*, vol. 44, no. 12, pp. 2127–2152, 2009.

[61] R. Wang and X. Zhang, "A planar 3-DOF nanopositioning platform with large magnification," *Precision Engineering*, vol. 46, pp. 221–231, 2016.

[62] J. Gan, X. Zhang, H. Li, and H. Wu, "Full closed-loop controls of micro/nano positioning system with nonlinear hysteresis using micro-vision system," *Sensors and Actuators A: Physical*, vol. 257, pp. 125–133, 2017.

[63] C.-L. Chu, H.-C. Chen, and M.-H. Sie, "Development of a $XY\theta_z$ 3-DOF nanopositioning stage with linear displacement amplification device," in *International Conference on Precision Machinery and Manufacturing Technology, Kenting, Taiwan*, vol. 123, 2017.

[64] K. Cai, Y. Tian, F. Wang, D. Zhang, and B. Shirinzadeh, "Development of a piezo-driven 3-DOF stage with t-shape flexible hinge mechanism," *Robotics and Computer-Integrated Manufacturing*, vol. 37, pp. 125–138, 2016.

[65] U. Bhagat, B. Shirinzadeh, L. Clark, P. Chea, Y. Qin, Y. Tian, and D. Zhang, "Design and analysis of a novel flexure-based 3-DOF mechanism," *Mechanism and Machine Theory*, vol. 74, pp. 173–187, 2014.

[66] J. Engelen, "Optimization of comb-drive actuators," Ph.D. dissertation, Dept. of Mathematics and Computer Science. University of Twente, Enschede, Netherlands, 2011.

[67] M. Rakotondrabe and I. A. Ivan, "Development and force/position control of a new hybrid thermo-piezoelectric microgripper dedicated to micromanipulation tasks," *IEEE Transactions on Automation Science and Engineering*, vol. 8, no. 4, pp. 824–834, 2011.

[68] Q. Xu and Y. Li, "Analytical modeling, optimization and testing of a compound bridge-type compliant displacement amplifier," *Mechanism and Machine Theory*, vol. 46, no. 2, pp. 183–200, 2011.

[69] Y. Li and Z. Wu, "Design, analysis and simulation of a novel 3-DOF translational micromanipulator based on the PRB model," *Mechanism and Machine Theory*, vol. 100, pp. 235–258, 2016.

[70] A. J. Fleming and K. K. Leang, *Design, modeling and control of nanopositioning systems*. Switzerland: Springer, 2014.

[71] B. J. Kenton and K. K. Leang, "Flexure design using metal matrix composite materials: Nanopositioning example," in *IEEE International Conference on Robotics and Automation, Saint Paul, MN, USA*, 2012, pp. 4768–4773.

[72] Y. K. Yong and S. O. Reza Mohemani, "A Z-scanner design for high-speed scanning probe microscopy," in *IEEE International Conference on Robotics and Automation, Saint Paul, MN, USA*, 2012, pp. 4780–4785.

[73] S. T. Smith, *Flexures: Elements of elastic mechanisms*. London, UK: CRC Press, 2014.